

CALIBRATING AND IMPROVING THE SENSITIVITY OF THE LIGO DETECTORS

A Dissertation

Submitted to the Graduate Faculty of  
the Louisiana State University and  
Agricultural and Mechanical College  
in partial fulfillment of the  
requirements for the degree of  
Doctor of Philosophy

in

The Department of Physics and Astronomy

by

Jeffrey S. Kissel

B.S., Pennsylvania State University, 2005

M.S., Louisiana State University, 2008

December, 2010

For my father.

# Acknowledgments

I stand on the shoulders of giants. The great majority of the work presented in this thesis would not have been possible without countless hours of tutelage, dedication, guidance, and patience from my advisor Gabriela Gonzalez; my pseudo-advisors Brian Lantz, Brian O'Reilly, and Joe Giaime; my colleagues in the Calibration Team Mike Landry, Keita Kawabe, and Rick Savage; and in the Seismic Team Rich Mittleman, Fabrice Matichard, Ken Mason, Ben Abbott, Corey Gray, and Joe Hanson; and to those who introduced me to and will continue to be my mentors of interferometry Rana Adhikari, Sam Waldman, Matt Evans, Lisa Barsotti, Valera Frolov, Peter Fritschel, and Nergis Mavalvala.

I would also like to acknowledge Sam Finn and Mike Ashley for offering that first glimpse into the field of gravitational wave astronomy. I am forever indebted to their instruction and excitement. I would also like to thank the LIGO fellowship award committee for their generous contribution, as well as their foresight to see that I would fall in love with experimental work.

I would like to thank my fellow (some now former) graduate students, Brent B., Sarah C., Dan C., Kate D., Anamaria E., Tobin F., Justin G., Ryan G., Evan G., Lisa G., Dan H., Sean H., Tyler L., Jonah K., Bill P., Jamie. R., Jake S., Nic S., Jeff S., and Sai V. who have made my time as a graduate student entertaining and memorable.

Last, and most sincerely, I would like to thank Jen Andrews for so many years of love and patience, which has seen me through the good, the bad, and ugly parts of my 5 years of graduate work.

Work presented in this thesis has been supported by NSF grants PHY-0905184 and PHY-0107417.

# Preface

Much of the work presented in this thesis was directly a result of my involvement in the LIGO Scientific Collaboration (LSC). In places where I have reproduced results derived from LIGO data I have done so with permission from the LSC; however, the opinions represented here are my own and not those of the LSC. Even work that was not directly derived from LIGO data often involved much collaboration and discussion with LSC members. I hope that I have given credit where credit is due.

# Table of Contents

Dedication . . . . .	ii
Acknowledgments . . . . .	iii
Preface . . . . .	iv
List of Tables . . . . .	vii
List of Figures . . . . .	viii
Abstract . . . . .	xvii
1. Introduction . . . . .	1
1.1 Linearized Theory of Gravity . . . . .	1
1.2 Gravitational Wave Sources . . . . .	4
1.3 Observation of Gravitational Waves . . . . .	6
2. The Laser Interferometer Gravitational Wave Observatory . . . . .	10
2.1 Power-Recycled, Fabry-Perot Michelson Interferometers . . . . .	10
2.2 Fundamental Noise Sources . . . . .	15
2.3 The Fifth Science Run . . . . .	17
3. Calibration of the LIGO Detectors . . . . .	20
3.1 Model . . . . .	20
3.1.1 Sensing Function . . . . .	22
3.1.2 Digital Filters . . . . .	24
3.1.3 Actuation Function . . . . .	24
3.2 Measurements . . . . .	26
3.2.1 Actuation Function . . . . .	27
3.2.2 Sensing Function . . . . .	30
3.2.3 Open Loop Transfer Function . . . . .	34
3.3 Uncertainty Estimation . . . . .	36
3.4 Results . . . . .	37
3.5 Summary . . . . .	41
4. The Advanced Laser Interferometer Gravitational Wave Observatory . . . . .	42
4.1 The Second Generation of Fabry-Perot Michelson Interferometers . . . . .	42
4.2 Upgrades to the Initial LIGO Interferometers . . . . .	42
4.3 Advanced LIGO Seismic Isolation . . . . .	45
4.4 Goals for Single Stage Seismic Isolation . . . . .	51
5. Prototype HAM-ISI Seismic Isolation System . . . . .	55
5.1 Mechanical Architecture and Design . . . . .	55
5.2 Active Control Model . . . . .	61

5.3	Active Control Design . . . . .	64
5.3.1	Damping Loops . . . . .	64
5.3.2	Blend Filters . . . . .	64
5.3.3	Isolation Loops . . . . .	69
5.3.4	Displacement Sensor Alignment . . . . .	71
5.3.5	Sensor Correction . . . . .	74
5.4	Results . . . . .	77
5.5	The Future . . . . .	81
6.	Conclusions . . . . .	85
	Bibliography . . . . .	87
	Appendix A: LIGO Amplitude Spectral Density . . . . .	94
	Appendix B: The Free-Swinging Michelson Techniques . . . . .	96
	Appendix C: Uncertainty Estimation of the LIGO Response Function . . . . .	103
	Appendix D: Tilt-Horizontal Coupling . . . . .	110
	Appendix E: Copyright Permissions . . . . .	113
	Vita . . . . .	114

# List of Tables

3.1	Summary of the actuation scaling coefficients measured during S5. These single numbers are formed by the mean of each measurement's median $\langle \mathcal{K}_A^{x,y} \rangle_j$ (6 for each end test mass in H1, 5 in H2, and 14 and 15 for the X and Y test masses, respectively in L1). Only statistical uncertainty is reported here; systematic uncertainty is folded the total uncertainty of the actuation function. . . . .	27
3.2	Summary of pendulum frequencies, $f_0^{cm}$ , and quality factors, $Q^{cm}$ , used to compose models of each interferometer's center-of-mass pendulum transfer functions in S5. . . . .	28
3.3	Summary of actuation function uncertainty, in relative magnitude $\sigma_{ A }/ A $ and phase $\sigma_{\phi_A}$ , used in each interferometer in S5. . . . .	30
3.4	Summary of cavity pole frequencies $f_c$ used in each interferometer's sensing function in S5. H1 and H2 have used the average of each arm, hence their numbers reported below are the same, with uncertainty estimated as the quadrature sum of each result. . . . .	31
3.5	Average value for scaling coefficients $\mathcal{K}_C$ for the sensing function, $C_L(f,t)$ for each interferometer. They are stated without uncertainty, since these quantities are derived from measurements of the open loop gain and actuation scaling coefficient. See further discussion in §3.3. . . . .	34
3.6	Summary of band-limited response function errors for the S5 science run. . . . .	38
5.1	Measured properties of prototype HAM ISI mechanical structure. . . . .	59
6.1	Summary of the actuation scaling coefficients measured during S5. These single numbers are formed by the mean of each measurement's median $\langle \mathcal{K}_A \rangle_j$ (6 for each end test mass in H1, 5 in H2, and 14 and 15 for the X and Y test masses, respectively in L1). Only statistical uncertainty is reported here; systematic uncertainty is folded the the total uncertainty of the actuation function. . . . .	101

# List of Figures

1.1	Optical layout of a Michelson interferometer. Coherent, laser light is incident on a beam splitter, which projects the light down perpendicular paths. At the end of each path $L_x$ and $L_y$ is a highly-reflective mirror, or “test mass,” which returns the light to the beam splitter. Here, the light is combined to constructively interfere at the symmetric, input port and destructively interfere at the anti-symmetric, output port. . . . .	7
1.2	Euler angles, $\theta$ , $\phi$ and $\psi$ used to define the antenna patterns $F_{+,\times}(\theta, \phi, \psi)$ . The axis $x^{TT}, y^{TT}$ are aligned with the lines of maximal strain for the plus polarization wave form. . . . .	9
2.1	Strain sensitivity of the LIGO interferometers, adapted from original design (1). . . . .	10
2.2	Optical layout for the LIGO interferometers. Pre-stabilized, $\lambda = 1064$ nm, laser light is phase modulated by a Pockels cell $\phi_m$ , then injected into the input mode cleaner. Stable, diffraction limited, light exits the mode cleaner, and is input into the interferometer. Light exiting both ports of the Michelson are optically isolated from the input and output optics and photodiodes using faraday isolators (FI). The power recycling cavity is formed by the power recycling mirror (PRM), the beam splitter (BS), and input test masses (ITMX, ITMY). The Fabry-Perot arm cavities are formed by the ITMs and the end test masses (ETMs). . . . .	11
2.3	Rendering of the iLIGO vacuum system (2). The layout of the chambers follows the optical layout, where the vertex houses the beam splitter and two input test masses in the larger BSC-style chambers, and all input and output optics in the HAM-style chambers. The end test masses are also in BSC-style chambers at each end station. . . . .	12
2.4	Schematic of Initial LIGO seismic isolation for BSC chamber (left) and HAM chamber (right), adapted from (3). For the BSC chambers, there is a single layer of active external pre-isolation, and four layers of passive isolation. For the HAM chambers, there is also a single layer of active external pre-isolation, but has only three layers of passive isolation. The support structure of the final layer of suspensions (Figure 2.5), is hung from or mounted on the optics platform for the BSC or HAM stacks, respectively. . . . .	13
2.5	A schematic of the LIGO optic suspensions for S5. Actuation force is provided by the coil actuators (mounted to the support structure) which act upon the magnets secured directly on the rear face of the optic. . . . .	13

2.6	Amplitude spectral density of the differential arm length for the Livingston interferometer. We show the control loop reduces the residual RMS ground motion by more than seven orders of magnitude when the interferometer operates at designed sensitivity. . . . .	14
2.7	Comparison between the shot noise of Michelson and Fabry-Perot Michelson interferometers, for the same input power of $P_{BS} = 5$ W. The other parameters of the noise are that of the first generation LIGO detectors: $L = 4$ km, $\lambda = 1064$ nm, $\mathcal{F} = 220$ , and $\eta = 0.9$ . . . . .	16
2.8	The best displacement sensitivity, expressed as equivalent displacement noise, for each interferometer during the S5 science run, and expected total noise in LIGO’s first 4 km interferometers. . . . .	18
2.9	Daily median of detector sensitivity during S5 to a 1.4-1.4 solar mass compact binary system averaged over angle and orientation. Dashed lines indicate the times during which the representative spectra in Figure 2.8 were taken. Large variations in detector sensitivity are due to upgrades or hardware problems.	19
3.1	The model of the control loop for differential changes in length of the Fabry-Perot arm cavities. The interferometer senses a change in DARM length, $\Delta L_{ext}$ according to $\gamma(t)C_L(f)$ , the result of which is the digital error signal $e_D$ , which is then fed back through a set of digital filters $D(f)$ , and converted to analog control via the actuation function of the end test masses $A(f)$ . . .	21
3.2	Schematic breakdown of the sensing function $C_L(f, t)$ . Internal to the LIGO Scientific Collaboration, the digital signal $e_D$ is often colloquially referred to by its digital “channel” name DARM_ERR. From left to right, $C_{FP}(f) \propto H_{FP}^x + H_{FP}^y$ is the arm cavity transfer function; $\alpha(t)$ is the time-dependent variation of the interferometer’s input laser power and optical gain; $\mathcal{K}_C$ is the scaling coefficient which absorbs all constants including the input laser power, optical gain, the quantum efficiency of the photodiodes, the impedance of the photodiode circuitry, and the analog-to-digital gain; $ADC(f)$ is the frequency dependence of the analog to digital conversion; and $\beta(t)$ is the digital factor which compensates for the analog change $\alpha(t)$ . The compensation is not perfect, therefore the factor $\gamma(t) \equiv \alpha(t)\beta(t)$ represents the residual variation.	22
3.3	Schematic breakdown of the signal flow through the actuation function for the X arm $A^x(f)$ . The digital signal $s_D(f)$ is colloquially referred to by its “channel” name DARM_CTRL. From right to left, $\xi^x$ is the fraction of the digital control signal sent to the X arm; $D_A^x(f)$ are digital filters; $DAC(f)$ is the frequency dependence of digital to analog conversion; $K_A^x$ is the scaling coefficient proportional to the digital-to-analog gain, the gain of resistance circuitry which converts voltage to current, the gain of the coil actuators which convert current to magnetic force, and the force-to-displacement transfer function gain; and $P^X$ is the frequency dependence of the force-to-displacement transfer function. . . . .	25

3.4	Physical shape of the end test mass drumhead internal resonance. Left: Cartoon, edge-on view of the fundamental mode of a cylindrical plate (4). Right: Three dimensional modal shape of the drumhead resonance from finite element analysis of a cylinder with dimensions similar to the LIGO test masses (5). . . . .	26
3.5	Time-dependent corrections to the sensing function $\Re\{\gamma(t)\}$ over the course of the science run (6). (Left) Time series of $\Re\{\gamma(t)\}$ for each interferometer. (Right) Histogram of $\Re\{\gamma(t)\}$ for each interferometer. . . . .	32
3.6	Histograms of $\Im m\{\gamma(t)\}$ over the entire S5 run, for H1 (top left), H2 (top right), and L1 (bottom). The standard deviation the data set represents a systematic uncertainty estimation of $\sigma_\gamma$ . The standard deviation $\Im m\{\gamma(t)\}$ for all interferometers is less than 5%, implying a negligible systematic uncertainty. . . . .	33
3.7	Open loop transfer function model vs. measurement comparisons for H1 (top left), H2 (top right), and L1 (bottom) in all of S5. The four panels shown are the magnitude and phase of model and measurements (top and bottom left), and the ratio between model and measurements (top and bottom right). . . . .	35
3.8	Systematic uncertainty in response function arising from the single pole approximation of the Fabry-Perot cavity response in open loop transfer function. This uncertainty is epoch-dependent; only the third epoch for each detector is shown. . . . .	37
3.9	Frequency dependent response function, $R_L(f)$ , for the three LIGO interferometers for all epochs of the S5 science run. . . . .	39
3.10	Frequency dependent error estimates for the response function for H1 (top left), H2 (top right), and L1 (bottom left). In magnitude (top panel) and phase (bottom panel), the total uncertainty (dashed-black) is composed of the uncertainty in actuation, $\sigma_{ A }/ A $ , $\sigma_{\phi_A}$ (in blue), the open loop transfer function magnitude $\sigma_{ G }/ G $ (in green), the open loop transfer function phase, $\sigma_{\phi_G}$ (in red), the time-dependent factor, $\sigma_\gamma/\gamma$ (in cyan), and from the single pole approximation of the Fabry-Perot cavity response (in magenta). . . . .	40
4.1	Comparison between the best initial LIGO strain sensitivity (L1, Aug 2007) and predicted baseline sensitivity for advanced LIGO. . . . .	43
4.2	Optical layout for Advanced LIGO. Changes from the Initial LIGO layout (Figure 2.2) include, increasing the input mode cleaner length, splitting the power recycling into a stable, three-mirror cavity, and the addition of a stable signal recycling cavity and output mode cleaner at the antisymmetric port. . . . .	44

4.3	Proposed Advanced LIGO sensitivity. Three different “modes” are proposed, indicative of possible configurations for the interferometer. Mode (1a) and (1b) are operated at low and high input power ( $P_{IN}^{(1a)} \simeq 25W$ , $P_{IN}^{(1b)} \simeq 125W$ ), with the signal recycling cavity at optimal tuning ( $\phi_{SRM} = 0^\circ$ ). Mode 2 is tuned for maximum range out to which we may see binary neutron star coalescence (optimally oriented, SNR 8), with high input power ( $P_{IN} \simeq 125W$ ) and a detuned signal recycling cavity, $\phi_{SRC} = 20^\circ$ . . . . .	46
4.4	SolidWorks rendering of the in-vacuum components of the seismic isolation and suspension system for the test masses (7). . . . .	47
4.5	Advanced LIGO quadruple suspension (8; 9). (Left) SolidWorks rendering of the final two stages of the suspension, composed entirely of monolithic fused silica. The connecting fibers are welded to the sides of the penultimate and test masses at junctions known as “ears.” These two stages are suspended from the upper stages with steel wire. (Middle, Right) Front and side view, mechanical drawing of the entire suspension assembly. . . . .	48
4.6	Advanced LIGO seismic isolation suspensions and active isolation. Each vacuum chamber shown is equipped with a single layer of hydraulic external pre-isolation or (HEPI). The test masses and beam splitter are in BSC-style chambers (orange) supported by a double-stage in-vacuum isolation platform (BSC-ISI), while HAM-style chambers (purple) which house the input and output optics are supported by a single-stage, in-vacuum seismic isolation platform (HAM-ISI). The test masses are each supported by a quadruple pendulum (cyan). The beam splitter (red), the third power and signal power recycling cavity optics (green), and the remaining recycling cavity optics (dark purple) have a triple pendulum suspensions. The output mode cleaner (yellow) is housed in a double suspension, and the output Faraday isolator in a single suspension. . . . .	49
4.7	SolidWorks rendering of Advanced LIGO HAM triple suspensions (10; 11). (Left) HAM large triple suspension, which will support the large recycling cavity optics (PR3 and SR3). (Right) HAM small triple suspension, which will support the small recycling cavity mirrors (PR2, PRM, SR2, and SRM). The top and intermediate mass are suspended with blade springs in addition to wires to improve vertical isolation. The optics in this rendering have been replaced with dummy masses or blanks, as is typical for the design stages when the exact properties of the optics are not known. . . . .	50
4.8	Power dependent requirements for the advanced LIGO signal recycling cavity. In terms of signal recycling cavity length, mode 1b is the most stringent, and is therefore chosen as the limiting target for the SRCL. . . . .	52
4.9	Model transmission of the HAM Large Triple and HAM Small triple suspensions for advanced LIGO (12; 13). For each suspension, the transmittance is defined by the input motion, at the suspension point of the first suspended stage, to the final optic motion at the bottom of the third suspension stage. In practice we treat the input motion at the suspension point to be that of the entire support structure which is mounted to the single stage isolation platform.	53

4.10 Advanced LIGO Target HAM ISI platform displacement noise (13; 12). The PRCL length requirements serve as rotation requirements in rad/ $\sqrt{\text{Hz}}$ for both recycling cavity lengths. Estimates of the ground motion were measured-modeled from the Livingston observatory, assumed to be average representative spectra the site (the Hanford observatory has roughly equivalent ground motion, (14)). Translational degrees of freedom (X, Y, Z) are measured by an STS-2 seismometer on the ground near the HAM6 chamber. Rotational degrees of freedom (RX, RY, RZ) are estimates from a combination of ground STS-2 data interpreted as tilt ( $> 0.3$ Hz), and differential signal between L4-C seismometers mounted on the four corners of the HAM support structure. . . . .	54
5.1 SolidWorks rendering of the HAM ISI. . . . .	56
5.2 HAM ISI Colocated and Cartesian coordinate systems. The colocated basis is defined by the local clusters of instrumentation in the suspended stage. The cartesian basis, whose origin is defined by the suspended stages center of gravity, is aligned with the global interferometer's coordinate system. . . . .	57
5.3 Picture of the L1 HAM ISI inside the HAM6 chamber, taken just after installation. The support tubes and support stage are visible on the bottom of the chamber, and the suspended stage takes up most of the middle of the chamber. The optical table is littered with ballast mass, required for the platform to be suspended when there is no payload. . . . .	58
5.4 Sensor noise models for individual sensors on the HAM ISI, derived from (15). DISP corresponds to the measured noise of the MicroSense capacitive position sensors (used as displacement sensors), and is a factor of 5 above the predicted displacement noise in (15). GS13 corresponds to the best measured noise performance of the GeoTech GS-13, as in (15). STS is a model of the Streckheisen STS-2 derived from a combination of the best measured displacement noise of the Nanometrics Trillium 240 down to 0.5 Hz, and the vendor specifications below 0.5 Hz. . . . .	59
5.5 Displacement response for Enhanced LIGO sensors. All sensors are readout by a $2^{16}/40$ cts/V ADC. The GS-13 and STS-2 have generator constants of 2200 and 1500 V / (m/s), respectively, however the GS-13 is amplified by an additional factor of 40.2 to improve its signal-to-noise ratio. The corner frequencies for GS-13 and STS-2 are 1 Hz and 8.3 mHz. The Microsense displacement sensors have a sensitivity of 10 V / mm. . . . .	60
5.6 External view of the L1 HAM 6 Chamber. The angled struts, or “gullwings” which connect the support tubes to the ground piers, run across the bottom of the picture painted in blue. . . . .	61

5.7	Model of active control loop and noise couplings to the platform motion $x_p$ . The loop shown is for the X translation direction, but where appropriate, noise couplings are treated to be same for all degrees of freedom. These noise sources are input ground motion, $x_g$ ; sensor noise from the on-board geophones, $n_G$ , the capacitive displacement sensors $n_D$ , and ground inertial sensor $n_S$ ; and platform tilt noise (originating from residual ground motion or sensor noise). . . . .	62
5.8	Damping loop control filter design for L1 HAM6 ISI, for the horizontal colocated inertial sensors (left), and vertical colocated sensors (right). . . . .	65
5.9	Comparison of transfer functions between drive and inertial sensor response in the cartesian basis with damping loops open vs. closed. Translational degrees of freedom are shown on the left, and rotational degrees of freedom on the right. . . . .	65
5.10	Demonstration of calibration accuracy for blend filter design. (Left) Response of displacement sensors and inertial sensors in the X direction, in response to X input. (Right) Ratio between responses. The feature at 1 Hz is from imprecise modeling of the GS-13 instrument response (i.e. the corner frequency and Q are not exactly 1 Hz and 5, respectively). The response of the displacement sensor significantly deviates from the geophone response above 10 Hz due to a resonance in the support structure. . . . .	67
5.11	Complimentary blend filters used for L1 HAM6 ISI. The low pass filters, $F^{LP}$ (shown in shades of blue) are used for the displacement sensors, and high pass filters $F^{HP}$ (shown in shades of green) are used for the inertial sensors. The blend frequencies, $f_B$ , (shown in red, with markers similar to those indicating the filters themselves) for X/Y, Z, RX/RY, and RZ are 0.27, 0.23, 0.3, and 0.19 Hz, respectively. . . . .	68
5.12	Super sensor response to actuator drive for the six cartesian degrees of freedom with damping loops engaged. Here we can fully appreciate the benefit of the simple, stiff, mechanical design. The transfer functions are flat up to the first rigid-body resonances between 0.5 and 2 Hz, and then fall smoothly as $1/f^2$ , for 2 decades in frequency before other resonant modes begin to appear above 100 Hz. . . . .	68
5.13	Digital control filters used to shape the super sensor signal for the L1 HAM ISI. Because the super sensor response is similar below 100 Hz for all degrees of freedom, the design of the isolation control filters is also almost identical. Above 100 Hz, resonances of the payload and internal structure of the platform require additional filtering. . . . .	70
5.14	Predicted open loop transfer function and suppression for the X isolation control loop for the L1 HAM6 ISI. (Left) Filter design over the entire frequency range, (right) zoom of the design in the region around the open loop transfer function unity gain crossing. Limiting the suppression and stability for all degrees of freedom is the resonance in the support support structure around 15 Hz. . . . .	71

5.15 Examples of tilt-horizontal cross coupling generated by misaligned capacitive position sensor plates. (Top) Sensor V1 is misaligned from the $x/y$ plane, such that a real platform translation in the $+x$ direction is misinterpreted as platform tilt in the $+rx$ direction, shown in grey. (Bottom) Sensor V2 and V3 are misaligned in opposing directions from the $x/y$ plane, such that a real platform translation in $+x$ is misinterpreted as platform tilt in the $+ry$ direction. . . . .	72
5.16 Model and measurement of the X response to X drive (in displacement units), before displacement sensor alignment. The measurement is the ratio of a witness STS-2 and cartesian transform of the displacement sensors. The data is shown in solid blue, translational and tilt portions of the model are shown in dashed blue and red (respectively), and the total model is shown in solid red. We see the tilt horizontal coupling frequency is $f_{thc} = 30$ mHz, and the curvature is negative as there is response minimum. . . . .	73
5.17 Example improvement gained using the displacement sensor alignment coefficient $C_{x \rightarrow ry}$ , for the H1 HAM6 ISI. The data shows that the tilt due to horizontal drive has reduced by a factor of 4, and $f_{thc}$ has moved from 30 mHz to 15 mHz. . . . .	73
5.18 Details of the feed forward path for the displacement sensors (zoom from Figure 5.7). The displacement sensors measure the difference between ground motion and platform motion. The components of total feed forward filter $F_x^{FF}$ (dash-dotted box), include a polyphase FIR filter (solid box), and several other IIR filters (dash boxes) which serve to remove undesired features of the practical implementation of the FIR filter. $x_D$ is the drive signal temporarily injected to measure the optimal filter for $F_x^{FF}$ , the excitation. . . . .	75
5.19 Frequency response (in velocity units) of filters used to implement hybrid polyphase FIR feed forward loop. . . . .	75
5.20 Comparison between measured optimal feed forward filter and implemented polyphase FIR filter system (in displacement units) for L1 HAM6 ISI. (Left) Ratio of geophone response to excitation via ground motion and through sensor correction path, compared against the polyphase FIR filter used for all three degrees of freedom. (Right) Ratio of polyphase FIR filter over optimal. . . . .	76
5.21 Amplitude spectral density of measured and modeled displacement noise for X degree of freedom. . . . .	78
5.22 Amplitude spectral density of measured and modeled displacement noise for Y degree of freedom. . . . .	78
5.23 Amplitude spectral density of measured and modeled displacement noise for Z degree of freedom. . . . .	79
5.24 Amplitude spectral density of measured and modeled displacement noise for RX degree of freedom. . . . .	79

5.25	Amplitude spectral density of measured and modeled displacement noise for RY degree of freedom. . . . .	80
5.26	Amplitude spectral density of measured and modeled displacement noise for RZ degree of freedom. . . . .	80
5.27	Estimated DARM displacement noise (for Mode 1a), if the prototype HAM ISI performance (black), and the SRCL target performance (gold) are used as the input motion to the Advanced LIGO SRCL cavity. The coupling is calculated by combining Eqs. 4.1 and 4.3, assuming the input parameters for Mode 1a ( $P_{arm} = 150$ W, $T_{ITM} = 0.014$ , and $\delta L = 10$ pm) and the vertical to horizontal coupling factor for the triple suspensions set to $dx_\ell/dx_Z = 10^{-3}$ . . . . .	81
5.28	SolidWorks rendering of a fully-equipped HAM Chamber. Here, the improvements over Enhanced LIGO are mostly in the support structure, including a HAM-style HEPI system (enclosed in a purple frame) and straight stiff crossbeams (grey). Also visible is one of 6 new L4-C seismometers to be used for further active feed-forward control of the suspended stage. . . . .	82
5.29	Simple model of the improvement in the support structure resonance with the planned improvements to the Advanced LIGO system, i.e. stiffer crossbeams and the addition of HEPI (16). Though feature will remain, the increase in stiffness from the crossbeam moves the fundamental frequency from roughly 13 to 20 Hz, while the addition of HEPI reduces the Q by an order of magnitude. . . . .	83
5.30	SolidWorks rendering of Advanced LIGO HAM ISI support stage, equipped with additional feed-forward L4-Cs circled in red. . . . .	84
6.1	Interferometer configurations used during the simple Michelson method of measuring the actuation scaling coefficient. Left: The simple Michelson configuration, where the power recycling mirror and end test masses are misaligned. Right: The single arm configuration, with the power recycling mirror and the opposing arm's input and end test mass are misaligned. . . . .	96
6.2	Example actuation scaling coefficients for the H2 input test masses $\mathcal{K}_i^{x,y}$ , measured using the simple Michelson method. Top: $\mathcal{K}_i$ as a function of frequency for the X and Y input test mass. Solid lines indicate the median of the data points $\langle \mathcal{K}_i \rangle$ , dashed lines indicate $1\sigma$ error bars (the standard deviation of all frequency points). . . . .	98
6.3	Example actuation scaling coefficients for the H1 end test masses $\mathcal{K}_A^{x,y}(f)$ , measured using the simple Michelson method. Top: $\mathcal{K}_A$ as a function of frequency for the X and Y end test mass. Solid lines indicate the median of the data points $\langle \mathcal{K}_A^{x,y} \rangle$ , dashed lines indicate $1\sigma$ error bars (see §3.3 for description). . . . .	99
6.4	“Asymmetric Michelson” configuration of the interferometer. With the power recycling mirror misaligned, an input test mass and opposing end test mass are aligned. . . . .	99

6.5 Example actuation scaling coefficient for the L1 X arm end test mass $\mathcal{K}_A^x$ , measured using the asymmetric Michelson method. Top: $\mathcal{K}_A^x$ as a function of frequency. Solid lines indicate the median of the data points $\langle \mathcal{K}_A^x \rangle$ , dashed lines indicate $1\sigma$ error bars. Bottom: Histograms for $\mathcal{K}_A^x$ , with the median shown in solid pink, and error bars in dashed pink. . . . .	100
6.6 An example ellipse produced by photodiode demodulated signal $q_{AS}$ versus total power, and corresponding fit to the ellipse used to determine $A_{pp}$ in asymmetric Michelson method. . . . .	101
6.7 Individual measurement medians and uncertainties of the actuation scaling coefficients, $\langle \mathcal{K}_A^x \rangle_j$ (left) and $\langle \mathcal{K}_A^y \rangle_j$ (right), measured over the course of the fifth science run. Measurement numbers 6 in H1 and 7 through 15 in L1 used the asymmetric Michelson technique, the remainder were measured with the simple Michelson technique. Only the magnitude for each measurement (top panels) is used to determine the total scaling coefficient for each test mass (indicated by horizontal lines), as the phase (bottom panels) is consistent with zero. The statistical uncertainty of actuation function is the quadrature sum of each arm's actuation coefficient uncertainty, which takes the larger of the standard deviation of each measurements median, $\langle \mathcal{K}_A \rangle_j$ or the mean uncertainty divided by the number of measurements $\sigma_{\mathcal{K}_A,j}$ . . . . .	102
6.8 Diagram of a horizontal seismometer ( $\Theta_0^{(h)} = \pi/2$ ) under the influence of a small tilt $\theta$ of the platform which is translating in the horizontal direction $x_{sp}$ . . . . .	110
6.9 Model, normalized response of an inertial sensor ( $f_0 = 0.1$ Hz, $Q = 1$ ) under both tilt and translation (in arbitrary velocity units). The idealized response to translation is shown in dashed blue. The response under the influence of linear tilt-horizontal coupling alone is shown in dashed green. If the sign of the tilt curvature is positive (as shown in the right-top drawing), and the magnitude of tilt is equal to the amount of input translation, the resulting response of the inertial sensor is shown in red. However, if the tilt curvature is negative (as shown in the right-bottom drawing), the resulting response is shown in purple. The tilt-horizontal coupling zero is shown in dash-dotted black with $f_{thc} = 0.5$ Hz. . . . .	112

# Abstract

The Laser Interferometer Gravitational wave Observatory (LIGO) is network of three, power recycled Fabry-Perot Michelson interferometers built to detect gravitational waves from astrophysical sources at frequencies between 40 and 6000 Hz. For their fifth science run, from 2005 to 2007, the detectors observed at designed sensitivity, achieving equivalent strain amplitude noise of  $3 \times 10^{-23}$  strain/ $\sqrt{\text{Hz}}$  at 100 Hz. To date, the observatory has not detected gravitational waves. However, even at such sensitivity, the expected detection rate for known astrophysical sources of gravitational waves is likely  $0.02 \text{ yr}^{-1}$ .

The fundamental noise source of these ground-based detectors limiting the sensitivity below 40 Hz is seismic motion. They use multi-stage passive isolation platforms from which their test masses are suspended from piano wire as single pendula providing isolation from ground motion. The residual test mass motion is controlled by electromagnetic actuators on the suspension system in response to the output of the interferometers, keeping them at their operating point. In the first portion of this thesis, I discuss the absolute calibration of the first generation of LIGO interferometer's gravitational wave readout during their fifth science run, the uncertainty of which is limited by the precision to which we can measure the control system above residual seismic noise.

A second generation of detectors, called Advanced LIGO, is currently under construction which will completely replace the first generation. Scheduled to become operational in 2014, they are predicted to improve the sensitivity by ten-fold or more, and will likely improve the detection rate to as much as  $40 \text{ yr}^{-1}$ . To achieve this sensitivity at the lower limit of the band, the test masses will be suspended from multiple cascading pendula. In addition, the multi-stage passive isolation platforms will be replaced with single- and double-stage suspended platforms with built-in active feedback control systems. Prototypes of single-stage active control systems have been in use for two years for a non-invasive upgrade of the LIGO interferometers. In the second portion of this thesis, I present results from these prototypes and demonstrate that their performance can meet the stringent requirement of the second generation of interferometers.

# 1. Introduction

We first describe gravitational radiation as a fundamental result of Einstein's General Relativity in the weak-field limit and how this radiation is observable by a generic Michelson interferometer in remainder of this chapter. The first generation of detectors is then described in detail in Chapter 2, including production of the output signal and its relation to gravitational wave induced strain on the interferometer. Chapter 3 discusses absolute calibration of this output signal during the final science run of the initial LIGO detectors revealing that the limiting factor is seismic in origin. The second generation of detectors are discussed in Chapter 4, with focus on the active isolation to be employed. Chapter 5 we show that results from two prototypes of these isolation systems demonstrating they will meet the stringent requirements set by second generation of detectors. A brief summary and conclusions are presented in Chapter 6.

## 1.1 Linearized Theory of Gravity

Matter and space-time are the constituents of the universe. These two components are governed by the equations of General Relativity, first developed by Albert Einstein, known as the Einstein Field Equations. These ten, coupled, non-linear differential equations can be represented by a single tensor equation<sup>1</sup>,

$$G_{\mu\nu} = R_{\mu\nu} - \frac{1}{2} g_{\mu\nu} R = \frac{8\pi G}{c^4} T_{\mu\nu}. \quad (1.1)$$

On the right-hand side, the four dimensional stress energy tensor,  $T_{\mu\nu}$ , represents the mass and energy in a given spacetime. This given arrangement of matter and energy then determines the four dimensional metric tensors,  $g_{\mu\nu}$  and  $R_{\mu\nu}$ , and the scalar,  $R$ , which define the curvature of spacetime. These equations tell us the structure of spacetime is caused by the presence of matter and energy, while the paths followed by matter and energy are governed by this structure.

The metric tensor, or simply the “metric,”  $g_{\mu\nu}$  determines the fundamental characteristics of a spacetime, describing distance, angle, volume, and even past and future. The simplest metric is called the Minkowski metric which defines the space time interval, or “world line,”  $ds^2$ , between two events in flat Cartesian space which is void of matter,

$$ds^2 \equiv g_{\mu\nu} dx^\mu dx^\nu = -c^2 dt^2 + dx^2 + dy^2 + dz^2, \quad (1.2)$$

the coefficients of which is often written in the form of a  $4 \times 4$  matrix,

$$g_{\mu\nu} = \eta_{\mu\nu} = \begin{pmatrix} -c^2 & 0 & 0 & 0 \\ 0 & 1 & 0 & 0 \\ 0 & 0 & 1 & 0 \\ 0 & 0 & 0 & 1 \end{pmatrix}. \quad (1.3)$$

---

<sup>1</sup>In above definition and following discussion, standard Einstein summation notation is used. Indices that include all four space-time coordinates run from 0 to 3 indicated with greek letter subscripts (superscripts). Indices including only spacial coordinates run from 1 to 3 and are indicated with roman characters. Where possible, all units (contained in factors of,  $c$ , the speed of light,  $G$ , the gravitational constant, etc) are left in place.

Here, the “special” flat Minkowski metric is denoted as  $\eta_{\mu\nu}$ , and the coordinate system is defined with reference to the Cartesian basis,

$$\begin{aligned} x_0 &= t & x_1 &= x \\ x_2 &= y & x_3 &= z, \end{aligned} \quad (1.4)$$

according to convention (17; 18; 19). The Minkowski metric is a good approximation for the space time in which we live in, where there is relatively little mass.

The Ricci tensor  $R_{\mu\nu}$  and Ricci scalar  $R$  are calculated using derivatives of the metric. They are contractions of the Riemann tensor,

$$R^\sigma_{\mu\lambda\nu} \equiv \partial_\lambda \Gamma^\sigma_{\mu\nu} - \partial_\nu \Gamma^\sigma_{\mu\lambda} - \Gamma^\rho_{\mu\nu} \Gamma^\sigma_{\rho\lambda} - \Gamma^\rho_{\mu\lambda} \Gamma^\sigma_{\rho\nu}, \quad (1.5)$$

where  $\partial_\alpha$  denotes the partial derivative,

$$\partial_\alpha \mathbf{A} \equiv \frac{\partial A^\beta}{\partial x^\alpha} e_\beta, \quad (1.6)$$

and  $\Gamma^\alpha_{\beta\gamma}$  is the Christoffel symbol,

$$\Gamma^\alpha_{\beta\gamma} \equiv \frac{1}{2} g^{\alpha\delta} (\partial_\gamma g_{\beta\delta} + \partial_\beta g_{\gamma\delta} - \partial_\delta g_{\beta\gamma}). \quad (1.7)$$

Thus,

$$R_{\mu\nu} = R^\lambda_{\mu\lambda\nu} \quad \text{and} \quad R = g^{\mu\nu} R_{\mu\nu} = R^\mu_\mu. \quad (1.8)$$

In astrophysical regimes, where the amount of mass and curvature are significantly large, the metric  $g_{\mu\nu}$  can become arbitrarily complicated and the field equations describing such systems are highly non-linear. However, if we are interested in the metric near an observer far away from all large sources of curvature (as is the case here at Earth), we may assume that the effect on his coordinate system to be weak. The metric in the spacetime of such a distant observer can be approximated by a small, linear perturbation to the Minkowski metric, or

$$g_{\mu\nu} \equiv \eta_{\mu\nu} + \varepsilon h_{\mu\nu}, \quad (1.9)$$

where  $|\varepsilon| \ll 1$ . This linear formalism, in combination with Einstein’s field equations, predicts the perturbation  $h_{\mu\nu}$  may be interpreted as waves interacting with the observer’s coordinate system that contain information about the original source of curvature. We develop this interpretation below.

We begin with the linearized metric, described by Eq. 1.9, in order to formulate the left-hand-side of the field equations. Partial derivatives of the Minkowski metric vanish, leaving Christoffel symbols to only depend on the perturbation (dropping terms  $\mathcal{O}(\varepsilon^2)$ ),

$$\Gamma^\alpha_{\beta\gamma} = \frac{1}{2} \varepsilon \eta^{\alpha\delta} (\partial_\gamma h_{\beta\delta} + \partial_\beta h_{\gamma\delta} - \partial_\delta h_{\beta\gamma}), \quad (1.10)$$

and the Riemann tensor simplifies to

$$R^\sigma_{\mu\lambda\nu} = \frac{1}{2} \varepsilon \eta^{\sigma\rho} (\partial_\lambda \partial_\mu h_{\nu\rho} - \partial_\lambda \partial_\rho h_{\mu\nu} - \partial_\nu \partial_\mu h_{\lambda\rho} + \partial_\nu \partial_\rho h_{\mu\lambda}). \quad (1.11)$$

We denote the familiar d'Alembertian operator as,

$$\square \equiv \eta^{\alpha\beta}\partial_\alpha\partial_\beta = -\frac{1}{c^2}\frac{\partial}{\partial t} + \frac{\partial}{\partial x^i}, \quad (1.12)$$

such that the Ricci tensor and scalar can be written as

$$R_{\mu\nu} = R^\lambda_{\mu\lambda\nu} = \frac{1}{2}\varepsilon(\partial_\lambda\partial_\mu h_\nu^\lambda + \partial_\nu\partial_\lambda h_\mu^\lambda - \square h_{\mu\nu} - \partial_\nu\partial_\mu h) \quad (1.13)$$

$$R = g^{\mu\nu}R_{\mu\nu} = \varepsilon(\partial_\mu\partial_\nu h^{\mu\nu} - \square h). \quad (1.14)$$

With these results, and again dropping terms  $\mathcal{O}(\epsilon^2)$ , Eq. 1.1 becomes

$$\frac{8\pi G}{c^4}T_{\mu\nu} = \frac{1}{2}\varepsilon(\partial_\lambda\partial_\mu h_\nu^\lambda + \partial_\nu\partial_\lambda h_\mu^\lambda - \square h_{\mu\nu} - \partial_\nu\partial_\mu h - \eta_{\mu\nu}\partial_\lambda\partial_\rho h^{\lambda\rho} + \eta_{\mu\nu}\square h). \quad (1.15)$$

Without loss of generality, we may further compress Eq. 1.15 by substituting a different perturbation in place of  $h_{\mu\nu}$ ,

$$\bar{h}_{\alpha\beta} \equiv h_{\alpha\beta} - \frac{1}{2}\eta_{\alpha\beta}h, \quad (1.16)$$

known as the “trace reverse” perturbation because  $\bar{h}_\mu^\mu = -h_\mu^\mu = -h$ . With such a substitution,

$$\frac{8\pi G}{c^4}T_{\mu\nu} = \frac{1}{2}\varepsilon(\partial_\lambda\partial_\mu\bar{h}_\nu^\lambda + \partial_\nu\partial_\lambda\bar{h}_\mu^\lambda - \square\bar{h}_{\mu\nu} - \eta_{\mu\nu}\partial_\mu\partial_\nu\bar{h}^{\mu\nu}). \quad (1.17)$$

We may further eliminate terms by acknowledging we are free to transform the coordinate system defined in Eq. 1.4 by as long as the Riemann tensor, and therefore the Ricci tensor and scalar remain unchanged. One such transformation is

$$x_\alpha^{TT} = x_\alpha + \varepsilon \phi_\alpha^{TT}, \quad (1.18)$$

where  $\phi_\alpha^{TT}$  is a function of position,  $\partial^\alpha\phi_\alpha^{TT} = 0$ ,  $\square\phi_\alpha^{TT} = \partial_\beta\bar{h}_\alpha^\beta = 0$ . Under such a transform, the first, second, and fourth term of Eq. 1.17 vanish, the trace-reverse perturbation is equivalent to the original perturbation, and

$$\frac{8\pi G}{c^4}T_{\mu\nu} = -\frac{1}{2}\varepsilon\square h_{\mu\nu}^{TT}. \quad (1.19)$$

Finally, making the approximation that in the nearly flat spacetime of the solar system, the stress-energy tensor vanishes leaving only a three-dimensional wave equation of the following form

$$0 = \square h_{\mu\nu}^{TT} = \left(\nabla^2 - \frac{1}{c^2}\frac{\partial}{\partial t}\right)h_{\mu\nu}^{TT} \quad (1.20)$$

from which we definitively find the existence of time dependent waves  $h_{\mu\nu}^{TT}(x_0^{TT}, x_3^{TT})$ , which travel at the speed of light,  $c$ . Further, it can be shown in the transverse-traceless gauge,

after employing symmetries demanded by the Riemannian geometry, only two independent components of the original perturbation remain,

$$h_{\mu\nu}^{TT} = \begin{pmatrix} 0 & 0 & 0 & 0 \\ 0 & h_{11} & h_{12} & 0 \\ 0 & h_{12} & -h_{11} & 0 \\ 0 & 0 & 0 & 0 \end{pmatrix}, \quad (1.21)$$

where each component is transverse and time dependent, and may be expressed as plane waves,

$$h_{\mu\nu}^{TT} = A_{\mu\nu} e^{ik_\beta x^\beta} \quad (1.22)$$

as long as  $k_\lambda k^\lambda = 0$  (i.e. the wave is transverse) and  $A_{\alpha\beta} k^\beta = 0$  (from the gauge condition  $\square \phi_\alpha^{TT} = \partial_\beta \bar{h}_\alpha^\beta = 0$ ). With only two independent components it is often convenient to express the plane wave solution as to independent polarizations, or “wave forms”

$$h_{\alpha\beta}^{TT} = \begin{pmatrix} 0 & 0 & 0 & 0 \\ 0 & h_{11} & 0 & 0 \\ 0 & 0 & -h_{11} & 0 \\ 0 & 0 & 0 & 0 \end{pmatrix} + \begin{pmatrix} 0 & 0 & 0 & 0 \\ 0 & 0 & h_{21} & 0 \\ 0 & h_{21} & 0 & 0 \\ 0 & 0 & 0 & 0 \end{pmatrix}$$

$$h_{\alpha\beta}^{TT}(x_0, x_3) = h_+^{TT}(t - z/c) + h_x^{TT}(t - z/c), \quad (1.23)$$

where we have reverted back from tensor notation into the cartesian basis. We will find that it is often more convenient to write these waveforms in the Fourier domain, as  $h_{+,x}^{TT}(f)$ , where

$$h_{+,x}^{TT}(t - z/c) = \int_{-\infty}^{\infty} h_{+,x}^{TT}(f) e^{2\pi i f(t-z/c)} df. \quad (1.24)$$

## 1.2 Gravitational Wave Sources

One can derive how astrophysical sources produce these gravitational waves by using a multipolar expansion of the stress energy tensor  $T_{\mu\nu}$ , instead of assuming vacuum (17; 18). The resulting expansion yields an expression for the spatial components of the strain in the transverse-traceless gauge,

$$h_{jk}^{TT} = \frac{2}{r} \frac{G}{c^4} \frac{\partial^2}{\partial t^2} (I_{jk}^{TT}(t - r/c)), \quad (1.25)$$

where  $I_{jk}^{TT}$  is the reduced quadrupole moment of the source,  $t$  is time in the observer’s frame, and  $r$  is the distance from the source to the observer. Hence, a source (or sources) whose mass has a time-varying quadrupolar moment will generate time and amplitude dependent gravitational waves. There are many astrophysical sources for gravitational radiation. We can obtain a rough, order-of-magnitude estimate for the strain produced by a given source

by approximating the time derivative of the quadrupole moment in Eq. 1.25 as the kinetic energy of the system associated with quadrupolar motion  $E_K^{QP}$ ,

$$h_{jk}^{TT} \simeq \frac{1}{r} \frac{G}{c^2} \left( E_K^{QP} / c^2 \right). \quad (1.26)$$

If we set the quadrupolar kinetic energy to have the rest energy of a solar mass,  $E_K^{QP}/c^2 = 1M_\odot$ , and take such a source to be at roughly the distance of the VIRGO cluster,  $r \simeq 15$  Mpc, then the strain amplitudes we expect are of order

$$h_{jk}^{TT} \simeq 10^{-21}. \quad (1.27)$$

However, this estimate is extremely crude. Listed below are some expected types of the sources of gravitational waves, which are predicted to have amplitudes as large as  $10^{-20}$  (20) or as small as  $10^{-28}$  (21), depending on the source mechanism, efficiency, measurement duration, and distance.

- Stochastic background radiation of cosmological or astrophysical origin - General relativity predicts stochastic gravitational radiation which is omnipresent in the universe, analogous to the Cosmic Microwave Background from electromagnetic radiation. This background may be composed of radiation from cosmological or many, unresolved astrophysical sources. For a cosmological background, the sources include (but are not limited to) residual big-bang radiation, the amplification of quantum vacuum fluctuations, and cosmic string cusps. Coalescing binary systems, rotating neutron stars, and core-collapse supernovae that are too frequent in time to resolve are the believed astrophysical sources for stochastic gravitational wave background (22; 23). B. Allen (22) estimates the strain produced by this background to be

$$h_{jk}^{TT} \approx 10^{-20} h_{100} \sqrt{\Omega(f)} \left( \frac{100 \text{ Hz}}{f} \right), \quad (1.28)$$

where  $h_{100}$  is a dimensionless factor of order unity reflecting the uncertainty in the Hubble constant, and  $\Omega(f)$  is the power spectral density of the gravitational wave energy density. For  $h_{100} \sim 0.75$ , and if  $\Omega(f) = 10^{-8}$  over a bandwidth  $50 \text{ Hz} < f < 150 \text{ Hz}$ , then the strain is of order  $h_{jk}^{TT} \sim 10^{-24}$  (22).

- Continuous Radiation from rotation of non-spherical compact objects - The non-axisymmetric distortions of a rapidly rotating neutron star cause disturbances in spacetime (24). In realistic neutron stars, such quadrupolar distortions could be supported by either elastic stresses or strong magnetic fields misaligned to the axis of rotation (21). For the later case, if the magnetic field poles are in the line of sight, polarized electromagnetic emission causes the star to pulse, and is therefore named a Pulsar. Pulsars in accreting binary systems, may have in-falling matter guided by magnetic fields which can also lead to quadrupolar moments (21; 25). Radio observations of the spin rate decrease of pulsars place upper limits on their gravitational wave emission. However, this emission may be directly detectable, and if not, a search would at least provide the opportunity to further refine these upper limits (24; 26). Current estimates (25) of the strain produced by these stars range from

$$h_{jk}^{TT} \approx 10^{-22} \left( \frac{f}{1 \text{ kHz}} \right)^{1/2} \quad (1.29)$$

to as low as  $h_{jk}^{TT} \approx 10^{-27}$  (at similar frequencies) (21).

- Radiation from Compact Binary Coalescences -

A large fraction of the stellar population are found in binary systems (27; 28). A binary system composed of two neutron stars, two black holes, or one of each may have a significant fraction of its orbital energy lost to gravitational radiation. As radiation is emitted, the orbital angular momentum of the system decreases with time, reducing the size of the orbit. The reduction in the size of the orbit decreases the orbital frequency, the rate of which can be predicted by general relativity. First confirmed by the spin rate decrease in the Hulse-Taylor pulsar (29; 30), gravitational radiation has now been inferred from several other binary pulsar systems including the fantastic double-pulsar binary system PSR J07373039 (31).

Eventually, the binary system will lose so much energy that it collapses, and the two compact objects will coalesce into one releasing gravitational radiation while doing so. The amplitude of the strain depends on the mass of the compact binary system,

$$h_{jk}^{TT} \approx 10^{-24} \left( \frac{15 \text{Mpc}}{R} \right) \left( \frac{M_1^3 M_2^3}{M_1 + M_2} \right)^{1/4} \left( \frac{1 \text{ day}}{\tau} \right)^{1/4}, \quad (1.30)$$

where  $R$  is the distance to the source,  $M_1$  and  $M_2$  are the mass of each component of the binary, and  $\tau$  is the time until collision (32). For a neutron star binary, where  $M_1 = M_2 = 1.4 M_\odot$ , at a distance of 200 Mpc, this amplitude is roughly  $h_{jk}^{TT} \sim 10^{-22}$ . The waveforms of such events are now fully predictable using numerical relativity (33; 34; 35), and the astrophysically occurrence rates of systems may be constrained by electromagnetic observations (28; 36). These, among other factors, make these systems the most promising sources of gravitational radiation.

- Burst radiation from supernovae and other transient sources -

Supernovae, the collapse of massive stars as they end their lives, are believed to emit gravitational radiation if the collapse is asymmetric in any fashion (i.e. the quadrupolar moment of the gravitational field is significant) (20; 37). However, astrophysical evidence provides minimal guidance for models of the radiation. In addition, the explosions pose extreme technical difficulties when calculating the bulk properties of degenerate matter during collapse that only recently have computational astrophysicists have begun to surpass. Recent progress (20) place estimates on the maximum strain to be between  $10^{-23} \leq h_{jk,max}^{TT} \leq 10^{-20}$ .

Along with supernovae, noteworthy astrophysics may also come from those sources for which we have no model. In that case, we stand to gain the most knowledge from the observation of these sources and their gravitational radiation. If observed, one might be able to develop physical models of the source without any other information (38).

### 1.3 Observation of Gravitational Waves

A suitable detector for gravitational waves is a Michelson interferometer. The concepts for which first appeared in the 1950s (39; 40), but it was not until the 1970s that they were practically designed (41; 42; 43). The optical layout of such an interferometer is shown in Figure 1.1. We examine the basic principles of such an interferometer by discussing the behavior of space time between the two perpendicular arms on the interferometer.

A given “test mass” – a particle that is free from all forces – must have a time-like world line  $x^\alpha(\tau)$  whose tangent  $\partial_\tau x^\alpha \equiv U^\mu$  remains constant. This can be expressed as the

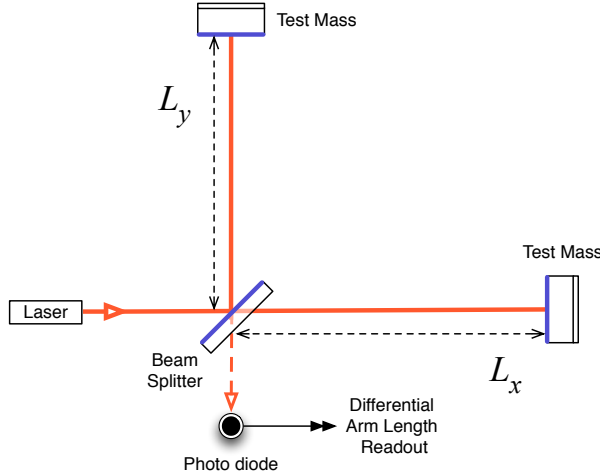


Figure 1.1: Optical layout of a Michelson interferometer. Coherent, laser light is incident on a beam splitter, which projects the light down perpendicular paths. At the end of each path  $L_x$  and  $L_y$  is a highly-reflective mirror, or “test mass,” which returns the light to the beam splitter. Here, the light is combined to constructively interfere at the symmetric, input port and destructively interfere at the anti-symmetric, output port.

“geodesic equation,”

$$0 = \frac{\partial^2 x^\alpha}{d\tau^2} + \Gamma_{\beta\gamma}^\alpha \left( \frac{\partial x^\beta}{\partial \tau} \right) \left( \frac{\partial x^\gamma}{\partial \tau} \right), \quad (1.31)$$

where  $\tau$  is the affine parameter, “proper time,” and  $\Gamma_{\beta\gamma}^\alpha$  is as defined in Eq. 1.7. If we consider the particle to be initially at rest in space-time which is flat other than the metric perturbation, the tangent  $U^\alpha$  can be thought of as the four-velocity of the particle, and  $U^\alpha = (\tau, 0, 0, 0)$ . This reduces the geodesic equation to

$$\frac{\partial^2 x^\alpha}{\partial \tau^2} = -\Gamma_{00}^\alpha \tau^2. \quad (1.32)$$

Further, in the transverse-traceless gauge, we have shown a perturbation to the metric  $h_{\mu\nu}^{TT}(t-z)$  to have  $h_{00}^{TT} = h_{\mu 0}^{TT} = h_{0\mu}^{TT} = 0$ , which means, from Eq. 1.10, that

$$\Gamma_{00}^\alpha = \frac{1}{2} \eta^{\alpha\lambda} (\partial_0 h_{\lambda 0}^{TT} + \partial_0 h_{0\lambda}^{TT} - \partial_\lambda h_{00}^{TT}) = 0, \quad (1.33)$$

and

$$\frac{\partial^2 x^\alpha}{\partial \tau^2} = 0. \quad (1.34)$$

In other words, the particle experiences no acceleration from the passing gravitational wave in the transverse-traceless gauge.

However, consider a photon traveling between two particles separated by a distance  $L_x$ , along x-axis of the TT-gauge Cartesian coordinate system whose z-axis is defined to be the direction of wave propagation, as discussed in §1.1. The photon will follow a null world line,

$$0 = g_{\mu\nu}dx^\mu dx^\nu = -c^2dt^2 + (1 + h_+^{TT})dx^2, \quad (1.35)$$

from which we may say

$$cdt = \left( \sqrt{1 + h_+^{TT}} \right) |dx| \simeq \left( 1 + \frac{1}{2} h_+^{TT} \right) |dx|. \quad (1.36)$$

This may be interpreted in two ways. We may say that the local coordinates of one of the test masses are fixed, such that the round-trip time of the photon  $T$  between the two test masses can be found from the integral of Eq. 1.36,

$$T_x = \frac{1}{c} \left( 1 + \frac{1}{2} h_+^{TT} \right) L_x, \quad (1.37)$$

implying a roundtrip delay of

$$\Delta T_x = \frac{h_+^{TT} L_x}{2c}. \quad (1.38)$$

On the other hand, if we instead fix the proper time between the test masses, then the distance between the test mass, as measured by one of the test masses is

$$\Delta L_x = \frac{1}{2} h_+^{TT} L_x. \quad (1.39)$$

Similarly, if we now place a third test mass along the Y-axis of the TT coordinate system, at a distance  $L_y$ , then the world line is

$$0 = g_{\mu\nu}dx^\mu dx^\nu = -c^2dt^2 + (1 - h_+^{TT})dy^2, \quad (1.40)$$

and

$$\Delta L_y = -\frac{1}{2} h_+^{TT} L_y. \quad (1.41)$$

A michelson interferometer may be setup in this exact fashion. The beam splitter is the reference test particle from which distance and time are measured, and the two end mirrors are at distances  $L_x$  and  $L_y$  along the x- and y-axis (See Figure 1.1). Many coherent, monochromatic, photons are then injected into the symmetric port of the beam splitter. As the photons return from the round trip in each arm, they have now accumulated a round trip travel time difference

$$\Delta T = \Delta T_x - \Delta T_y = h_+^{TT} \frac{L_x + L_y}{2c} = h_+^{TT} \frac{L}{c}, \quad (1.42)$$

implying a phase change between the arms of

$$\Delta\Phi = \Delta\Phi_x - \Delta\Phi_y = \frac{4\pi}{\lambda} \left( \frac{1}{2} h_+^{TT} L_x + \frac{1}{2} h_+^{TT} L_y \right) = \frac{4\pi}{\lambda} h_+^{TT} L, \quad (1.43)$$

which may be interpreted as a differential arm length change in the arms,

$$\Delta L = \Delta L_x - \Delta L_y = h_+^{TT} \frac{L_x + L_y}{2} = h_+^{TT} L. \quad (1.44)$$

In Eqs. 1.42, 1.43 and 1.44, we have defined the average length of the two arms,  $L = (L_x + L_y)/2$ .

In general, the gravitational plane wave is incident at arbitrary polar and azimuthal angle of incidence,  $\theta$  and  $\phi$ , and contains both wave forms  $h_{+,x}^{TT}(f)$  as in Figure 1.2. In this case, we treat the amplitude of strain on the interferometer  $h(f)$ , as a linear combination of both wave forms in the frequency domain,

$$h(f) = F_+(\theta, \phi, \psi) h_+^{TT}(f) + F_\times(\theta, \phi, \psi) h_\times^{TT}(f) \quad (1.45)$$

where the amplitude depends on so-called “antennae patterns”  $F_{+,x}(\theta, \phi, \psi)$ ,

$$\begin{aligned} F_+(\theta, \phi, \psi) &= \frac{1}{2} (1 + \cos^2 \theta) \cos(2\phi) \cos(2\psi) - \cos \theta \sin(2\phi) \sin(2\psi) \\ F_\times(\theta, \phi, \psi) &= -\frac{1}{2} (1 + \cos^2 \theta) \cos(2\phi) \sin(2\psi) - \cos \theta \sin(2\phi) \cos(2\psi) \end{aligned} . \quad (1.46)$$

As expected, we see an incident gravitational wave will cause maximum strain amplitude if  $\theta = \psi = \phi = 0$ . We refer to such a gravitational wave as “optimally oriented,” where

$$\Delta L(f) = h_+^{TT}(f)L = h(f)L. \quad (1.47)$$

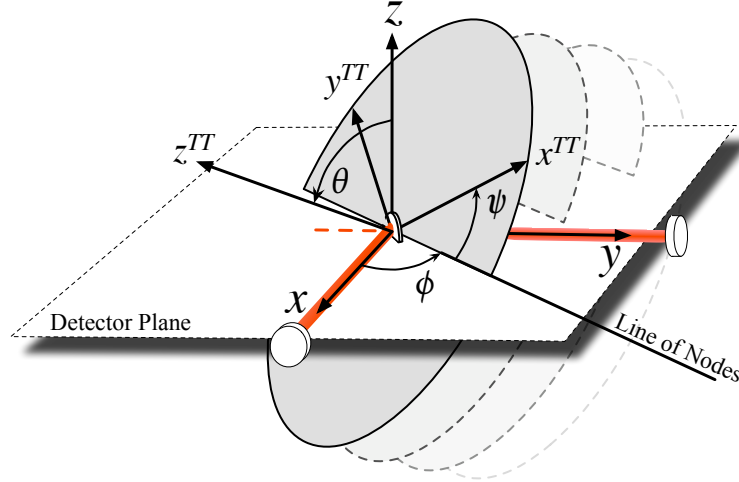


Figure 1.2: Euler angles,  $\theta$ ,  $\phi$  and  $\psi$  used to define the antenna patterns  $F_{+,x}(\theta, \phi, \psi)$ . The axis  $x^{TT}, y^{TT}$  are aligned with the lines of maximal strain for the plus polarization wave form.

As Equation 1.47 describes, if the interferometer measures relative changes in length  $\Delta L$ , then increasing the length of the interferometer arms  $L$  will produce a larger signal. The next chapter describes a network of suspended mass Michelson interferometers that has been built, whose arms are kilometers in length.

## 2. The Laser Interferometer Gravitational Wave Observatory

The Laser Interferometer Gravitational Wave Observatory (LIGO) is a network of three detectors built in the United States to detect local perturbations in the space-time metric from astrophysical sources (1). These distant sources, as described in Chapter 1, are expected to produce time-dependent strain amplitudes  $h(t) \sim 10^{-20}$  or less, observable by the interferometer array given sufficiently long measurement time-scales (17; 38). Figure 2.1 shows the originally expected strain sensitivity for these interferometers, in addition to the limiting noise sources which will be discussed further in Section 2.2.

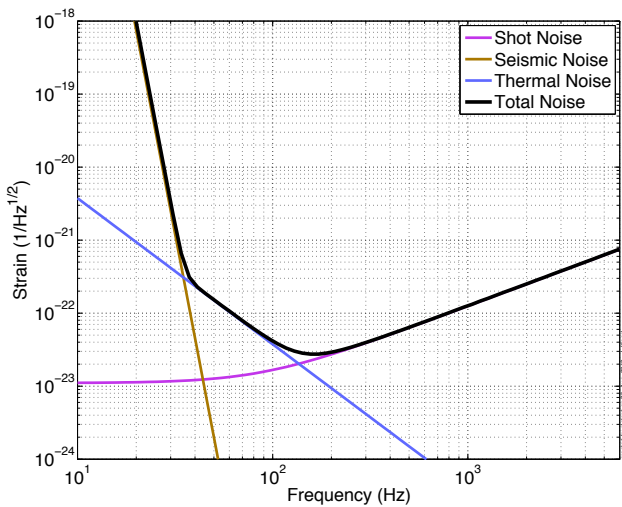


Figure 2.1: Strain sensitivity of the LIGO interferometers, adapted from original design (1).

### 2.1 Power-Recycled, Fabry-Perot Michelson Interferometers

The detectors, two in Hanford, WA (H1 and H2) and one in Livingston, LA (L1), are power-recycled Fabry-Perot Michelson interferometers. The optical layout of the interferometers is shown in Figure 2.2. The perpendicular Michelson arms are Fabry-Perot cavities, each of length  $L = 3995$  m for H1 and L1 ( $L = 2009$  m for H2). The cavities are produced by laser light resonating between two 10 kg, 25 cm diameter optics or “test masses,” with a partially transmissive input mirror and highly-reflective end mirror. Light reflected from the input port of the Fabry-Perot Michelson is recycled back into the interferometer with an additional optic forming a power recycling cavity. The interferometer receives light that is stripped of non-fundamental transverse spatial modes present in the laser field from an additional 12 m triangular ring cavity prior to the main interferometer known as the input mode cleaner.

The bulk material for all optics is ultra-pure fused silica  $\text{SiO}_2$ . Further, the optics have been coated with alternating layers of low ( $\text{SiO}_2$ ) and high ( $\text{Ta}_2\text{O}_5$ , “tantala”) index of refraction dielectric materials each of thickness  $\lambda/4$  in order to tune the cavity reflectivities.

The LIGO detectors have been built inside one of the world’s largest ultra-high vacuum enclosures. The detector must be under vacuum to remove air and dust particles which would cause insurmountable scattering of input light and phase fluctuations in the arm cavities mimicking gravitational wave strain. The test masses, beam splitter and corresponding suspension systems are enclosed in one of two types of vacuum chambers: the large “basic symmetric chamber” or BSC. The power recycling mirror, input mode cleaner, and other associated input and output optics are housed in smaller “horizontal access modules” or HAMs. Each of these chambers are connected by a series of large tubes (Figure 2.3), most notably the arm cavity tubes which are 1.2 m in diameter, and 4 km long.

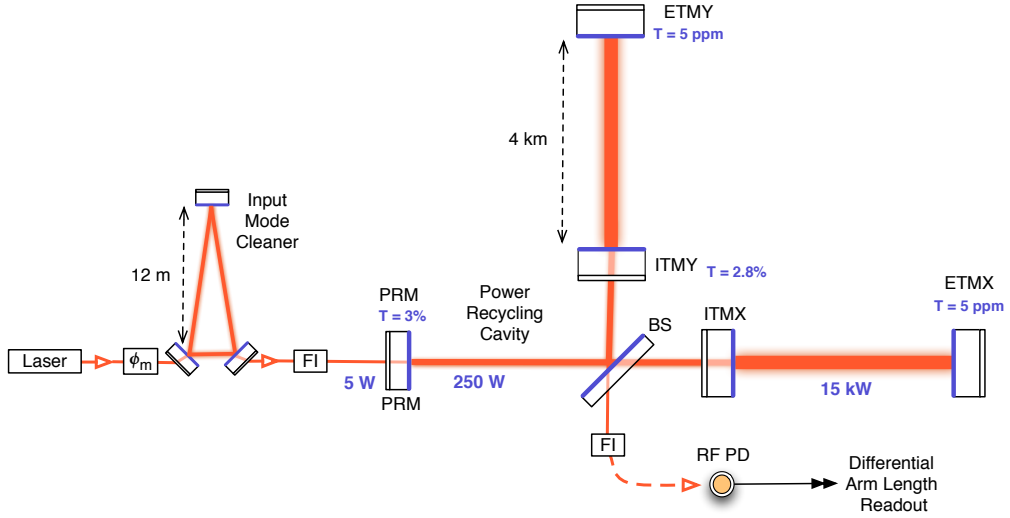


Figure 2.2: Optical layout for the LIGO interferometers. Pre-stabilized,  $\lambda = 1064$  nm, laser light is phase modulated by a Pockels cell  $\phi_m$ , then injected into the input mode cleaner. Stable, diffraction limited, light exits the mode cleaner, and is input into the interferometer. Light exiting both ports of the Michelson are optically isolated from the input and output optics and photodiodes using faraday isolators (FI). The power recycling cavity is formed by the power recycling mirror (PRM), the beam splitter (BS), and input test masses (ITMX, ITMY). The Fabry-Perot arm cavities are formed by the ITMs and the end test masses (ETMs).

All optics shown in Figure 2.2 are suspended with several layers of passive isolation in order to reduce motion from ground in gravitational wave band. The driving principle behind passive isolation is the ratio,  $P(f)$ , of the displacement,  $x(f)$ , of a pendulum’s center of mass,  $m$ , to a force  $F(f)$  input on its suspension point,

$$P(f) = \frac{x(f)}{F(f)} = \frac{1}{m} \frac{1}{(f_0^2 + i \frac{f_0}{Q}) f - f^2}, \quad (2.1)$$

where  $f_0$  is the natural resonance frequency,  $Q$  is the quality factor associated with damping,

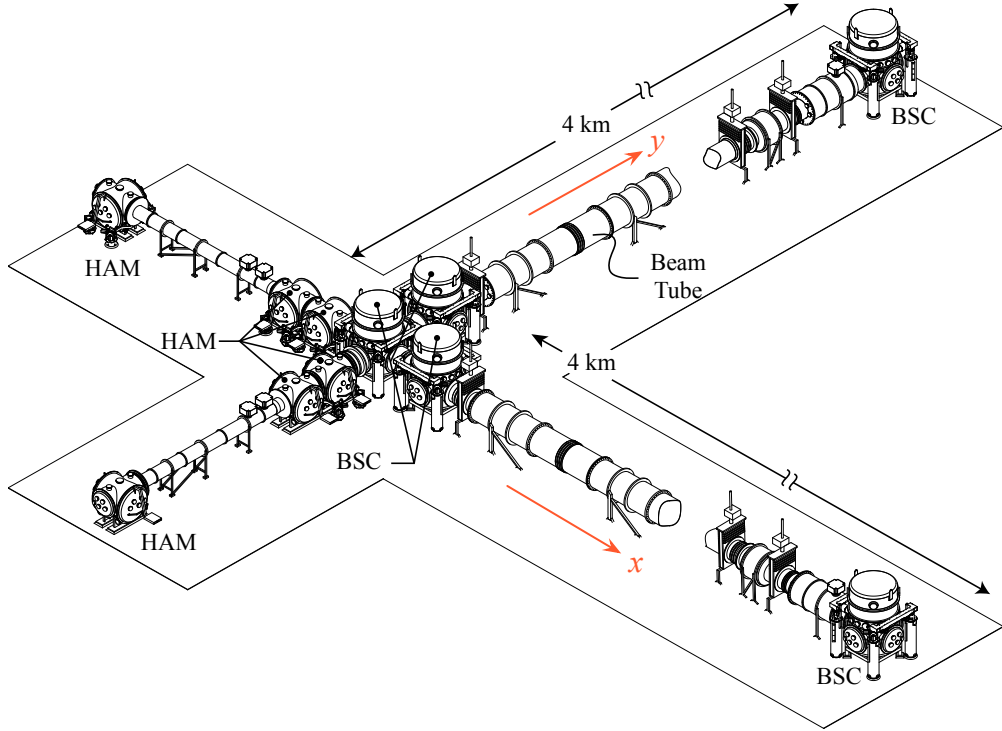


Figure 2.3: Rendering of the iLIGO vacuum system (2). The layout of the chambers follows the optical layout, where the vertex houses the beam splitter and two input test masses in the larger BSC-style chambers, and all input and output optics in the HAM-style chambers. The end test masses are also in BSC-style chambers at each end station.

and  $A$  is an amplitude scale factor that depends on the specifics of the pendulum (length, mass, etc.). When  $f \gg f_0$ , the transfer function simplifies to  $f^{-2}$ . Hence, if that driving force is ground motion, then at frequencies well above the natural resonance frequency, the pendulum's center of mass sees a reduction in ground motion by a factor  $f^{-2}$ . Further, if several pendula with similar resonant frequencies are suspended in a cascading fashion, each layer provides an additional  $f^{-2}$  above  $f_0$ . This principle has guided the design of the LIGO passive isolation system, shown in Figures 2.4 and 2.5. Figure 2.4 shows two types platforms (corresponding to the two types of vacuum chambers) from which the optics are suspended. They consist of 3 (for the HAM chambers) and 4 (for the BSC chamber) layers of mass elements connected to, or suspended from, damped coil springs forming cascading stages of pendula as described above (3; 44). Figure 2.5 shows a schematic of the final stage of suspension system for a given optic. The optics are hung from a rigid support structure using 300  $\mu\text{m}$  thick steel wire looped around the cylindrical barrel, guided by small extensions to the barrel. The support structure is fixed to the optical platform of the mass-spring system. Each of these stages of isolation are designed to have resonant frequencies between 1 and 10 Hz, such that in the band where we expect gravitational waves,  $f_{GW} \sim 100$  Hz, the optics are displaced many orders of magnitude less than ground motion.

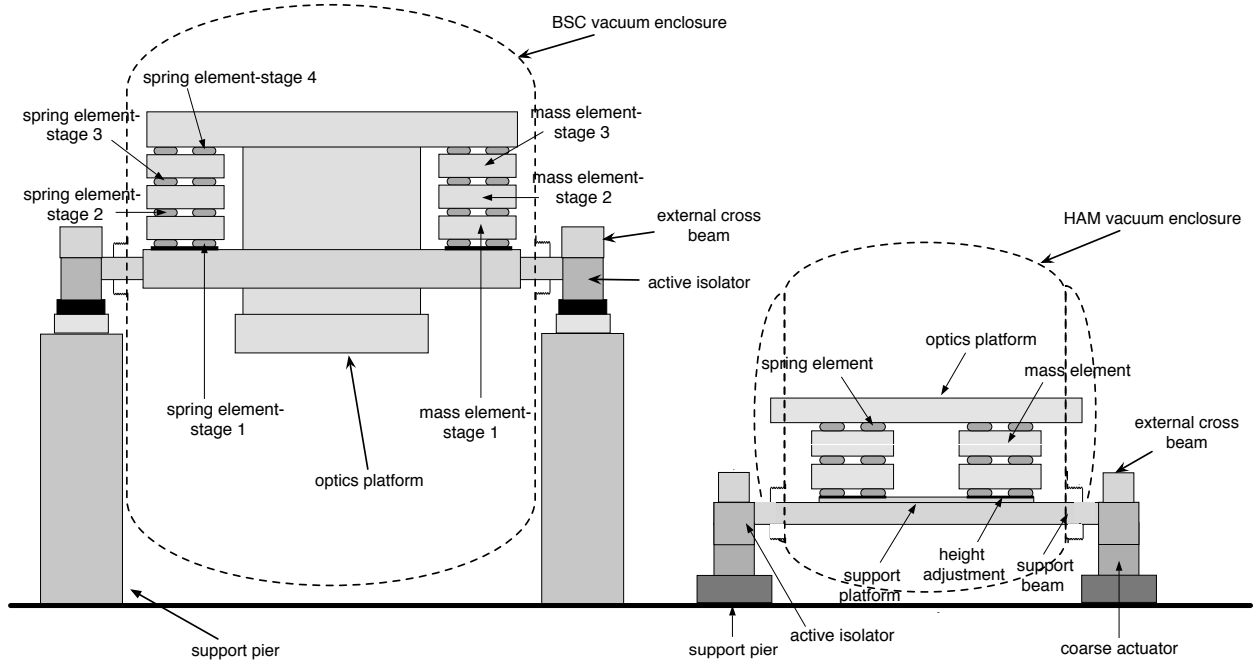


Figure 2.4: Schematic of Initial LIGO seismic isolation for BSC chamber (left) and HAM chamber (right), adapted from (3). For the BSC chambers, there is a single layer of active external pre-isolation, and four layers of passive isolation. For the HAM chambers, there is also a single layer of active external pre-isolation, but has only three layers of passive isolation. The support structure of the final layer of suspensions (Figure 2.5), is hung from or mounted on the optics platform for the BSC or HAM stacks, respectively.

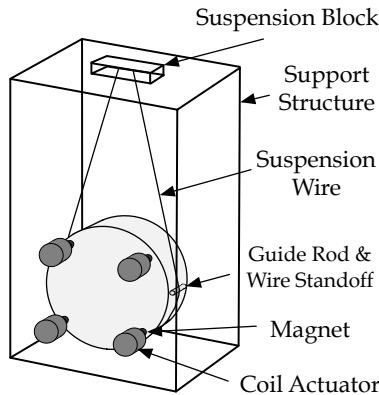


Figure 2.5: A schematic of the LIGO optic suspensions for S5. Actuation force is provided by the coil actuators (mounted to the support structure) which act upon the magnets secured directly on the rear face of the optic.

While under the influence of residual displacement from ground, even through the seismic isolation system, the power-recycled Fabry-Perot Michelson interferometer is an inherently non-linear device. Active feedback control of the interferometer is an essential part of reducing this residual motion to where the readout is linearly proportional to the differential arm length changes; the degree of freedom designed to be most sensitive to gravitational wave strain. Each interferometer uses a Nd:YAG solid-state laser ( $\lambda = 1064$  nm) for the primary laser field. The control system must keep the round-trip lengths of the cavities near integer multiples of the laser wavelength so that newly introduced input light constructively interferes with previous round trips. Under these conditions, the light inside the cavity builds up and they are said to be “on resonance” or “locked.” Figure 2.6 shows a comparison between the displacement noise of the changes in differential arm length in absence of control and while under control. Implementation of feedback control requires a detection scheme which independently senses all longitudinal degrees of freedom in the interferometer. As such, the input laser field’s phase is modulated at several frequencies (typically tens of MHz), generating fluctuations of the primary field known as “sidebands.” The carrier and sideband fields reflected from each cavity are measured by a series of independent photodiodes such that a Pound-Drever-Hall style control scheme (45; 46) can be used with actuation force supplied by electro-magnetic coil-actuators (paired with magnets secured on the rear face of the optics). Further discussion of this control system is reserved for Chapter 3.

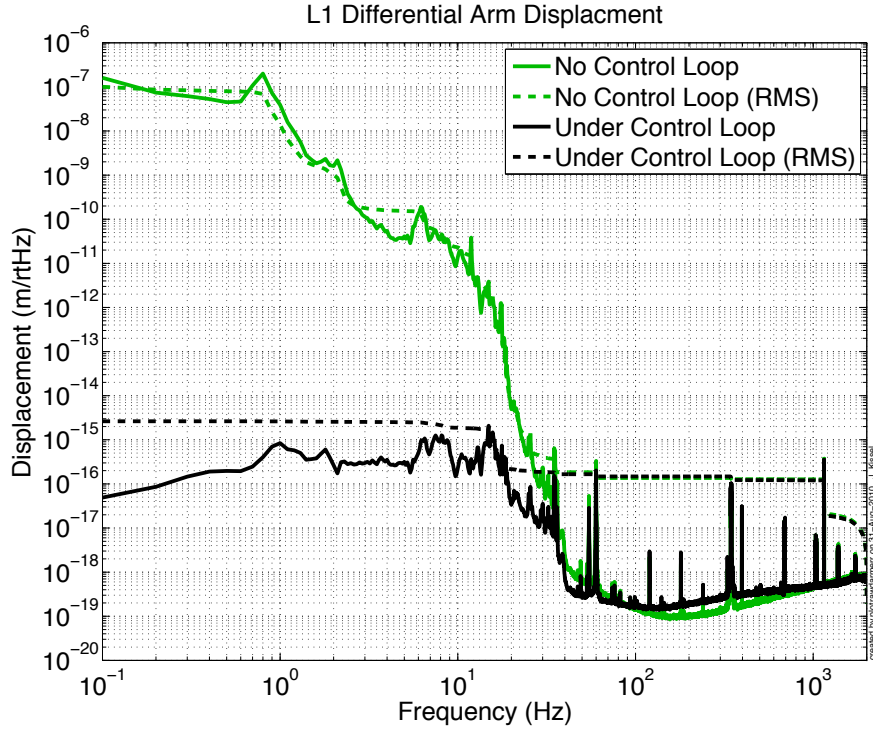


Figure 2.6: Amplitude spectral density of the differential arm length for the Livingston interferometer. We show the control loop reduces the residual RMS ground motion by more than seven orders of magnitude when the interferometer operates at designed sensitivity.

## 2.2 Fundamental Noise Sources

There are three fundamental sources of noise that limit each interferometer's sensitivity. With the suspension systems described in section 2.1, the seismic displacement noise defines the limit of the spectrum from 40Hz and below, described roughly by the  $f^{-10}$  slope created by the 5 passive isolation stages of the end test masses. This noise limit is often referred to as the “seismic wall” because of its characteristically steep slope.

Above  $\sim 200$  Hz, the interferometers are designed to be limited by sensing noise. The fundamental limit in sensing noise is the uncertainty in photon counting or “shot noise,” originating from discrete quantum nature of light and the Heisenberg uncertainty principle. A simple Michelson interferometer (Figure 1.1) has shot noise which takes the form

$$n_{\text{shot}}^{\text{MI}}(f) = \frac{1}{L} \sqrt{\frac{\hbar c \lambda}{2\pi\eta P_{\text{BS}}}} \quad (2.2)$$

where  $\hbar$  is Planck’s constant,  $\eta$  is the photodiode quantum efficiency,  $c$  is the speed of light,  $P_{\text{BS}}$  is the power incident on the beam splitter (32). Gravitational waves in the band of interest have  $f_{\text{GW}} \sim 150$  Hz, or wavelength  $\lambda_{\text{GW}} \sim 2000$  km. A Michelson interferometer achieves maximum sensitivity when the light spends half a gravitational wave period in the arms (32; 47), requiring a length of  $L = \lambda_{\text{GW}}/2 = 1000$  km. Even for such long arm lengths, a  $P_{\text{BS}} \sim 50$  W would be required to achieve an shot noise equivalent to a strain of  $10^{-21}$ . Such arm lengths are hopelessly impractical to build, and sufficiently stable,  $\lambda = 1064$  nm lasers with 50 W output power did not exist (as of the 1990s). To reduce the length of the arms, LIGO has two distinct improvements to the basic Michelson in order to increase the sensitivity. The first is the use of Fabry-Perot resonant cavities for arms whose finesse,  $\mathcal{F} \sim 220$ . For a such an interferometer, referred to as a Fabry-Perot Michelson (FPM), the shot noise improves to

$$n_{\text{shot}}^{\text{FPM}} = \sqrt{\frac{\pi\hbar\lambda}{c\eta P_{\text{BS}}}} \left( \frac{\sqrt{1 + (4\pi f\tau_s)^2}}{4\pi\tau_s} \right) \quad (2.3)$$

where  $f$  is the gravitational wave frequency, and  $\tau_s = 2\mathcal{F}L/\pi c$ , is the light storage time in the arm cavity (48). Figure 2.7 demonstrates the improvement in shot noise gained by replacing the arms of a Michelson interferometer with Fabry-Perot arm cavities. The second modification decreases the required input power with the addition of a partially transmissive mirror at the symmetric port, forming an additional “power-recycling” cavity with the Fabry-Perot Michelson. In this configuration, for the power-recycled Fabry-Perot Michelson, the power at the beam splitter<sup>2</sup> is increased by a factor

$$g_{\text{pr}} = \frac{r_p}{1 + r_p r_c} \quad (2.4)$$

where  $r_p$  is the (amplitude) reflectivity of the the power recycling mirror, and

$$r_c = \frac{r_i - r_e}{1 - r_i r_e} \quad (2.5)$$

with  $r_i$  and  $r_e$  as the input and end test mass (amplitude) reflectivities (49). For the first generation LIGO cavities where  $T_p = T_i = 0.027$ , and  $T_e = 5 \times 10^{-6}$  the arm cavities are slightly over-coupled such that the arm cavity reflectivity is  $r_c \sim -0.9996$ , creating a recycling cavity gain of  $g_{\text{pr}} \sim 70$  (48).

---

<sup>2</sup>when the cavities are on resonance, and with loss is neglected, or  $T = 1 - r^2$

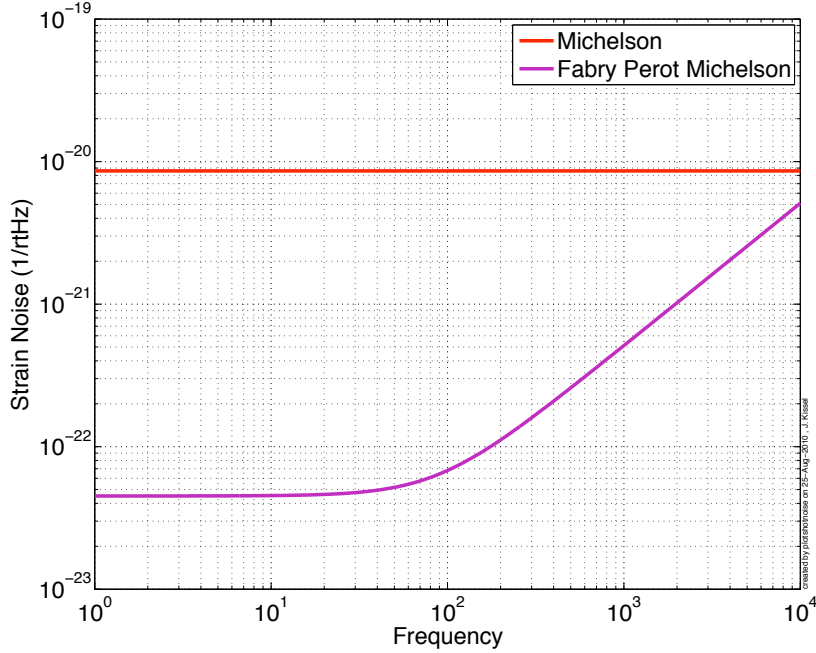


Figure 2.7: Comparison between the shot noise of Michelson and Fabry-Perot Michelson interferometers, for the same input power of  $P_{BS} = 5$  W. The other parameters of the noise are that of the first generation LIGO detectors:  $L = 4$  km,  $\lambda = 1064$  nm,  $\mathcal{F} = 220$ , and  $\eta = 0.9$ .

Thermal noise of the optics and suspension systems dominate the frequency band between that created by the seismic and shot noise limits. While in ultra-high vacuum, the interferometer optics and suspensions are still at room temperature. At designed sensitivity, the Brownian motion of the bulk material, surface coatings, and suspension wires incoherently displace the face of the test masses, and appears as noise referred to collectively as “thermal noise.” The frequency spectrum of this noise is associated with energy dissipation in the materials, in accordance with the fluctuation-dissipation theorem (50; 32). This theorem states the power spectrum of a system’s thermal displacement noise is given directly as

$$x^2(f) = \frac{k_B T}{\pi^2 f^2} \Re e(Y(f)) \quad (2.6)$$

where  $k_B$  is Boltzmann’s constant,  $T$  is the temperature of the system, and  $Y(f)$  is the admittance of the system. The energy dissipation, or “loss,” is folded into often complicated expressions for  $Y(f)$ . The suspension wires, the test mass, and its coating can be described by damped harmonic oscillators, which obey Hooke’s law,

$$F = -k(1 + i\phi)\delta x \quad (2.7)$$

where the stiffness  $k$  is complex, with any dissipation terms folded into the imaginary part referred to as the “loss angle,”  $\phi$ , which can be itself frequency-dependent. However, the

admittance function is different for each mechanism, resulting in a different frequency dependence for each. For the suspension thermal noise (32), the spectrum is defined by

$$x_{sus}^2(f) = \frac{4k_B T k \phi}{2\pi f [(k - m(2\pi f)^2)^2 + k^2 \phi^2]} \propto f^{-5} \quad (2.8)$$

and for the internal thermal noise of the test mass coating (51),

$$x_{int}^2(f) = \frac{2k_B T \phi_{eff}(1 - \sigma)}{\pi^{3/2} w E f} \propto f^{-1} \quad (2.9)$$

where  $w$  is the half-width of the incident Gaussian laser profile, and  $\phi_{eff}$  is the effective loss angle, a function of the Poisson ratios,  $\sigma$ , Young's modulus,  $E$ , and loss angles of both the substrate and coatings. The dominant source of dissipation for the substrate-coating system is the high-index material, tantalum  $Ta_2O_5$ . The total thermal noise dominates the sensitivity between 40 Hz and 200 Hz, with suspension thermal noise from 40 to 100 Hz, and coating thermal noise from 100 to 200 Hz (48).

## 2.3 The Fifth Science Run

Construction of the LIGO interferometers as described in section 2.1 was completed in the late 1990s, however it took several years of commissioning and brief data collection periods, or “science runs,” before they operated at designed sensitivity (i.e. at the intended sensitivity shown in Figure 2.1). During the fifth LIGO science run (S5), these detectors accumulated approximately one year (368.84 days) of triple coincidence data near their designed sensitivity between Nov 4 2005 and Oct 1 2007. The best sensitivity, determined by amplitude spectral density (see Appendix A for details) of the displacement noise, for each detector and an example sensitivity curve describing the fundamental noise sources for the 4 km detectors (1) are shown in Figure 2.8.

While Figure 2.8 displays the best sensitivity achieved during S5, the interferometers exhibit both short- and long-term variations in sensitivity from seasonal and daily variations in the environment, improvements made to the instruments over the course of the run, et cetera. As a figure of merit of the sensitivity over time, we integrate the power spectral density using a matched-filter template describing a binary neutron star (1.4-1.4 solar mass) coalescence over which angle and orientation have been averaged. This metric produces a predicted range out to which we may see such a source with signal-to-noise ratio of 8 (see (52) for details). Figure 2.9 illustrates the daily median of this range over the course of the science run.

Calibrating the output of the power-recycled Fabry-Perot Michelson into physical units displayed in Figures 2.8 and 2.9 is a critical part of the experiment. However, the fundamental challenge of this task is that the interferometer cannot operate at unless its cavities are locked on resonance. Therefore the control and actuation systems must be well understood in order to remove their response from the sensing system. Several techniques and measurement suites have been developed for the S5 run to characterize all components of the interferometer control loop and determine the absolute measurement scale and frequency response of LIGO detectors. We discuss this procedure and resulting uncertainty in great detail in Chapter 3.

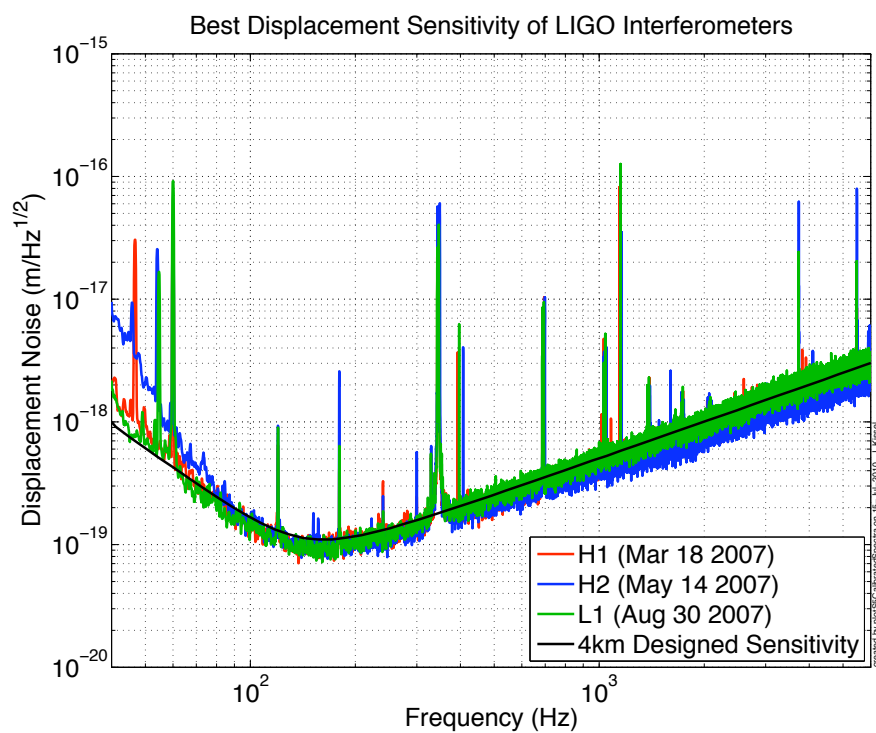


Figure 2.8: The best displacement sensitivity, expressed as equivalent displacement noise, for each interferometer during the S5 science run, and expected total noise in LIGO's first 4 km interferometers.

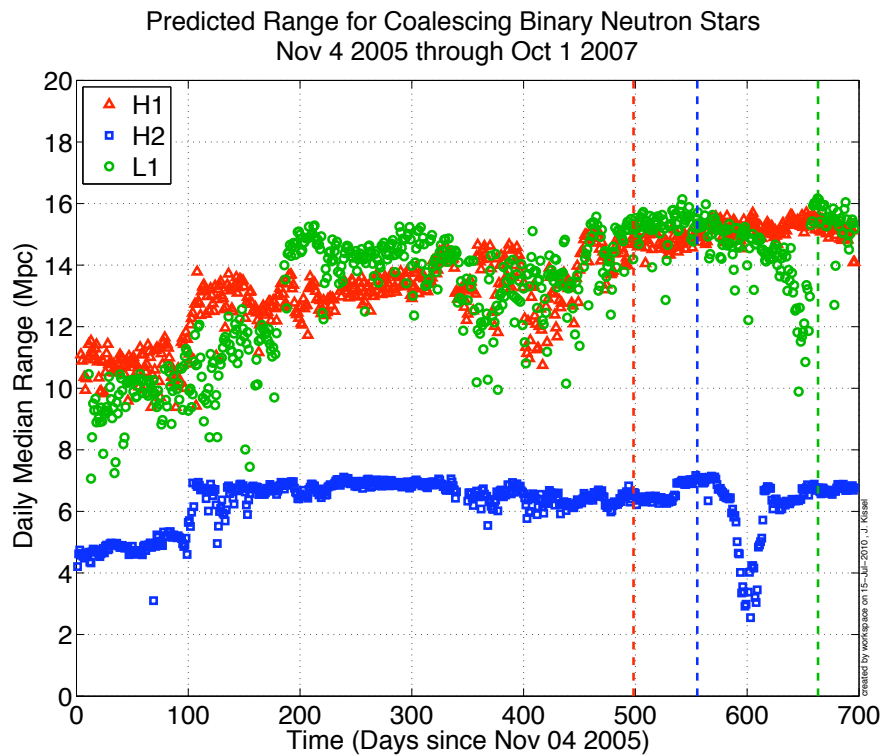


Figure 2.9: Daily median of detector sensitivity during S5 to a 1.4-1.4 solar mass compact binary system averaged over angle and orientation. Dashed lines indicate the times during which the representative spectra in Figure 2.8 were taken. Large variations in detector sensitivity are due to upgrades or hardware problems.

### 3. Calibration of the LIGO Detectors <sup>3</sup>

Differential changes of the interferometer's Fabry-Perot arm cavity lengths are measured by precisely monitoring the phase between light returned by each cavity using a Pound-Drever-Hall error signal. When the interferometer is under servo control, this error signal,  $e_D(f)$ , is the recorded data stream that is probed for the presence of gravitational wave strain. The error signal is proportional to a differential arm length change,  $\Delta L_{ext}(f)$  caused by the end test mass displacement such that,

$$\Delta L_{ext}(f) = R_L(f) e_D(f) \quad (3.1)$$

where the change in length  $\Delta L_{ext}$  is the sum of the interferometer's response to the astrophysical signal and other differential noise sources.

The quantity  $R_L(f)$  is a complex function in the frequency-domain known as the "length response function." In this chapter, we provide a complete description of a frequency-domain model of the length response function used for each detector in the S5 data set. In Section 3.1, we describe the model used for all LIGO interferometers which divides a given interferometer into three major subsystems – sensing, digital control, and actuation – and includes a detailed description of the important components of each subsystem. Measurements of these components along with corresponding uncertainties are presented in Section 3.2. Finally, the response function,  $R_L(f)$ , is developed from the subsystems and the uncertainty in each subsystem are combined in Section 3.3 to form the total uncertainty estimate.

Searches for gravitational wave strain are performed on the error signal in the time domain, from  $e_D(t)$  and a convolution kernel,  $R_L(t - t')$ ,

$$h(t) = \frac{1}{L} \int R_L(t - t') e_D(t') dt', \quad (3.2)$$

where  $R_L(t - t')$  is developed from the parameters of the length response function,  $R_L(f)$ . The production of the time-domain convolution kernel,  $R_L(t - t')$ , from the frequency-domain model,  $R_L(f)$ , and the associated additional uncertainty are discussed in detail in (54; 55).

#### 3.1 Model

Astrophysical gravitational wave strain  $h(f)$  detected by the interferometers contains source information including wave forms  $h_{+,\times}(f)$ , azimuthal angle  $\phi$ , polar angle  $\theta$ , and orientation (or polarization angle)  $\psi$  (see Figure 1.2). The amplitude of the wave's projection into the interferometer basis,  $h(f)$ , is described by Eq. 1.45.

We model each interferometer's response to an optimally-oriented ( $\theta = \phi = \psi = 0$ ), plus-polarized wave form using the long wavelength approximation, where the gravitational wave wavelength is much larger than the 4 km arm cavities. The approximation is valid between 40 and 6000 Hz, and has associated uncertainty of at most 2% (56). From this reference model, the detector response to an arbitrary waveform, orientation, and polarization angle

---

<sup>3</sup>Much of the material presented in this chapter has been published in (53) and is reproduced here with expressed permission from Dr. William Barletta, Coordinating Senior Editor of Nuclear Instruments and Methods A (see Appendix E).

may be calculated analytically (as described by Eq. 1.46 and (17; 57; 58)). In the long wavelength approximation, the strain amplitude,  $h(f)$ , in Fabry-Perot arm lengths of the interferometer is

$$h(f) = \frac{L_{ext}^x(f) - L_{ext}^y(f)}{L} = \frac{\Delta L_{ext}}{L}, \quad (3.3)$$

(cf Eq. 1.47).

Feedback control systems are used to hold the interferometer in a regime where the digital error signal,  $e_D(f)$ , is linearly related to the DARM length,  $\Delta L_{ext}$ , (as in Eq. 3.1) and hence to the gravitational wave strain,  $h(f)$ . We model this control loop as a single-input, single-output control loop depicted in Figure 3.1.

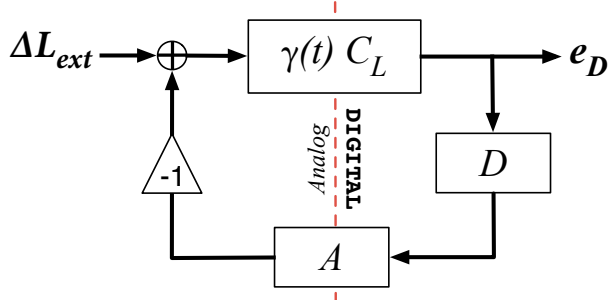


Figure 3.1: The model of the control loop for differential changes in length of the Fabry-Perot arm cavities. The interferometer senses a change in DARM length,  $\Delta L_{ext}$  according to  $\gamma(t)C_L(f)$ , the result of which is the digital error signal  $e_D$ , which is then fed back through a set of digital filters  $D(f)$ , and converted to analog control via the actuation function of the end test masses  $A(f)$ .

The loop contains three major subsystems. First is the length sensing function,  $C_L(f, t)$ , which describes how the interferometer responds to differential changes in arm lengths and how that response is digitized. This function is separated into a frequency-dependent function  $C_L(f)$  which may have some slow time dependence captured by a factor  $\gamma(t)$ .  $D(f)$  is a set of digital filters, used to shape the loop error signal into a control signal. The remaining subsystem is the actuation function,  $A(f)$ , which describes how the test masses physically respond to the digital control signal. We assume linear relationships between all subsystems, such that any subsystem (and internal components) may be defined by the ratio of output over input signals.

The product of frequency-dependent subsystems inside the control loop is the “open loop transfer function”  $G_L(f)$ ,

$$G_L(f) = C_L(f)D(f)A(f). \quad (3.4)$$

Using the above model, we derive the length response function,  $R_L(f, t)$ , in terms of these functions to be

$$R_L(f, t) \equiv \frac{1 + \gamma(t)G_L(f)}{\gamma(t)C_L(f)}. \quad (3.5)$$

The remainder of this section describes the components of each subsystem in the control loop.

### 3.1.1 Sensing Function

The length sensing function,  $C_L(f, t)$ , describes the transfer function between the residual change in DARM length,  $\Delta L(f)$ , and the digital error signal,  $e_D(f)$ ,

$$C_L(f, t) = \gamma(t) \frac{e_D(f)}{\Delta L(f)}. \quad (3.6)$$

It is important to note that this linear relationship between the differential arm length change and the digital error signal only applies when the detector is under control of the feedback loop: in Eq. 3.6,  $\Delta L(f)$  is the residual external DARM length change,  $\Delta L_{ext}(f)$ , after the controlled length change,  $\Delta L_A(f)$ , is applied. The sensing function has several components (shown in Figure 3.2) which are treated independently,

$$C_L(f, t) = \gamma(t) \times \mathcal{K}_C \times [C_{FP}(f) \times ADC(f)]. \quad (3.7)$$

The constant,  $\mathcal{K}_C$ , holds all frequency-independent scaling factors, and has dimensions of digital counts of error signal per unit change in differential arm length. The remaining terms in Eq. 3.7 are dimensionless, including time dependence, treated independently in the coefficient  $\gamma(t)$ .

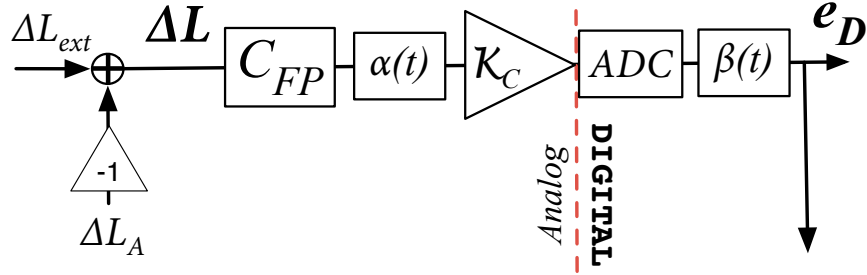


Figure 3.2: Schematic breakdown of the sensing function  $C_L(f, t)$ . Internal to the LIGO Scientific Collaboration, the digital signal  $e_D$  is often colloquially referred to by its digital “channel” name DARM\_ERR. From left to right,  $C_{FP}(f) \propto H_{FP}^x + H_{FP}^y$  is the arm cavity transfer function;  $\alpha(t)$  is the time-dependent variation of the interferometer’s input laser power and optical gain;  $\mathcal{K}_C$  is the scaling coefficient which absorbs all constants including the input laser power, optical gain, the quantum efficiency of the photodiodes, the impedance of the photodiode circuitry, and the analog-to-digital gain;  $ADC(f)$  is the frequency dependence of the analog to digital conversion; and  $\beta(t)$  is the digital factor which compensates for the analog change  $\alpha(t)$ . The compensation is not perfect, therefore the factor  $\gamma(t) \equiv \alpha(t)\beta(t)$  represents the residual variation.

The change in each arm cavity length,  $L$ , affects the phase of the laser’s electric field returning from the cavity. On resonance, the transfer function,  $H_{FP}(f)$ , between the change in electric field phase reflected by the cavity input mirror and a change in cavity length is

$$H_{FP}(f) = \frac{2\pi r_e(1 - r_i^2)}{\lambda(r_i - r_e)} \frac{\sin(2\pi f L/c)}{2\pi f L/c} \frac{e^{-2\pi i f L/c}}{1 - r_i r_e e^{-4\pi i f L/c}} \quad (3.8)$$

where  $\lambda$  is the laser wavelength,  $r_i$  and  $r_e$  are the amplitude reflectivity of the input and end test masses, and  $c$  is the speed of light. In the frequency band considered for analysis, where  $40 \text{ Hz} < f < 6 \text{ kHz} \ll 2c/L$ , the frequency-dependence of  $H_{FP}(f)$  is approximated by a simple “cavity pole” transfer function,

$$H_{SP}(f) \equiv \frac{H_{FP}(f \ll c/2L)}{H_{FP}(0)} \approx \frac{1}{1 + i \frac{f}{f_c}}, \quad (3.9)$$

where  $f_c = c(1 - r_i r_e)/4\pi L \sqrt{r_i r_e}$  (49; 56; 59; 60; 61).

The LIGO detectors use a Pound-Drever-Hall detection scheme to extract this phase information from the arm cavities, which is recombined at the beam splitter. The laser electric field input into the interferometer is phase-modulated at  $\omega_m/2\pi = 25 \text{ MHz}$ , which effectively splits the field into a “carrier” field with the original laser frequency,  $\Omega$ , and upper and lower “sideband” fields with frequency  $\Omega \pm \omega_m$ . The sideband fields resonate in the power recycling cavity but are anti-resonant in the arm cavities, and therefore, unlike the carrier field, experience no phase change from the arm cavity length variation. The Michelson is set up with a fixed “Schnupp” asymmetry (62) such that, at the anti-symmetric port, the carrier field is held on a dark fringe and the sideband fields are not. In this setup, when the arm cavity lengths change differentially, the carrier field moves away from the dark fringe, mixes with the sideband field at the antisymmetric port, and a beat signal at  $\omega_m$  is generated.

The power of the mixed field at the antisymmetric port (in Watts) is sensed by four photodiodes. The photocurrent from these diodes is converted to voltage, and then demodulated at 25 MHz. This demodulated voltage signal,  $V_D(f)$  (and therefore the differential change in arm lengths) is proportional to power of the input laser field,  $P_{in}$ , the “optical gain” (the product of Bessel functions of modulation strength,  $J_0(\Gamma)$  and  $J_1(\Gamma)$ , the recycling cavity gain,  $g_{rc}$ , the transmission of the sidebands into the antisymmetric port from the Michelson asymmetry  $t_{sb}$ , and the reflectivity of the arm cavities for the carrier,  $r'_c$ ), the quantum efficiency of the photodiodes  $\eta$ , and the impedance of the photodiode circuitry  $R_{pd}$ ,

$$\frac{V_D(f)}{\Delta L_{ext}(f)} = -8P_{in}J_0(\Gamma)J_1(\Gamma)g_{rc}t_{sb}r'_c\eta R_{pd} \frac{2\pi}{\lambda} \frac{1}{1 + i \frac{f}{f_c}} \quad (3.10)$$

where

$$\begin{aligned} r_c &= \frac{(r_e - r_i)}{(1 - r_i r_e)}, & r'_c &= \frac{r_e(1 - r_i^2)}{(1 - r_i r_e)^2}, \\ g_{rc} &= \frac{t_r}{1 - r_r r_c}, & t_{sb} &= \frac{t_r \sin(2\omega_m \delta/c)}{1 - r_r \cos(2\omega_m \delta/c)}, \end{aligned} \quad (3.11)$$

$\Gamma$  is the modulation strength,  $\omega_m$  is the modulation frequency,  $\delta$  is the Schnupp asymmetry,  $c$  is the speed of light, and  $r_r$ ,  $r_e$ , and  $r_i$  are the amplitude reflectivities of the recycling mirror, end, and input test masses (61; 46; 49; 60). Note that, in practice,  $V_D(f)$  contains signal proportional to the differential changes in Michelson arm lengths (the distance from the beam splitter to each input test mass), but is ignored in this discussion as we focus only on the degree of freedom most sensitive to gravitational waves.

The demodulated voltage from the photodiodes is whitened, and anti-aliased with analog circuitry and then digitized by an analog-to-digital converter which scales the voltage to digital counts. The frequency dependence of the anti-aliasing filters and digitization process is folded into the function  $ADC(f)$ . We absorb all proportionality and dimensions of this

process into the single constant,  $\mathcal{K}_C$ , having dimensions of digital counts per meter of DARM test mass motion.

The optical gain is time-dependent because small, low-frequency ( $f \ll 40$  Hz) alignment and thermal lensing fluctuations in the resonant cavities change the carrier and sideband field amplitudes. The input laser power may also fluctuate from similar alignment and thermal effects. We represent these variations with a coefficient,  $\alpha(t)$ . The input power, along with the carrier and sideband power stored in the cavities, are monitored by several independent photodiodes. Their signals are also digitized and combined to form a coefficient,  $\beta(t)$ , used to digitally compensate for the time-dependent variations. The compensated anti-symmetric port signal forms the error signal for the DARM control loop,  $e_D(f)$ . The sensing function therefore depends on both time and frequency, but can be separated into independent components  $C_L(f, t) = \gamma(t)C_L(f)$ , where

$$C_L(f) \propto C_{FP}(f) \times ADC(f) = [H_{SP}^x(f) + H_{SP}^y(f)] \times ADC(f) \quad (3.12)$$

and

$$\gamma(t) \equiv \alpha(t)\beta(t) \quad (3.13)$$

is the scale factor of order unity accounting for the residual time dependence after compensation.

### 3.1.2 Digital Filters

The digital filters,  $D(f)$ , are known functions in the model. These filters are used to shape the digital DARM control loop error signal,  $e_D(f)$  (in digital counts proportional to displacement) into a digital control signal,  $s_D(f)$  (in digital counts proportional to force),

$$D(f) = \frac{s_D(f)}{e_D(f)} \quad (3.14)$$

Over the course of the science run, discrete changes are made to the digital filters,  $D(f)$ , to improve the performance and stability of the detector (four times in the Hanford interferometers, three in Livingston). These changes significantly alter the frequency-dependence of the DARM control loop, and hence affect the overall response function of the interferometer. We divide the run into “epochs” defined by these changes.

Note that the digital filter component does not include all digital filters in the DARM loop. Both the sensing function and the actuation function contain digital filters, but their frequency dependence is either negligible in the measurement band, only important in a very narrow frequency range, or are compensating for analog circuitry whose product with the digital filters form a unity transfer function. We include these filters in their respective sub-systems for completeness.

### 3.1.3 Actuation Function

The actuation function  $A(f)$  is defined by the transfer function between the digital control signal,  $s_D(f)$ , and the physical motion imposed on the end test masses by the control loop,  $\Delta L_A$ ,

$$A(f) = \frac{\Delta L_A}{s_D(f)}, \quad (3.15)$$

and has units of end test mass displacement in meters per count of digital control signal. We describe the actuation function as a linear combination of functions for each test mass,

$$A(f) = \xi^x A^x(f) + \xi^y A^y(f). \quad (3.16)$$

where  $\xi^{x,y}$  are known digital coefficients of order unity, roughly equivalent, but opposite in sign. Once split, the control signal flows through each component to the end test masses as shown in Figure 3.3.

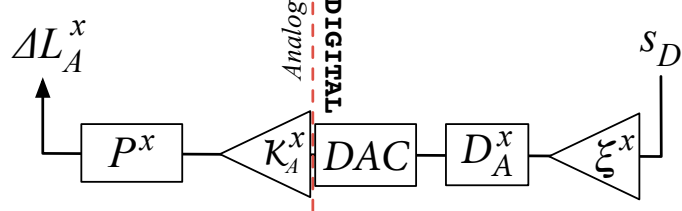


Figure 3.3: Schematic breakdown of the signal flow through the actuation function for the X arm  $A^x(f)$ . The digital signal  $s_D(f)$  is colloquially referred to by its “channel” name DARM\_CTRL. From right to left,  $\xi^x$  is the fraction of the digital control signal sent to the X arm;  $D_A^x(f)$  are digital filters;  $DAC(f)$  is the frequency dependence of digital to analog conversion;  $K_A^x$  is the scaling coefficient proportional to the digital-to-analog gain, the gain of resistance circuitry which converts voltage to current, the gain of the coil actuators which convert current to magnetic force, and the force-to-displacement transfer function gain; and  $P^x$  is the frequency dependence of the force-to-displacement transfer function.

For each arm, the digitally split control signal passes through digital suspension filters,  $D_A(f)$ , and is converted from digital signal to an analog voltage via the digital to analog conversion element,  $DAC(f)$ , which includes analog anti-imaging circuitry. The resulting voltage passes through a resistance circuit converting it into current, and is sent to the coil actuators which convert the current into force on the magnets attached to the end test mass. The suspended test mass is displaced according to the force-to-displacement transfer function,  $P(f)$ , changing each arm cavity length,  $\Delta L_A(f)$ . The arm’s scaling coefficients,  $\mathcal{K}_A$ , absorb all dimensions and frequency-independent factors in the actuation path. This includes the digital-to-analog gain, the gain of the resistance circuitry, the gain of the coil actuators, and the force-to-displacement transfer function scale factor. In summary, we express the individual end test mass actuation functions in Eq. 3.16 as

$$A^{x,y}(f) = \mathcal{K}_A^{x,y} \times [D_A^{x,y}(f) \times DAC(f) \times P^{x,y}(f)]. \quad (3.17)$$

The actuation coefficients,  $\mathcal{K}_A$ , scale the arbitrary counts of digital excitation force into meters of test mass motion. The remaining terms in Eq. 3.17 are dimensionless.

The suspended test mass can be treated as a pendulum driven by the coil actuators (see Figure 2.5). The force-to-displacement transfer function for the center of mass of a pendulum,  $P_{cm}(f)$ , is

$$P_{cm}(f) \propto \frac{1}{[f_0^{cm}]^2 + i \frac{[f_0^{cm}]}{Q^{cm}} f - f^2} \quad (3.18)$$

where  $f_0^{cm}$  and  $Q^{cm}$  are the frequency and quality factor of the pendulum. A rigid body resonant mode akin to the fundamental mode of a cylindrical plate (4) (see Figure 3.4) known as the “drumhead” mode is also included in the force-to-displacement model. Its radially-symmetric shape, excited by the actuators, lies directly in the optical path and amplifies the cavity’s response to the length control signal above a several kHz (5). We approximate the effects of the resonance by multiplying  $P_{cm}(f)$  by an additional pendulum transfer function,  $P_{dh}(f)$ , defined by frequency,  $f_0^{dh}$ , and quality factor,  $Q^{dh}$ . The total force-to-displacement transfer function is

$$P(f) \propto P_{cm}(f)P_{dh}(f) \quad (3.19)$$

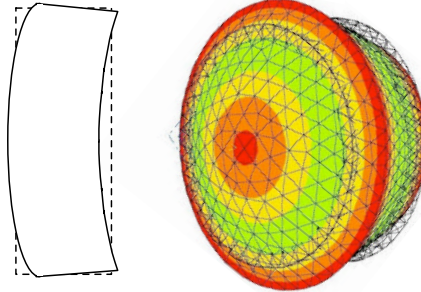


Figure 3.4: Physical shape of the end test mass drumhead internal resonance. Left: Cartoon, edge-on view of the fundamental mode of a cylindrical plate (4). Right: Three dimensional modal shape of the drumhead resonance from finite element analysis of a cylinder with dimensions similar to the LIGO test masses (5).

The digital suspension filters,  $D_A(f)$ , are between the split control signal and the digital-to-analog converter. Their purpose is to remove control signal in narrow frequency ranges around the frequencies of other in-band, non-axisymmetric, rigid-body resonant modes of the test masses that are excited by the actuation forces (5), and to reduce the coupling between DARM length motion and angular motion of the test mass.

## 3.2 Measurements

Each subsystem of the response function  $R_L(f)$  is developed using measurements of key parameters in their modeled frequency dependence and their scaling coefficients. The digital filter subsystem is completely known; its frequency dependence and scaling coefficient are simply folded into the model of the response function. The parameters of the frequency-dependent portions of the sensing and actuation subsystems may be obtained precisely by direct measurement or are known from digital quantities and/or design schematics. As such, these parameters’ measurements will only be briefly discussed.

The detector’s sensing function behaves in a non-linear fashion when uncontrolled, therefore we may only infer the linear model’s scaling coefficient,  $\mathcal{K}_C$ , from measurements of the detectors under closed control loops. We infer that the remaining magnitude ratio between our model and measurements of the open loop transfer function  $G_L(f_{UGF})$  as the sensing coefficient  $\mathcal{K}_C$  (where  $f_{UGF}$  is the unity gain frequency of the DARM control loop). Other

than the known frequency-independent magnitude of  $D(f)$ , the open loop gain model's magnitude is set by the actuation scale factor,  $\mathcal{K}_A$ . This makes it a crucial measurement in our model because it sets the frequency-independent magnitude of the entire response function. Measurements of the open loop transfer function over the entire gravitational wave frequency band are used to confirm that we have modeled the correct frequency dependence of all subsystems. Finally, measurements of  $\gamma(t)$  track the time dependence of the response function. The details of these measurements and respective uncertainty estimates are described below.

### 3.2.1 Actuation Function

The components of each arm's actuation function,  $\mathcal{K}_A^{x,y}$ ,  $DAC(f)$  and  $P^{x,y}(f)$  are measured independently in a given detector. As with  $D(f)$ , both  $\xi^{x,y}$  and  $D_A^{x,y}(f)$  are digital functions included in the model without uncertainty.

#### Actuation Scaling Coefficients, $\mathcal{K}_A^{x,y}$

The standard method for determining the actuation coefficients,  $\mathcal{K}_A^{x,y}$ , used for the fifth science run is an interferometric method known as the “free-swinging Michelson” technique; a culmination of several measurements with the interferometer in non-standard configurations. The method uses the interferometer’s well-known Nd:YAG laser wavelength ( $\lambda = 1064.1 \pm 0.1$  nm, (63; 64)) as the calibrated length reference while using the test mass’ coil actuators to cause a length change. Details of the technique are described in Appendix B. The actuation coefficient is measured using this method many times for each optic in each interferometer over the course of the science run, and their mean used as the actuation scaling coefficient for all model epochs. Table 3.1 summarizes the actuation coefficients,  $\mathcal{K}_A^{x,y}$ , for the three interferometers in the fifth science run, using free-swinging techniques.

Table 3.1: Summary of the actuation scaling coefficients measured during S5. These single numbers are formed by the mean of each measurement’s median  $\langle \mathcal{K}_A^{x,y} \rangle_j$  (6 for each end test mass in H1, 5 in H2, and 14 and 15 for the X and Y test masses, respectively in L1). Only statistical uncertainty is reported here; systematic uncertainty is folded the total uncertainty of the actuation function.

	$\mathcal{K}_A^x$ (nm/ct)	$\mathcal{K}_A^y$ (nm/ct)
H1	$0.847 \pm 0.024$	$0.871 \pm 0.019$
H2	$0.934 \pm 0.022$	$0.958 \pm 0.034$
L1	$0.433 \pm 0.039$	$0.415 \pm 0.034$

#### Force-to-Displacement Transfer Function, $P(f)$

Each test mass coil actuator system is equipped with an optical position sensor system that consists of an infrared LED emitter aimed at a small photodiode mounted in the coil actuator, and a mechanical “flag” attached to the magnet on the optic that cuts through the beam. From amplitude spectral densities of these sensor signals while the optic is free-swinging,

the frequency of each center-of-mass transfer function,  $f_0^{cm}$  is measured with negligible uncertainty. The quality factors,  $Q^{cm}$ , depend on the amount of local damping applied to suspension, but are estimated from driven transfer functions. The uncertainty of this estimation, though large, has little effect on the center-of-mass transfer function in the frequency band of interest and is ignored. Table 3.2 shows the results for the center of mass force-to-displacement transfer function. The drumhead frequency,  $f_0^{dh}$  for each test mass in the Hanford and Livingston detectors have been measured to be 9.20 kHz and 9.26 kHz respectively with  $Q^{dh} \sim 10^5$  (5; 65), where again though the uncertainty in these parameters may be large, it has little effect in band and is ignored.

Table 3.2: Summary of pendulum frequencies,  $f_0^{cm}$ , and quality factors,  $Q^{cm}$ , used to compose models of each interferometer's center-of-mass pendulum transfer functions in S5.

	X End Test Mass	Y End Test Mass		
	$f_0^{cm}$ (Hz)	$Q^{cm}$	$f_0^{cm}$ (Hz)	$Q^{cm}$
H1	0.767	10	0.761	10
H2	0.749	10	0.764	10
L1	0.766	100	0.756	100

### Digital to Analog Conversion, $DAC(f)$

The digital to analog conversion model  $DAC(f)$ , includes the effects of the finite sample-and-hold method used to convert digital signal to an analog voltage, the analog anti-imaging filter, measured residual frequency dependence from imperfect digital compensation of analog de-whitening, and the time delay arising from computation and signal travel time.

We use the standard model for the sample and hold of the digital to analog converter (66; 67)

$$H_s(f) = \text{sinc}\left[(2\pi f)/(2f_s)\right] e^{-i(2\pi f)/(2f_s)}, \quad (3.20)$$

where the sample frequency  $f_s = 16384$  Hz is used in all detectors.

The same analog anti-image filter is used for each of the four coils on the test mass. They are analog, third-order, Chebyshev low-pass filters with 0.5 dB passband ripple whose corner frequency is at 7.5 kHz and 8.1 kHz for the Hanford and Livingston detectors, respectively, and modeled as such in the  $DAC(f)$  transfer function. We also include residuals measured between the modeled anti-imaging filter and its analog counterpart.

For a given end test mass, there is a complementary pair of digital and analog whitening filters for each of the four coil actuators. A comparison between the digital compensation and the real analog electronics has shown non-negligible, frequency-dependent residuals. We measure the residuals for all four coils in each test mass by taking the ratio of transfer functions between a digital excitation and the analog output of the whitening filters with the digital filters on and off. We include the average residual of the four coils in our model.

A detailed analysis of the digital time delay in the digital-to-analog conversion has been performed elsewhere (68). For the actuation model we estimate the time delay from our model of the open loop transfer function (attributing all residual delay in the loop to the actuation function), and assign a fixed delay to each epoch.

### Actuation Uncertainty, $\sigma_A$

The digital suspension filters,  $D_A(f)$ , have well-known digital transfer functions, which are included in the model without an uncertainty. The model of force-to-displacement transfer function,  $P(f)$ , and digital-to-analog conversion,  $DAC(f)$ , are derived from quantities with negligible uncertainty. Hence, the uncertainty estimate for the actuation function is derived entirely from measurements of the actuation scaling coefficient,  $\mathcal{K}_A$ .

The actuation coefficient is measured using a series of complex transfer functions taken to be frequency independent as described in 6. We take advantage of this fact by estimating the frequency-independent uncertainty in the overall actuation function from the statistical uncertainty of all free-swinging Michelson measurements. For magnitude, we include a systematic uncertainty originating from an incomplete model of the actuation frequency-dependence, such that the total actuation uncertainty is

$$\left(\frac{\sigma_{|A|}}{|A|}\right)^2 = \left(\frac{\sigma_{|\mathcal{K}_A|}}{|\mathcal{K}_A|}\right)^2 + \left(\frac{\sigma_{(r/a)}}{(r/a)}\right)^2 \quad (3.21)$$

$$\sigma_{\phi_A}^2 = \sigma_{\phi_{\mathcal{K}_A}}^2. \quad (3.22)$$

The statistical uncertainties,  $\sigma_{|\mathcal{K}_A|}/|\mathcal{K}_A|$  and  $\sigma_{\phi_{\mathcal{K}_A}}$ , are the quadrature sum of the scaling coefficient uncertainty from each test mass, as measured by the free-swinging Michelson technique. For each optic's coefficient, we estimate the uncertainty by taking the larger value of either the standard deviation of all measurement medians, or the mean of all measurement uncertainties divided by the square root of the number of frequency points in a given measurement. These two numbers should be roughly the same if the measured quantity followed a Gaussian distribution around some real mean value and stationary in time. For all optics, in all interferometers, in both magnitude and phase, these two quantities are not similar, implying that the measurements do not arise from a parent Gaussian distribution. We attribute this to the quantity changing over time, or a systematic error in our measurement technique that varies with time. Later studies of the free-swinging Michelson technique have revealed that the probable source of this time variation is our assumption that the optical gain of the simple Michelson remains constant over the measurement suite (see 6).

We have folded in an additional  $\sigma_{(r/a)}/(r/a) = 4\%$  systematic error in magnitude for the Hanford detectors only. This correction results from the following systematic difference between the Hanford and Livingston free-swinging Michelson measurement setup. Analog suspension filters, common to all detectors, are used to increase the dynamic range of the coil actuators during initial control of the test masses. When optic motions are sufficiently small enough to keep the cavity arms on resonance, they are turned off and left off as the detectors approach designed sensitivity (48; 69). These additional suspension filters were left in place for the Hanford measurements in order to obtain better signal-to-noise ratios for the driven transfer functions described in 6. The filters' color had been compensated with digital filters, but the average residual frequency dependence is roughly 4% for both end test masses in H1 and H2.

The total uncertainty for each interferometer's actuation function, as described in Eq. 3.22, is shown in Table 3.3. These estimates include statistical and known systematic uncertainties. To investigate potential unknown systematic uncertainties in the actuation functions we applied two fundamentally different calibration methods. The results of these investigations are described in Appendix B.

Table 3.3: Summary of actuation function uncertainty, in relative magnitude  $\sigma_{|A|}/|A|$  and phase  $\sigma_{\phi_A}$ , used in each interferometer in S5.

	$\sigma_{ A }/ A  [\%]$	$\sigma_{\phi_A} [\text{deg}]$
H1	5.36	1.84
H2	5.84	0.48
L1	12.2	3.07

### 3.2.2 Sensing Function

The components of the sensing function,  $\mathcal{K}_C$ ,  $C_{FP}(f)$ , and  $ADC(f)$  are described in §3.1.1. The frequency-dependent components are developed from measured parameters with negligible uncertainties, and  $K_C$  is obtained as described above. The techniques used to obtain the parameters are described below.

#### Sensing Scaling Coefficient, $\mathcal{K}_C$

In principle, the scaling coefficient  $\mathcal{K}_C$  is also composed of many independently measurable parameters as described in §3.1.1. In practice, these components (specifically components of the optical gain) are difficult to measure independently as the interferometer must be controlled into the linear regime before precise measurements can be made. The scaling coefficient for the other subsystems are either measured (in the actuation) or known (in the digital filters). We take advantage of this by developing the remainder of sensing subsystem (i.e. its frequency-dependence), forming the frequency-dependent loop model scaled by the measured actuation and known digital filter gain, and assume the remaining gain difference between a measurement of open loop transfer function and the model is entirely the sensing scale factor. Results will be discussed in §3.2.3.

#### Fabry-Perot Cavity Response, $C_{FP}(f)$

Our model of the Fabry-Perot Michelson frequency response is the sum of the response from each arm as in Eq. 3.12. Using the single pole approximation (Eq. 3.9), the frequency response of each arm cavity  $H_{SP}^{x,y}(f)$  can be calculated explicitly using a single measured quantity, the cavity pole frequency  $f_c$ . We compute  $f_c$  by measuring the light storage time  $\tau = 1/(4\pi f_c)$  in each cavity.

A single measurement of the storage time is performed by aligning a single arm of the interferometer (as in the right panel of Figure 6.1) and holding the cavity on resonance using the coil actuators. Then, the power transmitted through that arm is recorded as we rapidly take the cavity out of resonance. We fit the resulting time series to a simple exponential decay, whose time constant is the light storage time in the cavity. This measurement is performed several times per arm, and the average light storage time is used to calculate the cavity pole frequency. Table 3.4 shows the values of  $f_c$  used in each model.

Table 3.4: Summary of cavity pole frequencies  $f_c$  used in each interferometer's sensing function in S5. H1 and H2 have used the average of each arm, hence their numbers reported below are the same, with uncertainty estimated as the quadrature sum of each result.

	$f_c^x$ (Hz)	$f_c^y$ (Hz)
H1	$85.6 \pm 1.5$	$85.6 \pm 1.5$
H2	$158.5 \pm 2.0$	$158.5 \pm 2.0$
L1	$85.1 \pm 0.8$	$82.3 \pm 0.5$ Hz

### Analog to Digital Conversion, $ADC(f)$

Each of the four photodiodes used to measure the power at the dark port are sampled at 16384 Hz. The dominant frequency dependence of this analog-to-digital conversion process arises from the analog anti-aliasing filters. These filters are analog eighth order elliptic filters, which differ only in corner frequency at the two sites: 7.5 kHz for the Hanford and 8.1 kHz for Livingston. The frequency dependence is unity below 1 kHz. Above a few kHz, the magnitude changes less than 2%, but the phase loss from these filters becomes non-negligible ( $> 180$  deg). The residual frequency dependence between this model and measured transfer function of the filter is also included. The discrepancy occurs only above 1 kHz and varies less than 2% in magnitude and 5 degrees in phase.

### Time Dependence, $\gamma(t)$

We measure the time dependence of the sensing function by digitally injecting a signal,  $s_{cl}(f)$ , at the output of the digital filters,  $D(f)$ , prior to the control signal,  $s_D(f)$ , at three line frequencies  $f_{cl}$  near 50, 400, and 1100 Hz. The time-dependent coefficient  $\gamma(t)$  is defined as

$$\gamma(t) = \alpha(t)\beta(t) = -\frac{1}{G_L(f_{cl})} \frac{s_D(f_{cl}) - s_{cl}(f_{cl})}{s_D(f_{cl})}, \quad (3.23)$$

where  $G_L(f_{cl})$  is the modeled DARM open loop transfer function at the reference time in each epoch at a given calibration line frequency,  $f_{cl}$ ;  $s_{cl}(f_{cl})$  and  $s_D(f_{cl})$  are the excitation signal and the control signal, respectively, each digitally demodulated at the same frequency and averaged over 60 seconds. The coefficient generated from  $f_{cl} \approx 400$  Hz is used to scale the response function model; the other two frequencies are used to confirm that the variations are independent of frequency. In the ideal case (no noise on top of the injected line and with a perfect model for  $G_L(f_{cl})$ ), the coefficient is a real factor near unity. Figure 3.5 shows the evolution of  $\Re\{\gamma(t)\}$  over the course of the science run for each detector.

We also separate the relative uncertainty of the time dependent coefficient  $(\sigma_\gamma/\gamma)^2$  into those of systematic and statistical origin. As the coefficient is ideally real and unity, we expect the imaginary part of the measurement defined in Eq. (3.23) to be a random time series with zero mean. A non-zero mean would indicate a systematic error in our estimate of  $\Re\{\gamma(t)\}$ , given by  $\sqrt{1 - (\Im m\{\gamma(t)\})^2}$  (assuming the real part of  $\gamma(t)$  is unity). The measured mean is less than 5% for all detectors across the entire run, implying a negligible systematic error of 0.1% and is ignored.

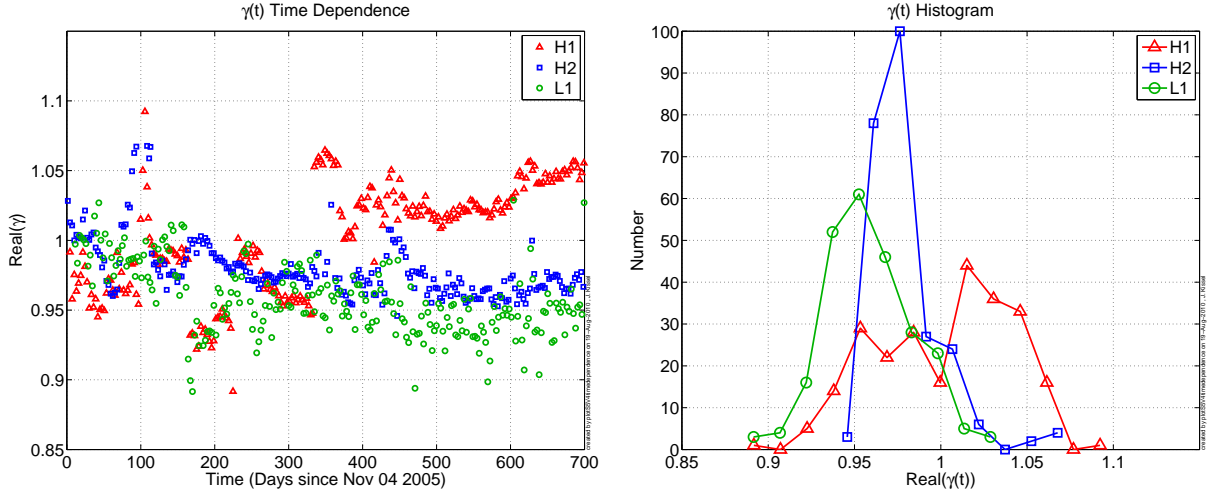


Figure 3.5: Time-dependent corrections to the sensing function  $\text{Re}\{\gamma(t)\}$  over the course of the science run (6). (Left) Time series of  $\text{Re}\{\gamma(t)\}$  for each interferometer. (Right) Histogram of  $\text{Re}\{\gamma(t)\}$  for each interferometer.

The statistical error is determined by the signal-to-noise ratio of the calibration line at frequency  $f_{cl}$ , and is estimated by the standard deviation of  $\Im m\{\gamma(t)\}$ , measured in every epoch at a sampling rate of 1 Hz. Though the statistical error is roughly equivalent in all epochs for a given detector, we chose the largest standard deviation as a representative error for the entire run. Figure 3.6 shows an example histogram of  $\Im m\{\gamma(t)\}$  for H2.

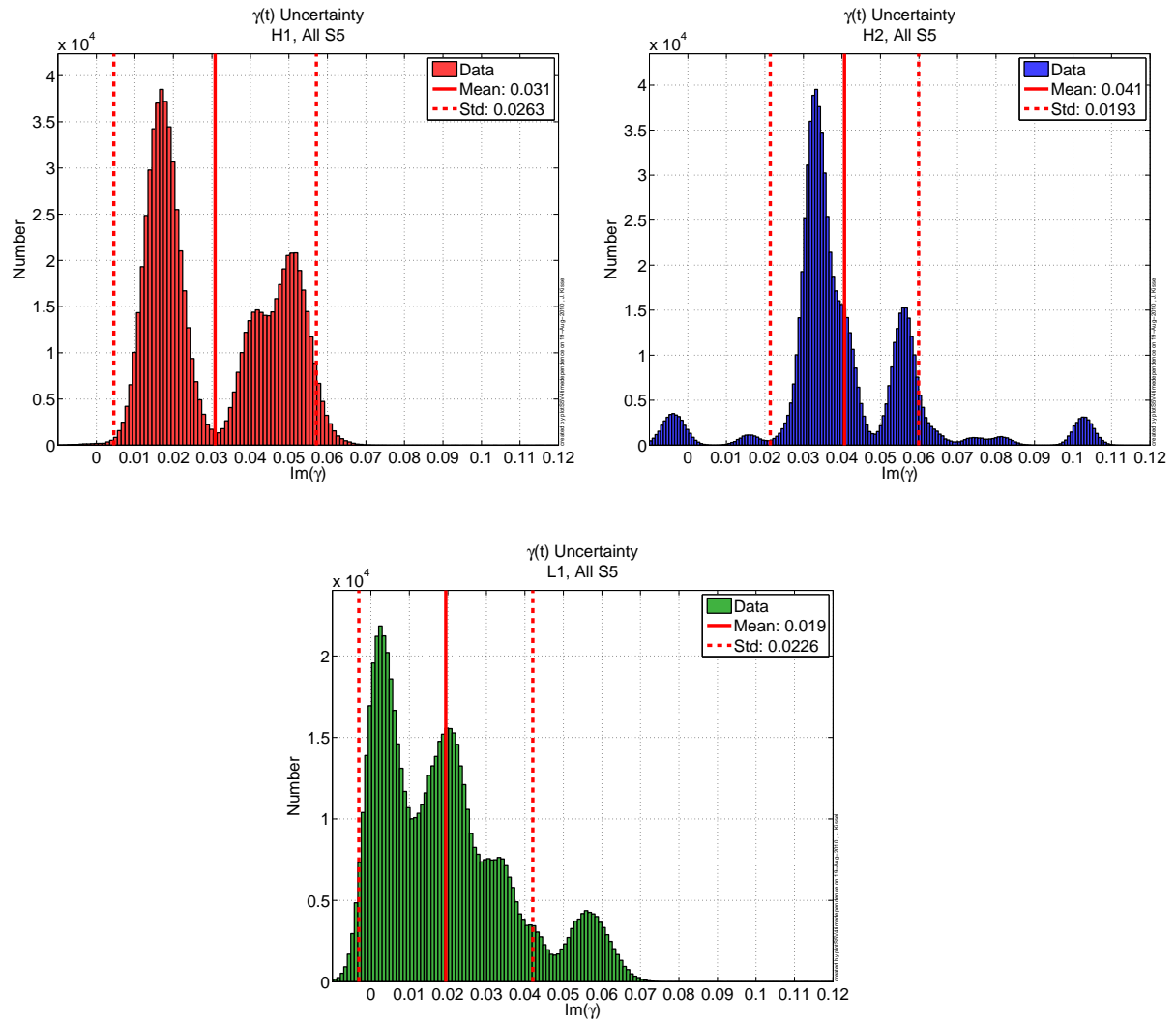


Figure 3.6: Histograms of  $\Im\{m\{\gamma(t)\}\}$  over the entire S5 run, for H1 (top left), H2 (top right), and L1 (bottom). The standard deviation the data set represents a systematic uncertainty estimation of  $\sigma_\gamma$ . The standard deviation  $\Im\{m\{\gamma(t)\}\}$  for all interferometers is less than 5%, implying a negligible systematic uncertainty.

### 3.2.3 Open Loop Transfer Function

The open loop transfer function,  $G_L(f)$ , is measured while the interferometer is controlled, operating in the nominal configuration, at designed sensitivity. We use a digital DARM excitation with amplitude much larger than  $\Delta L_{ext}$ , such that we may assume it to be a contribution to measurement noise. During the measurement we assume no time-dependent variations occur, and set  $\gamma(t) = 1$ . We compare this measurement against our model of the open loop transfer function which is the product of each subsystem described above (see Eq. 3.4), and scale the model by the measurement's magnitude at the expected unity gain frequency to form  $\mathcal{K}_C$  as described in §3.2.2. Values for the sensing scaling coefficient averaged over epochs, are shown in Table 3.5.

Table 3.5: Average value for scaling coefficients  $\mathcal{K}_C$  for the sensing function,  $C_L(f,t)$  for each interferometer. They are stated without uncertainty, since these quantities are derived from measurements of the open loop gain and actuation scaling coefficient. See further discussion in §3.3.

	$\mathcal{K}_C$ ( $cts/10^{-15}m$ )
H1	0.15
H2	0.61
L1	9.1

We measure the open loop transfer function many times during the course of the science run. To compare these measurements against the model for each epoch, they are normalized by the magnitude of the open loop transfer function at a fixed unity gain frequency. This normalization removes the time dependent scale factors between measurement times such that a fair comparison can be made. Figure 3.7 shows the results of this comparison.

The uncertainty estimation in the open loop transfer function magnitude and phase ( $(\sigma_{|G_L|}/|G_L|)^2$  and  $\sigma_{\phi_{G_L}}^2$ ) are separated into systematic and statistical uncertainty. We expect the ratio of the model and our measurements to follow a Gaussian distribution with unity mean in magnitude and zero mean in phase. This ratio is shown in Figure 3.7. We observe a non-Gaussian systematic in all detectors from an unknown source, most apparent in the Hanford detectors. We estimate this systematic uncertainty in magnitude and phase by subtracting a smoothed version of the residuals,  $G_L^{res}(f) = \langle G_L^{model}/G_L^{meas} \rangle$ , from unity and zero, respectively. The statistical uncertainty,  $\sigma_{\Sigma|G_L|}$  and  $\sigma_{\Sigma\phi_{G_L}}$ , is estimated from the standard deviation of the remaining scatter in the ratio after the systematic error  $G_L^{res}(f)$  is subtracted. Both the systematic and statistical errors are added in quadrature to form the total uncertainty in the open loop transfer function model,

$$\left( \frac{\sigma_{|G_L|}}{|G_L|} \right)^2 = (\sigma_{\Sigma|G_L|})^2 + (1 - |G_L^{res}(f)|)^2 \quad (3.24)$$

$$\sigma_{\phi_{G_L}}^2 = \left( \sigma_{\Sigma\phi_{G_L}} \right)^2 + \left( \phi_{G_L^{res}(f)} \right)^2. \quad (3.25)$$

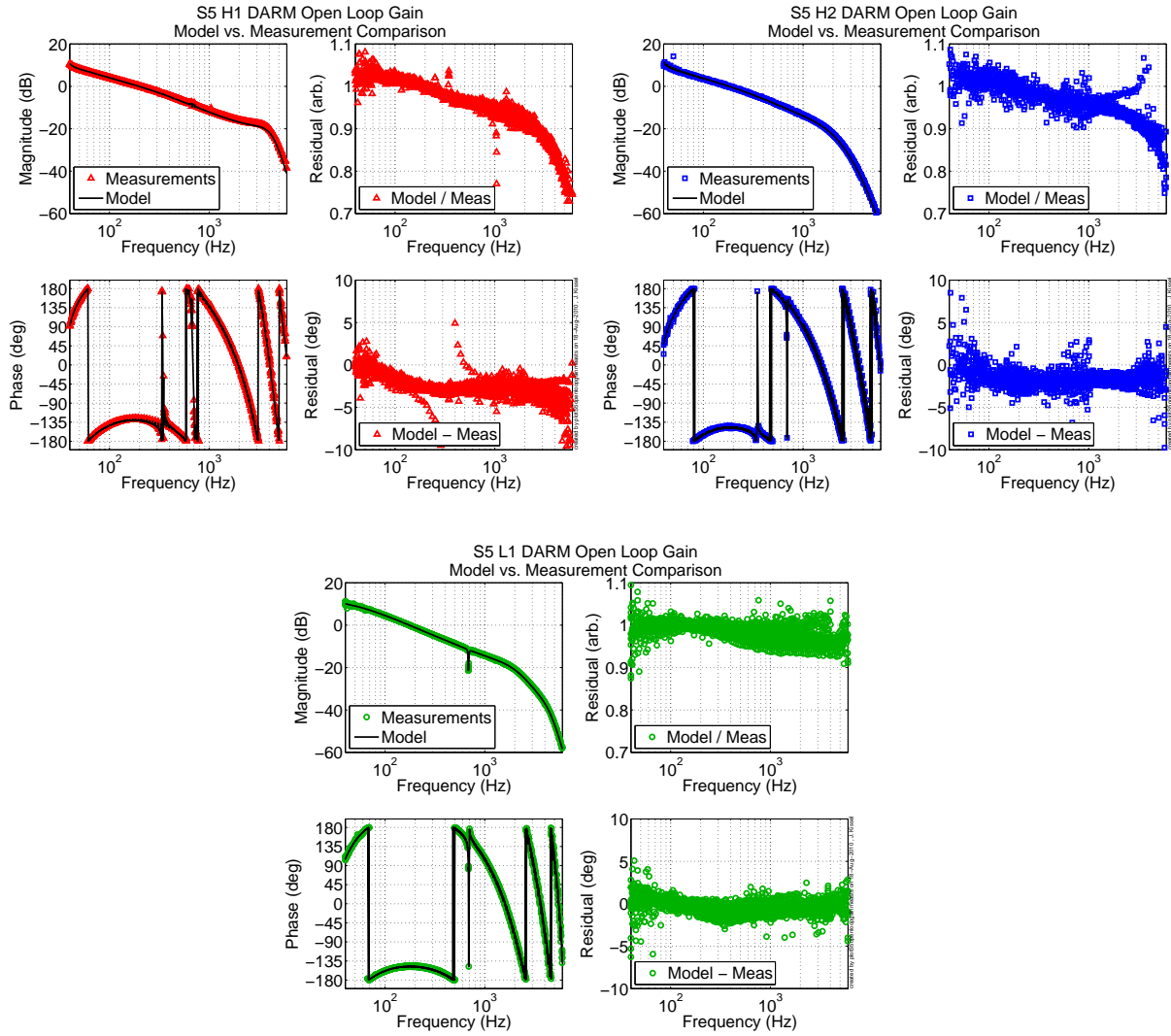


Figure 3.7: Open loop transfer function model vs. measurement comparisons for H1 (top left), H2 (top right), and L1 (bottom) in all of S5. The four panels shown are the magnitude and phase of model and measurements (top and bottom left), and the ratio between model and measurements (top and bottom right).

### 3.3 Uncertainty Estimation

The measurement uncertainty of each component of the response function described in §3.2 are folded into a complex function of frequency known as the “error budget.” Formulation of the error budget is of particular importance to data analysis, as the total uncertainty of the response function determines that accuracy to which we may compare a given interferometer’s output with another, and it also constrains the reconstruction of a possible gravitational wave form. The latter constraint determines the accuracy to which the analysis may determine the parameters of the astrophysical source.

We do not assign any uncertainty to the digital filters  $D(f)$  nor directly to the time-independent component of the sensing function  $C_L(f)$ . The digital filters, which are well-known digital functions, are placed into the model without uncertainty. As described in §3.2.2, the frequency dependence of the sensing function is composed of parameters measured to negligible uncertainty. Uncertainties in its scaling coefficient  $\mathcal{K}_C$ , are accounted for in the open loop transfer function and actuation function uncertainty.

The uncertainties of the remaining quantities in the response function  $A(f)$ ,  $G_L(f)$ , and  $\gamma(t)$  are treated as uncorrelated. If the uncertainties are completely correlated (i.e. there are none in  $C_L(f)$ ), the covariant terms in the estimation reduce the overall estimate of the response function uncertainty (see Appendix C). Since we do not have an independent estimate of the uncertainty in the sensing function, we adopt this conservative estimate.

We re-write the response function in terms of the measured quantities to which we assign uncertainty,

$$R_L(f, t) = A(f)D(f) \frac{1 + \gamma(t)G_L(f)}{\gamma(t)G_L(f)} \quad (3.26)$$

and separate into magnitude and phase (dropping terms which include the uncertainty in  $D(f)$ ),

$$|R_L| = \sqrt{\left(\frac{|A|}{\gamma|G_L|}\right)^2 \left[1 + (\gamma|G_L|)^2 + 2\gamma|G_L|\cos(\phi_{G_L})\right]}, \quad (3.27)$$

$$\phi_{R_L} = \arctan\left(\frac{\gamma|G_L|\sin(\phi_A) + \sin(\phi_A - \phi_{G_L})}{\gamma|G_L|\cos(\phi_A) + \cos(\phi_A - \phi_{G_L})}\right), \quad (3.28)$$

such that the relative uncertainty in magnitude and absolute uncertainty in phase are

$$\begin{aligned} \left(\frac{\sigma_{|R_L|}}{|R_L|}\right)^2 &= \left(\frac{\sigma_{|A|}}{|A|}\right)^2 + \Re e\{W\}^2 \left(\frac{\sigma_{|G_L|}}{|G_L|}\right)^2 \\ &\quad + \Im m\{W\}^2 \sigma_{\phi_{G_L}}^2 + \Re e\{W\}^2 \left(\frac{\sigma_\gamma}{\gamma}\right)^2 \end{aligned} \quad (3.29)$$

$$\begin{aligned} \sigma_{\phi_{R_L}}^2 &= \sigma_{\phi_A}^2 + \Im m\{W\}^2 \left(\frac{\sigma_{|G_L|}}{|G_L|}\right)^2 \\ &\quad + \Re e\{W\}^2 \sigma_{\phi_{G_L}}^2 + \Im m\{W\}^2 \left(\frac{\sigma_\gamma}{\gamma}\right)^2, \end{aligned} \quad (3.30)$$

where we define  $W \equiv 1/(1 + G_L)$  (see Appendix C for derivation). Each uncertainty component in Eqs. 3.29 and 3.30 is assumed to be the same over the course of the science run (independent of epochs). However, the complex coefficient  $W$  is different for each epoch.

Our calculation of the response function includes the open loop transfer function model which is approximated by replacing the complete cavity response  $H_{FP}(f)$  (Eq. 3.8) with the single pole transfer function  $H_{SP}(f)$  (Eq. 3.9) in the sensing function subsystem. We include the ratio of the response function calculated with and without the correct cavity response in our error budget,

$$\frac{R_L^{FP}(f)}{R_L^{SP}(f)} = \frac{1 + (H_{FP}/H_{SP})G_L(f)}{1 + G_L(f)} \quad (3.31)$$

added linearly (as opposed to in quadrature) because the approximation results in a frequency-dependent scaling of the response function with known sign. As with the weighting function  $W$ , this term involves the direct multiplication of the open loop transfer function and therefore is epoch dependent. As an example, Figure 3.8 shows this error contribution from the third epoch in each detector.

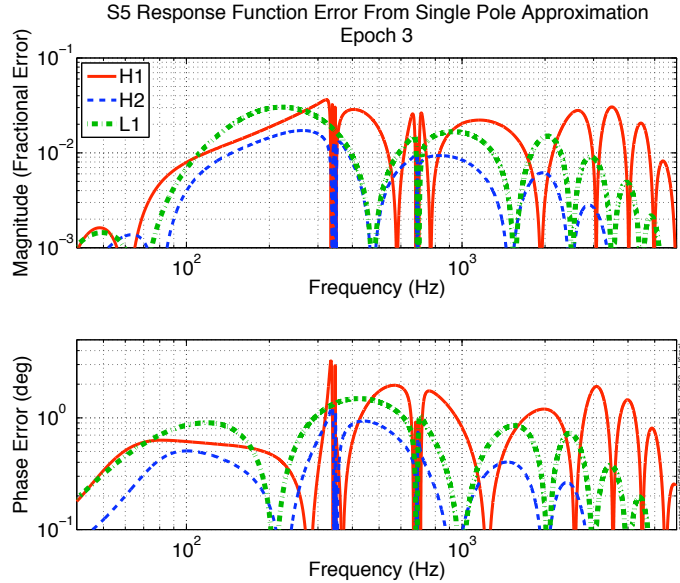


Figure 3.8: Systematic uncertainty in response function arising from the single pole approximation of the Fabry-Perot cavity response in open loop transfer function. This uncertainty is epoch-dependent; only the third epoch for each detector is shown.

## 3.4 Results

In Figure 3.9 we plot the final response function for all interferometers for the entire fifth science run. Figure 3.10 shows the frequency dependence of all terms in the error budget of the response function for the third epoch of each detector. In Table 3.6, we summarize the

frequency-dependent uncertainty of each interferometer’s response function by dividing the error into three frequency bands: 40-2000 Hz, 2000-4000 Hz and 4000-6000 Hz and computing the RMS errors across each band, averaged over all epochs. All epoch uncertainties are within 1% of the mean uncertainty stated. Each value is the estimated 68% (one sigma) confidence interval across the band for the entire 2 calendar-year science run.

Table 3.6: Summary of band-limited response function errors for the S5 science run.

	$R_L(f)$ Magnitude Error (%)			$R_L(f)$ Phase Error (Deg)		
	40-2000 Hz	2-4 kHz	4-6 kHz	40-2000 Hz	2-4 kHz	4-6 kHz
H1	10.4	15.4	24.2	4.5	4.9	5.8
H2	10.1	11.2	16.3	3.0	1.8	2.0
L1	14.4	13.9	13.8	4.2	3.6	3.3

The largest source of systematic error in most data analysis techniques used to analyze S5 LIGO data is the uncertainty in response function magnitude (24; 70; 23). Our inability to measure the sensing function independently of the closed loop (specifically its scaling coefficient) forces a conservative, uncorrelated treatment of the uncertainty in the measured subsystems,  $A(f)$  and  $G_L(f)$ , inflating the total uncertainty in the response function. In all detectors, we find the uncertainty in the actuation function,  $A(f)$ , dominates the response function error budget in magnitude.

The statistical uncertainty in the free-swinging Michelson measurements of the actuation scaling coefficient are the primary source of the actuation uncertainty. In the Hanford detectors, the uncertainty arises from our inability to displace the test mass above residual external noise sources at high frequency. This decreases the signal-to-noise of the measurement, inflating the uncertainty estimate across the measurement band. For L1, in which we have obtained a large number of measurements using several methods of the free-swinging Michelson technique (see 6), we have found the results to be inconsistent with a Gaussian distribution. We attribute this to a poorly understood underlying variation in the technique, for example the assumption that the optical gain is time-independent over the course of the measurement suite.

The assumption that the actuation scaling coefficient is linear in amplitude over the range of actuation, from the  $10^{-8}$  m employed for the free-swinging Michelson technique to the  $10^{-18}$  m required to compensate for expected gravitational wave signals, has not been confirmed. To investigate the linearity of the actuation scaling coefficients over this range of actuation amplitudes, and to bound potential overall systematic errors, we have employed two additional, fundamentally different, actuator calibration methods. The so-called “frequency modulation” technique (71) uses an independently calibrated oscillator to frequency-modulate the interferometer’s laser light, creating an effective length modulation on the order of  $10^{-13}$  m while operating in a single-arm interferometer configuration. The so-called “photon calibrator” technique (72) uses auxiliary, power-modulated lasers to displace the test masses by approximately  $10^{-18}$  m via radiation pressure with the interferometer in its nominal configuration (see Figure 1). Both methods are employed at select frequencies across the LIGO measurement band. Statistical uncertainties for both methods are reduced to the 1% level by averaging many measurements.

At the end of the S5 science run, a detailed comparison between these two methods and

the free-swinging Michelson technique was performed. With all three calibration methods, actuation coefficients were measured over the frequency band from 90 Hz to 1 kHz for each end test mass. For the H1 and H2 interferometers, all calculated actuation coefficients—for all frequencies, for all four masses, and for all three methods—were within a  $\pm 15\%$  range. The maximum difference between the mean value for any method and the mean value for all three methods, for any of the four end test masses, was 3.7% (73). This indicates that the overall systematic uncertainties in the actuation functions determined using the free-swinging Michelson method, and therefore the magnitudes of the interferometer response functions, are within these bounds.

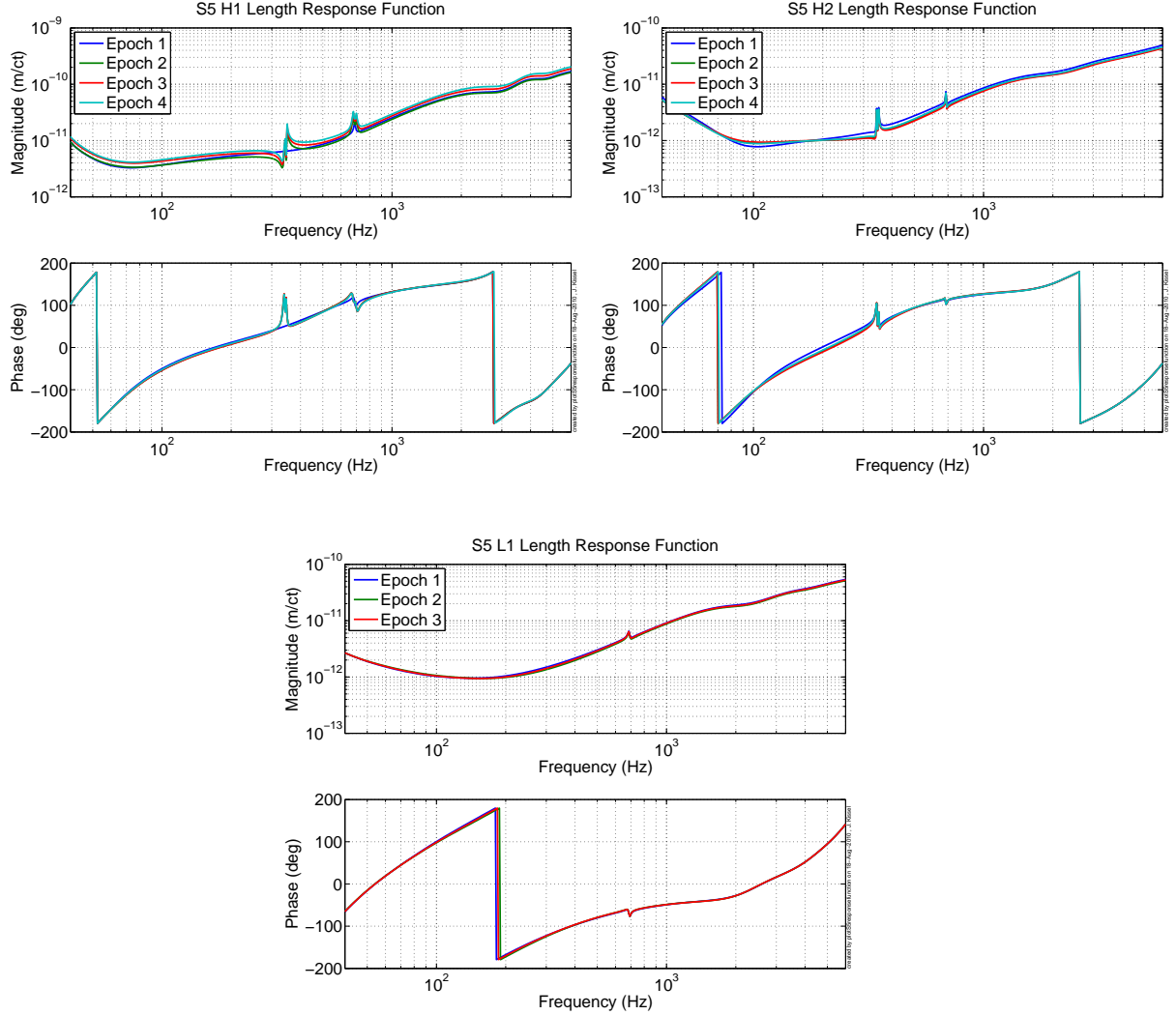


Figure 3.9: Frequency dependent response function,  $R_L(f)$ , for the three LIGO interferometers for all epochs of the S5 science run.

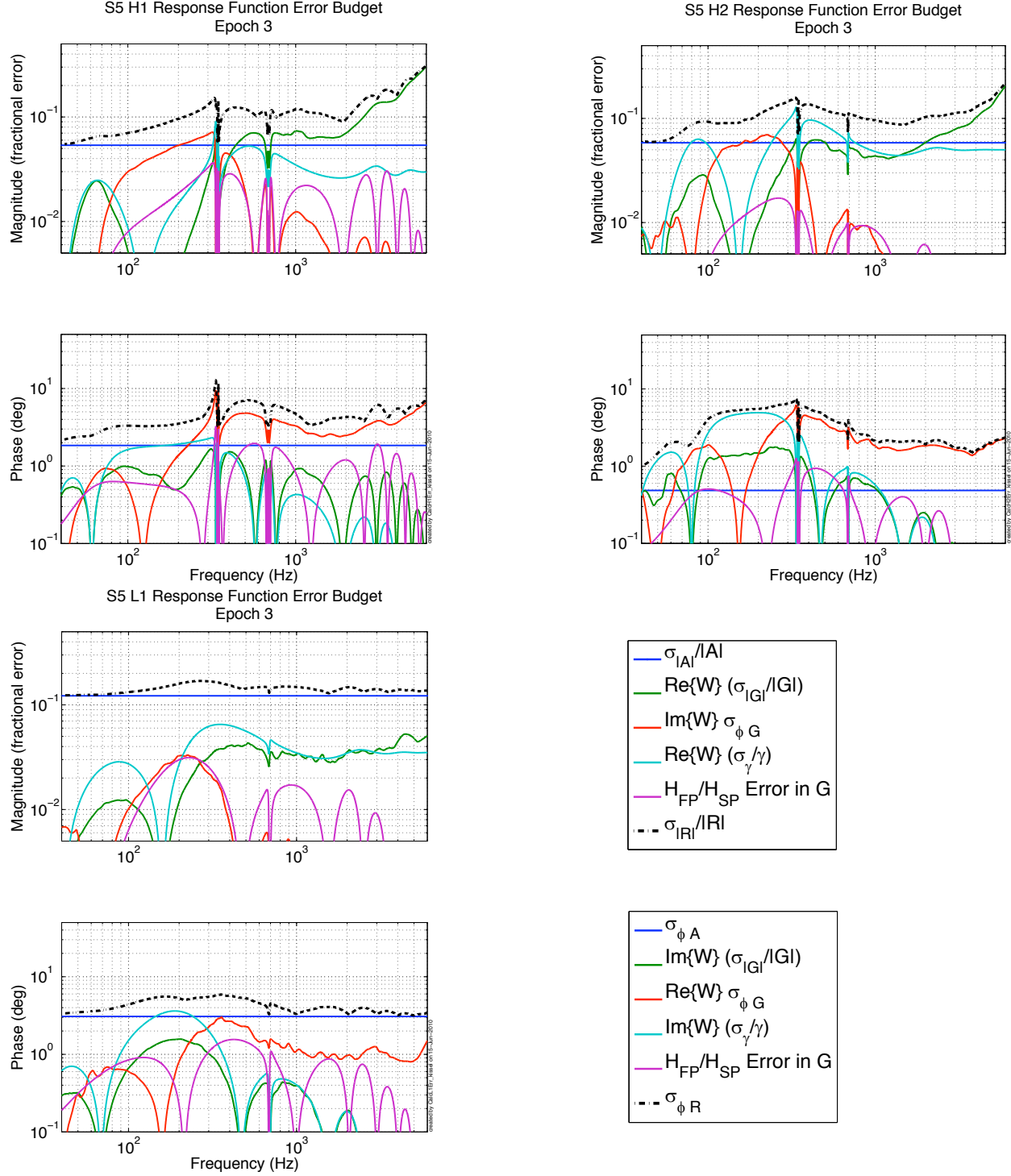


Figure 3.10: Frequency dependent error estimates for the response function for H1 (top left), H2 (top right), and L1 (bottom left). In magnitude (top panel) and phase (bottom panel), the total uncertainty (dashed-black) is composed of the uncertainty in actuation,  $\sigma_{|A|}/|A|$ ,  $\sigma_{\phi A}$  (in blue), the open loop transfer function magnitude  $\sigma_{|G|}/|G|$  (in green), the open loop transfer function phase,  $\sigma_{\phi G}$  (in red), the time-dependent factor,  $\sigma_{\gamma}/\gamma$  (in cyan), and from the single pole approximation of the Fabry-Perot cavity response (in magenta).

### 3.5 Summary

The LIGO interferometers have provided some of the world’s most sensitive gravitational wave strain measurements during their fifth science run. We have described a model used for each interferometer’s differential arm length control loop known as the length response function,  $R_L(f, t)$ , the proportionality between the digital Pound-Drever-Hall error signal,  $e_D(f)$  and differential displacement of the arm cavity lengths. Measurements presented here have shown the frequency-dependent uncertainty in  $R_L(f, t)$  is less than 15% in magnitude and 5° in phase for the frequency band where the interferometer is most sensitive. The results of two fundamentally different, high-precision methods for measuring the actuation functions (71; 72) confirm that these results are free of systematic uncertainty within the stated uncertainties (73).

In the two calendar year science run, as knowledge of the long-term characteristics of the instrument increased, a great deal of improvements were made to the calibration measurement techniques compared with prior results (74). By analyzing the uncertainties of each measured component of the response function independently, we have identified the actuation function as the dominant source of uncertainty in our model of the response function. In turn, estimates of the actuation function uncertainty are limited by our inability to displace the test masses above residual ground motion during measurements.

In the era of the next generation of detectors, data analysis will require an amplitude uncertainty of 10% or less to reduce the calibration uncertainty below other systematic errors of the continually improving astrophysical searches (75). The improved accuracy will increase our confidence of a detection as possible candidates are compared across the network of interferometers. Once regular detections are made, it will improve the ability to reconstruct the original waveform of the incident gravitational wave, allowing for parameters of the astrophysical source to be better resolved. Chapter 4 introduces the advanced detectors, which are predicted to achieve regular detections by broadening the LIGO sensitivity to lower frequencies and decreasing the noise floor by a factor of 10 or more.

# 4. The Advanced Laser Interferometer Gravitational Wave Observatory

## 4.1 The Second Generation of Fabry-Perot Michelson Interferometers

The first generation of LIGO detectors, henceforth referred to as “Initial LIGO,” were built with design parameters near the limit of technology for the time (circa 1990’s). However, they were built in an infrastructure designed to hold much more powerful instruments in the future (1). With two decades of further research and development such a detector is now possible that may improve strain sensitivity as much as a factor of 10 in the 100-200 Hz region, the most sensitive region of the instruments. Indeed, great efforts have been made on all fundamental noise source fronts, over a broad range of frequencies, to design and build instruments that will improve sensitivity at every frequency between 10 Hz and 10 kHz. All research, development, and design has been finished on these new detectors, and are currently being built. Installed in the same vacuum system as the current detectors, they will entirely replace the Initial LIGO internal components, the first installation of which will begin in the Fall of 2010. All three interferometers are expected to be operational by 2014, with their designed sensitivity achieved some time later. Figure 4.1 shows a model of the target sensitivity for all interferometers in Advanced LIGO with the limiting fundamental noise sources compared against the best sensitivity obtained by the Livingston interferometer during the S5 science run. The expected detection rate for the well-modelled compact binary coalescence sources of the Initial LIGO detectors is at most  $0.6 \text{ yr}^{-1}$  for neutron star binaries (although more likely  $0.02 \text{ yr}^{-1}$ ). When the Advanced LIGO detectors achieve their designed sensitivity, these rates are expected to increase to as many as  $40 \text{ yr}^{-1}$  (36).

This chapter discusses the Advanced LIGO interferometers, including general improvements to the Initial LIGO design with specific attention devoted to the improved seismic isolation and suspension systems. As a part of this system, the single-stage active isolation platform is introduced by defining the goals for its performance such that it is not a limiting noise source to advanced LIGO sensitivity.

## 4.2 Upgrades to the Initial LIGO Interferometers

Advanced LIGO was designed to be a quantum noise limited interferometer at frequencies greater than 10 Hz, while improving the broad-band sensitivity by a factors of 10 or more from the Initial LIGO sensitivity. This implies that the sensitivity be limited by shot noise at high frequency and radiation pressure noise at low frequency. In order to achieve this, three fundamental changes will be made to the Initial LIGO interferometer: several optical layout changes and increased laser power will reduce the quantum noise at high frequencies; dissipation of the test masses and suspension systems will be reduced to lower the thermal noise at intermediate frequencies; and significant improvements in the seismic isolation and suspension systems will be made in order to increase detection band at low frequency.

The quantum noise will be reduced using three different methods. First, the power of the laser injected into the interferometer will be significantly increased from roughly 5 W to

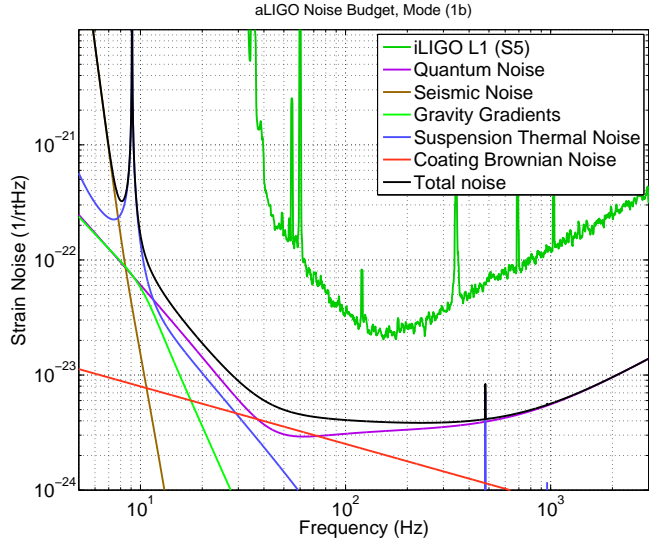


Figure 4.1: Comparison between the best initial LIGO strain sensitivity (L1, Aug 2007) and predicted baseline sensitivity for advanced LIGO.

125 W, as shot noise in any Michelson-based interferometer scales proportionally to  $\sqrt{P_{BS}}$ . The increase in input power will be done using a three stage laser system. The first stage is a Nd<sup>3+</sup>:Yag non-planar ring oscillator (NPRO) that generates a  $\lambda = 1064$  nm, 2 W beam as in Initial LIGO. The second stage is an amplifier which boosts the optical power to 35 W and acts as the master laser to the third stage; an injection locked ring oscillator that increases the optical power to 180 W (76). However, expected losses in the input optic chain reduce this power to 125W incident on the power-recycling cavity. In order to combat the radiation pressure back-reaction noise associated with higher input power, the mass of the test masses has been increased from 10 kg to 40 kg.

Second, the readout of differential arm lengths will be more efficient. The geometry of the recycling cavity and arm cavities will be converted from roughly flat-flat cavities to roughly confocal cavities. In the case of the power-recycling cavity, this will provide an increase in stability, and make the cavities much less susceptible to thermal and angular fluctuations, as well as provide adaptable mode matching which may compensate for mirror imperfections. The addition of a signal-recycling cavity, in conjunction with increasing the arm cavity finesse increased from 220 to 450, will yield the ability to tailor the interferometer's response function to a particular frequency range, and reduce the need for greater input power (77). This tailoring is performed by changing the microscopic length of the signal recycling cavity, effectively detuning the cavity from resonance by a phase  $\phi_{SRM} = 2\pi\ell_S/\lambda$ .

Third, the detection scheme for sensing the differential arm lengths will be switched from a heterodyne, PDH radio-frequency modulation scheme to a homodyne, “DC” scheme. This will further reduce shot noise and reduce sensitivity to technical noises such as laser frequency and amplitude noise. This requires the addition of an output mode cleaner before the detection photodiodes, which strips the light exiting the signal-recycling cavity of all injected sideband fields ( $f \simeq 1 - 100$  MHz), and any non-fundamental modes produced from imperfections in, thermal distortions of, or alignment fluctuations in the interferometer optics. The mode cleaner therefore leaves only the carrier field and gravitational wave side-

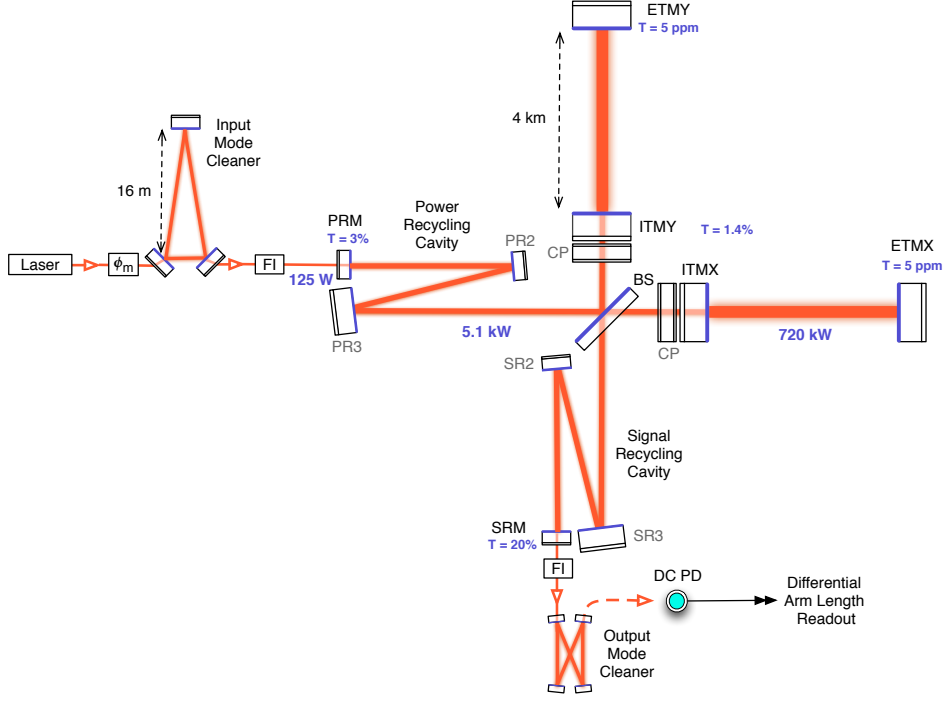


Figure 4.2: Optical layout for Advanced LIGO. Changes from the Initial LIGO layout (Figure 2.2) include, increasing the input mode cleaner length, splitting the power recycling into a stable, three-mirror cavity, and the addition of a stable signal recycling cavity and output mode cleaner at the antisymmetric port.

bands ( $f \simeq 1 \text{ Hz} - 10 \text{ kHz}$ ). The reduction of unnecessary light on the readout photodiodes improves the signal-to-noise ratio (61; 78), and therefore improves the sensitivity. Further, because only light filtered by the 4 km arm cavities is used, the contribution of laser noise is reduced above the cavity pole frequency,  $f_c$ , of the arm cavities (79).

Many complementary methods will be employed to reduce the second fundamental noise source between 50 and 500 Hz: thermal fluctuations in the test masses and suspension systems. Modest improvements have been made to the optical coating materials: doping the high index layers of tantalum  $Ta_2O_5$  with 25% titania  $TiO_2$  has shown to reduce the effective loss  $\phi_{eff}$  by roughly a factor of 2 (80). Also, as has been shown in Eq. 2.9, the noise scales inversely proportional to the beam size. The larger test masses allow for increase in beam size to be used in the arm cavities. The increase from a 25 cm to 35 cm in diameter, garners an immediate order of magnitude improvement in the coating thermal noise. As will be discussed later, the Advanced LIGO suspensions have been designed using materials with significantly lower loss by replacing the final stage of the suspension system with monolithic fused-silica fibers. These fibers, with the help of the monolithic construction will greatly reduce the dissipation (loss angle  $\phi$ ) in the system, such that this noise source will be below expected radiation pressure noise.

Finally, the seismic “wall” we moved to reduce the lower limit of the detection band from 40 Hz to 10 Hz. This will be accomplished by completely replacing the Initial LIGO in-vacuum passive isolation platforms and single suspensions with active isolation platforms and

many, multi-layered suspension systems. These improvements will be discussed in Section 4.3.

For both practical and astrophysical motivations, the ability to change the input power and tune signal-recycling cavity allows the Advanced LIGO interferometers to operate in several “modes.” The expected sensitivity of the most probable modes of operation are shown in Figure 4.3. The first mode, (1a) will have input power of 25 W incident on the power-recycling cavity, and maintain full resonance in the signal recycling cavity ( $\phi_{SRM} = 0$ ). The low input power reduces the radiation pressure back-reaction noise, therefore increasing sensitivity at low frequencies. This low-frequency sensitivity favors expected upper limits of known continuous wave sources (81), and the detection of large-SNR black-hole black-hole binary systems (27). The additional practical benefit is to use only the first two stages of the advanced LIGO laser system, which have been previously demonstrated with the upgraded initial LIGO interferometers. The second mode, (1b) engages the final ring-oscillator stage of the laser, increasing the power to the maximum designed output, with 125 W incident on the power-recycling cavity. This mode serves as a “catch-all:” moderately sensitive to a wide variety of sources, and is therefore the baseline mode for Advanced LIGO to maximize the probability of gravitational wave detection. The third possible mode, (2) serves to optimize the sensitivity at high frequency by using the full power of the advanced LIGO laser (125 W), and detuning the signal recycling cavity by  $\phi_{SRM} = 20^\circ$ . The latter is more difficult from a control perspective, but low-mass compact binary coalescences (i.e. neutron-star neutron-star pairs), and burst sources including the core-collapse of massive stars during supernova are expected to dominate the sources in this frequency band, and these sources are likely to have corresponding electromagnetic signatures that improve detection confidence.

### 4.3 Advanced LIGO Seismic Isolation

A great deal of improvements must be made to the seismic isolation systems in order to reduce the influence of ground motion from 40 Hz to 10 Hz. Improvements in this band greatly increase the detection event rate, as gravitational waves from massive astrophysical systems are dominant in this frequency band (36).

All chambers in all three interferometers will be outfit with hydraulic external pre-isolation (HEPI). The pre-isolation system is an active isolation system that quiet hydraulic actuators to provide relatively large-throw ( $\pm 1$  mm in translation,  $\pm 1$  mrad in rotation), six degree of freedom static positioning for the isolation systems inside the vacuum chambers. In addition, signals from position and inertial sensors colocated with the actuators are blended, conditioned, and fed back to the actuators. The blended signal provides position control down to DC, while providing isolation from ground in the 0.1 - 10 Hz band. This system serves as the first line of defense against large seismic disturbances from human activity, earth tides, ocean waves, and seasonal changes in the local environment. This system was installed in 2004 for L1, where these seismic disturbances prevented daily operation of the interferometer. This installation has demonstrated that a factor of ten in the 0.1-10 Hz band can be achieved for all three translational degrees of freedom (82).

Inside the vacuum system, the test masses in the Fabry-Perot arm cavities require the most amount of isolation to achieve Advanced LIGO’s sensitivity goals. As such, they receive the most extensive isolation systems in the interferometer. The in-vacuum, initial LIGO 4 stage passive isolation stacks will be replaced by a two-stage active and passive isolation system known as the BSC in-vacuum seismic isolation platform, or BSC ISI (83). Each cascading stage is connected with steel blade-spring and wire flexure systems which provide compliance in all six cartesian degrees of freedom, with rigid body resonances are in the band

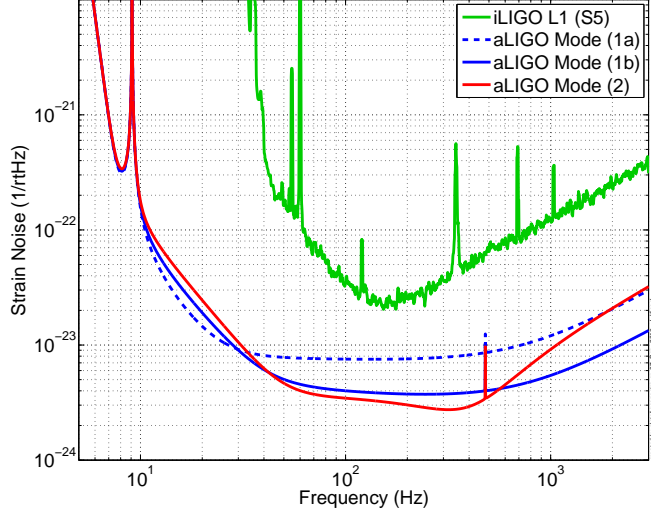


Figure 4.3: Proposed Advanced LIGO sensitivity. Three different “modes” are proposed, indicative of possible configurations for the interferometer. Mode (1a) and (1b) are operated at low and high input power ( $P_{IN}^{(1a)} \simeq 25W$ ,  $P_{IN}^{(1b)} \simeq 125W$ ), with the signal recycling cavity at optimal tuning ( $\phi_{SRM} = 0^\circ$ ). Mode 2 is tuned for maximum range out to which we may see binary neutron star coalescence (optimally oriented, SNR 8), with high input power ( $P_{IN} \simeq 125W$ ) and a detuned signal recycling cavity,  $\phi_{SRC} = 20^\circ$ .

between 2 and 10 Hz. These short pendulum systems provide classic  $f^{-4}$  isolation from the external stage above these resonances. However, each stage also contains electromagnetic coil actuators used to control the motion of the stage, and an array of position and inertial sensors to sense motion. The active feedback system improves the passive isolation in a frequency band between 0.1 and 20 Hz. A prototype of this isolation system has been shown to achieve a factor of 300 at 1 Hz and a factor of over 3000 (84).

The bottom of second stage of the BSC ISI is an optical table, from which Advanced LIGO test mass suspensions are mounted. These suspensions systems are a cascading series of four pendulums, of which the test masses are the final stage (83; 76; 77). With each stage having similar resonant frequencies in the 0.5 – 5 Hz band, they provide a reduction from residual motion of the BSC-ISI proportional to  $f^{-8}$ . While the first three stages of the pendula, suspending the “top mass,” “upper intermediate mass,” and “penultimate mass” will be suspended via steel wire and blade-springs like the BSC-ISI, the penultimate mass and test mass will both be 40 kg fused silica bulk mass, connected by fused silica fibers, creating a monolithic, ultra-high Q (low loss) structure. In addition, each layer of the quadruple suspension will be using by an adjacent quadruple pendulum from which forces will be applied that originate from an equally isolated source. The first three stages will contain electromagnetic coil drivers similar to initial LIGO design, but the test mass will be controlled using electro-static drive, to further reduce the amount of control-induced noise. Figure 4.4 shows a SolidWorks rendering of the entire in-vacuum isolation system inside a

BSC chamber, and Figure 4.5 shows the quadruple suspension in detail, including the final monolithic stage.

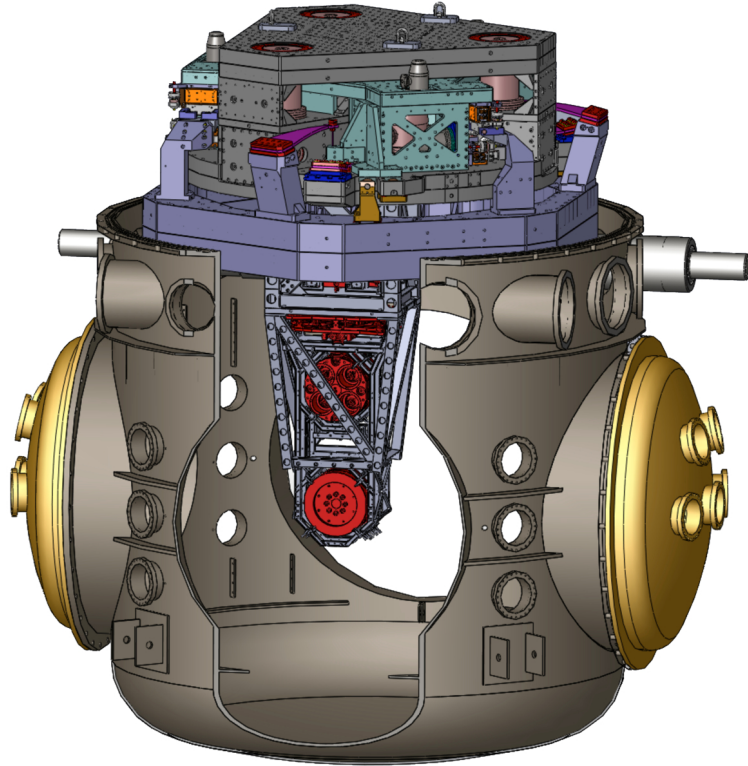


Figure 4.4: SolidWorks rendering of the in-vacuum components of the seismic isolation and suspension system for the test masses (7).

The remaining optics will receive varying degrees of less seismic isolation, according to their impact on the interferometer sensitivity. Figure 4.6 shows the Advanced LIGO optical layout, indicating which the suspension types for each optic. The beam splitter, supported by an BSC-ISI, will be suspended from a triple suspension. The power- and signal-recycling cavity optics, inside HAM vacuum chambers, will be suspended from two types of triple pendula depending on the size of the optic, referred to as the HAM Large Triple Suspension (HLTS) or HAM Small Triple Suspension (HSTS). These suspensions are shown in Figure 4.7. Finally, the output mode cleaner and the output Faraday isolator will be suspended from a double and single suspension system, respectively.

All auxiliary optics, in HAM chambers will be mounted on a simpler version of the BSC-ISI, called the HAM in-vacuum seismic isolation platform or HAM-ISI. In the remainder of this chapter, the isolation requirements for the HAM-ISI are derived with respect to the coupling between displacement of the recycling cavity lengths and the gravitational readout for Advanced LIGO.

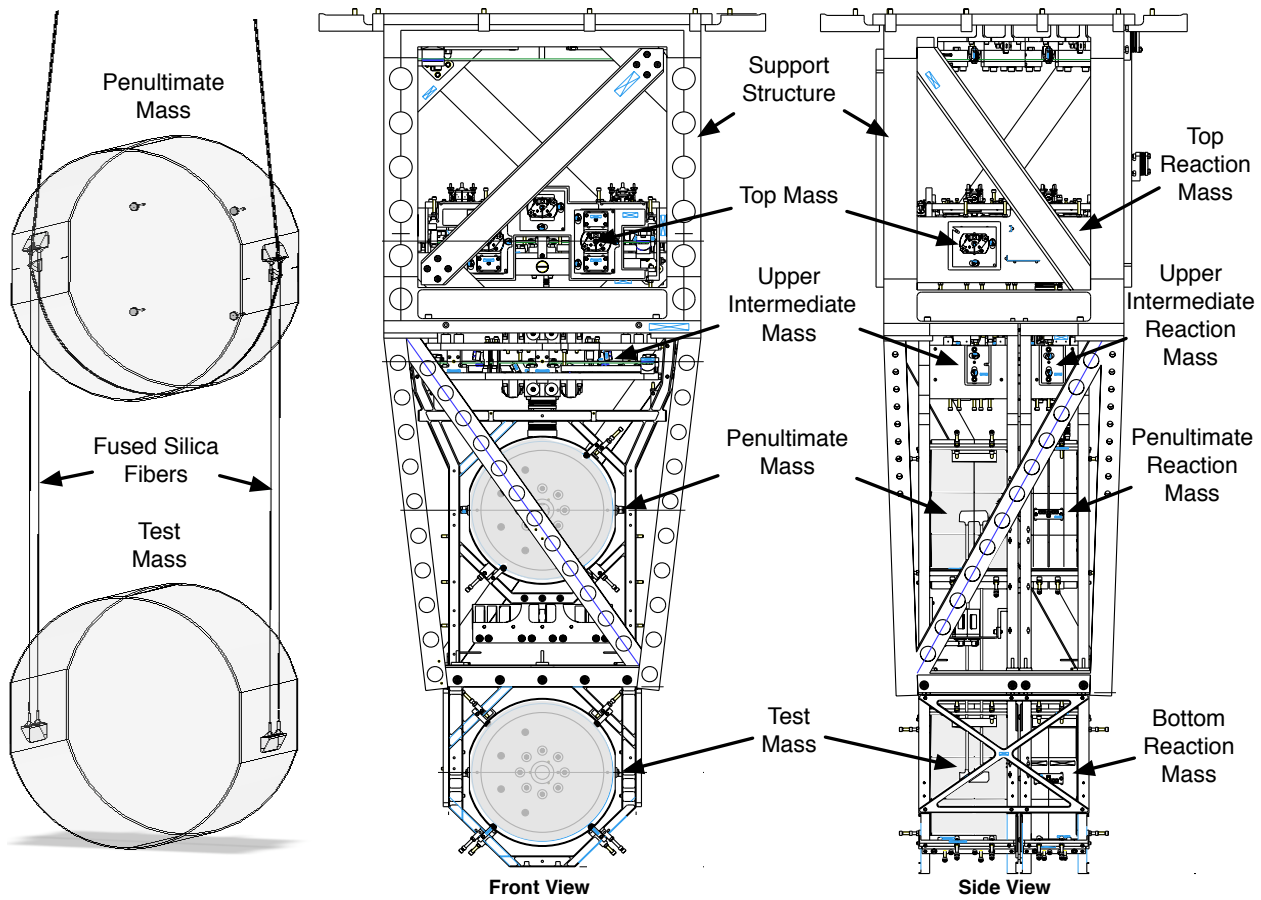


Figure 4.5: Advanced LIGO quadruple suspension (8; 9). (Left) SolidWorks rendering of the final two stages of the suspension, composed entirely of monolithic fused silica. The connecting fibers are welded to the sides of the penultimate and test masses at junctions known as “ears.” These two stages are suspended from the upper stages with steel wire. (Middle, Right) Front and side view, mechanical drawing of the entire suspension assembly.

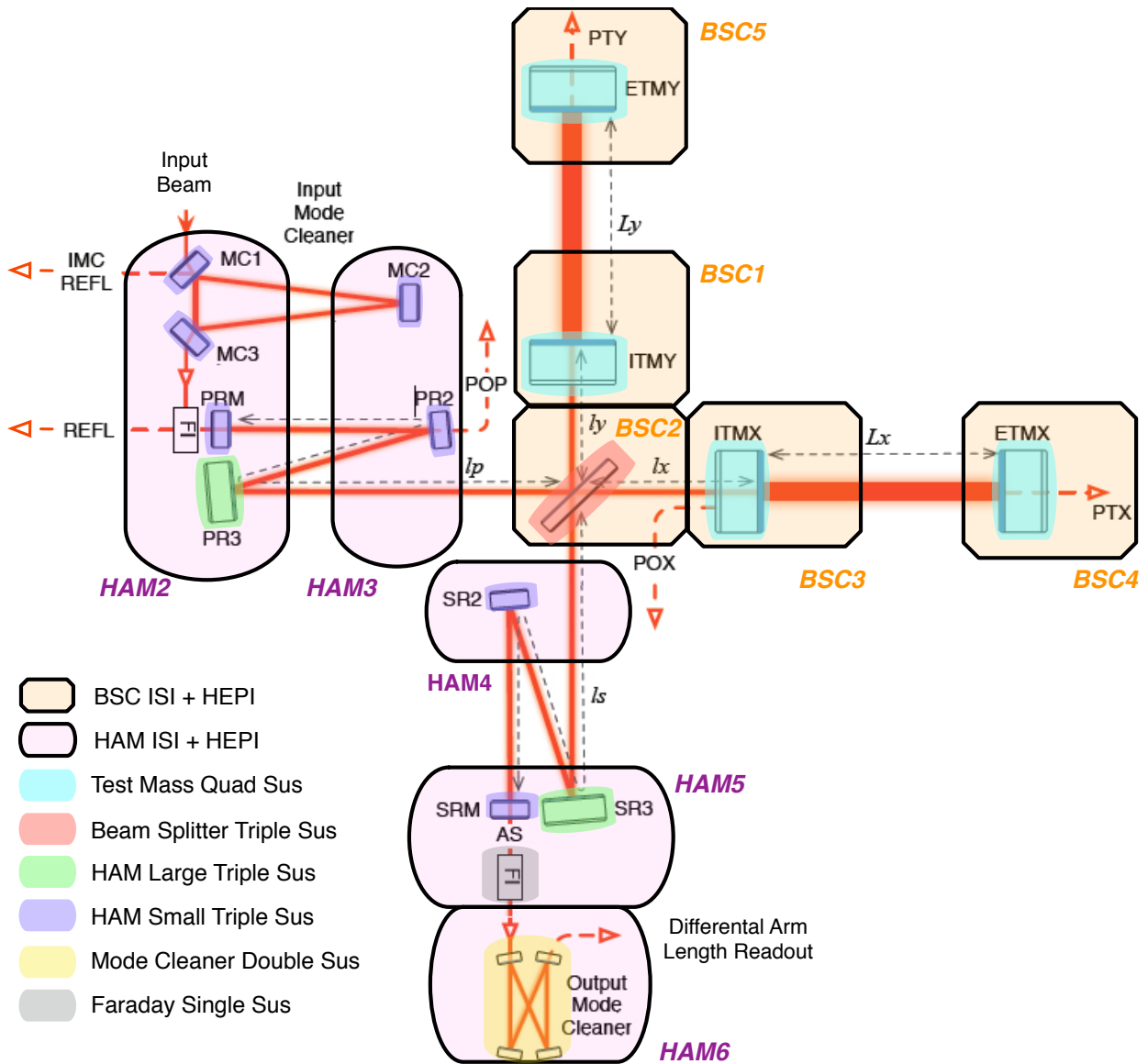


Figure 4.6: Advanced LIGO seismic isolation suspensions and active isolation. Each vacuum chamber shown is equipped with a single layer of hydraulic external pre-isolation or (HEPI). The test masses and beam splitter are in BSC-style chambers (orange) supported by a double-stage in-vacuum isolation platform (BSC-ISI), while HAM-style chambers (purple) which house the input and output optics are supported by a single-stage, in-vacuum seismic isolation platform (HAM-ISI). The test masses are each supported by a quadruple pendulum (cyan). The beam splitter (red), the third power and signal power recycling cavity optics (green), and the remaining recycling cavity optics (dark purple) have a triple pendulum suspensions. The output mode cleaner (yellow) is housed in a double suspension, and the output Faraday isolator in a single suspension.

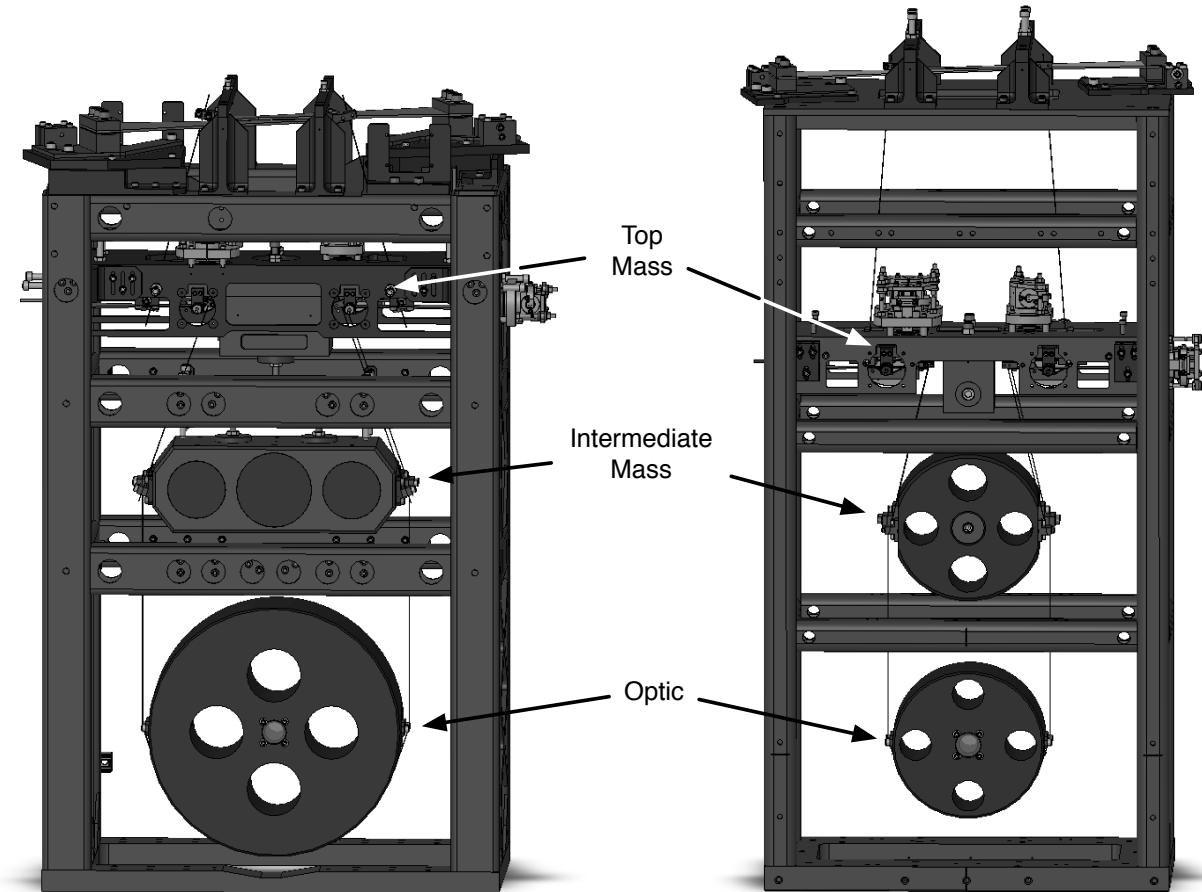


Figure 4.7: SolidWorks rendering of Advanced LIGO HAM triple suspensions (10; 11). (Left) HAM large triple suspension, which will support the large recycling cavity optics (PR3 and SR3). (Right) HAM small triple suspension, which will support the small recycling cavity mirrors (PR2, PRM, SR2, and SRM). The top and intermediate mass are suspended with blade springs in addition to wires to improve vertical isolation. The optics in this rendering have been replaced with dummy masses or blanks, as is typical for the design stages when the exact properties of the optics are not known.

## 4.4 Goals for Single Stage Seismic Isolation

Both power and signal cavities are composed of three optics, the largest suspended from a single HAM Large Triple Suspension and two from HAM Small Triple Suspensions (Figure 4.6). In this section, we describe the target performance for the single-stage, active, in-vacuum, seismic isolation platforms on which the suspensions are mounted, known as a “HAM-ISI.”

Requirements for displacements in both the power- and signal- recycling cavity lengths (PRCL and SRCL, respectively) are the same below 5 Hz, and are defined based on the long-term knowledge of the ground spectra and previous experience with interferometric control of auxiliary degrees of freedom (14; 85). They are the same for all degrees of freedom, longitudinal (horizontally, along the beam line), transverse (horizontally, perpendicular to the beam line), and vertical (10; 11). Therefore, the requirements for all degrees of freedom (X, Y, Z, RX, RY, and RZ) for the HAM-ISIs are also the same below 5 Hz. From 5 Hz down to 0.6 Hz, the lowest eigenmodes of the triple suspensions, the requirements are set to minimize the RMS motion of the cavities, such that optically controlled length and alignment control loops need not have  $> 5$  Hz bandwidth. Any greater a bandwidth would cause the sensing noise of these loops to limit the 10-20 Hz band of the interferometer sensitivity (86). At frequencies between 0.1 – 0.2 Hz, the requirements are set to be roughly a factor of 5 - 10 below the RMS motion of the ground at these frequencies. Below 0.1 Hz they must not to amplify the ground motion. These requirements (below 0.2 Hz) are the same requirements of the test mass isolation platforms (BSC ISIs), as differential motion between the core optics and the recycling cavities would result undesired low-to-high frequency mixing of optical fields or “up-conversion” effects.

The coupling mechanism between changes in the recycling cavity lengths and the differential arm length readout is different for the two cavities, but the suspension systems are the same. As such, the requirements for the HAM-ISI deviate above 5 Hz based on their differences.

The coupling between fluctuations of the SRCL to the differential arm length readout is a function of frequency,

$$\frac{x_{DARM}}{x_{SRCL}} = 0.012 \left( \frac{10 \text{ Hz}}{f} \right)^2 \left( \frac{P_{arm}}{750 \text{ kW}} \right)^2 \left( \frac{0.014}{T_{ITM}} \right) \left( \frac{\delta L}{10 \text{ pm}} \right) \quad (4.1)$$

where  $P_{arm}$ , is power in the arm cavities,  $T_{ITM}$  is transmission of input test masses, and  $\delta L$  is the fixed offset between the arm cavity lengths used for homodyne readout (87). The displacement noise for the triple suspensions is expected to be dominated by the suspension thermal noise, proportional to  $f^{-5/2}$  at frequencies above the natural resonant frequencies (32). The total contribution to the DARM displacement noise is therefore proportional to  $f^{-9/2}$ . Taking the power dependence of the coupling and the design of the triple suspension into account, whose highest longitudinal resonant frequency is  $\simeq 3$  Hz, the coupling is expected to contribute the most to DARM in the 10-30 Hz band (11; 10). The requirements for displacement noise of the SRCL are therefore defined to be 10 times below the predicted spectra of the high power, tuned interferometer configuration (mode 1b in Figure 4.3) at 20 Hz, and have frequency dependence proportional to  $f^{-5/2}$  between 30 Hz and below. Above 30 Hz, where the contribution is expected to continue to fall with frequency, the requirements are relaxed to have the same magnitude as the requirements at 30 Hz and independent of frequency (87). This requirement is shown in Figure 4.8.

The requirements for the seismic isolation systems under the SRCL cavity above 5 Hz are therefore defined such that the SRCL motion, as a result of transmittance of the triple

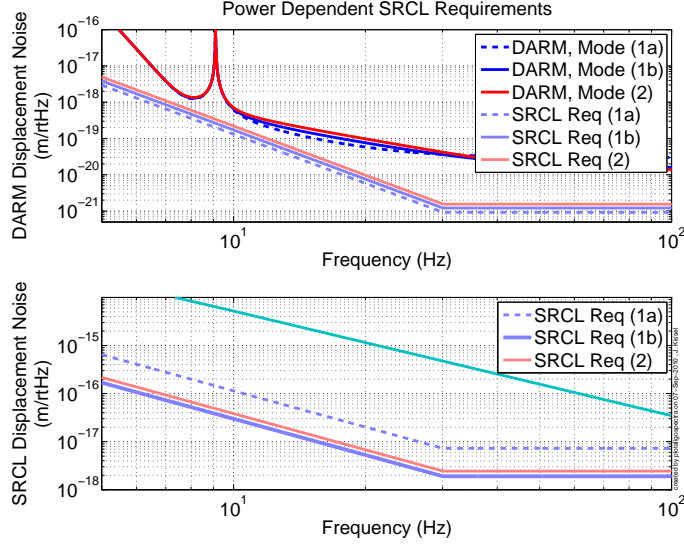


Figure 4.8: Power dependent requirements for the advanced LIGO signal recycling cavity. In terms of signal recycling cavity length, mode 1b is the most stringent, and is therefore chosen as the limiting target for the SRCL.

suspensions, does not exceed this thermal noise limit (10; 11; 88). The SRCL displacement  $d\ell_S$  is modelled to be a combination of the longitudinal and vertical input motion from the isolation systems,  $dx_\ell$  and  $dx_Z$ , transmitted through the triple suspensions of the optics that compose the cavity, ( $T_\ell^L$ ,  $T_Z^L$  for SR3 and  $T_\ell^S$ ,  $T_Z^S$  for SR2 and SRM), or

$$\begin{aligned} d\ell_S = & dx_\ell^{HAM4} (2T_\ell^S) - dx_\ell^{HAM5} (2T_\ell^L + T_\ell^S) \\ & + \frac{dx_\ell}{dx_Z} [dx_Z^{HAM4} (2T_Z^S) - dx_Z^{HAM5} (2T_Z^L + T_Z^S)] \end{aligned} \quad (4.2)$$

where vertical-to-horizontal coupling is considered using the factor  $dx_\ell/dx_Z$ , such that we may explicitly consider the requirements for the residual vertical and horizontal motion of the isolation platform. The power spectral density is therefore estimated to be

$$\begin{aligned} d\ell_{SRCL}^2 = & (dx_\ell^{HAM4})^2 |2T_\ell^S|^2 + (dx_\ell^{HAM5})^2 |2T_\ell^L + T_\ell^S|^2 \\ & + \left( \frac{dx_\ell}{dx_Z} \right)^2 \left[ (dx_Z^{HAM4})^2 |2T_Z^S|^2 - (dx_Z^{HAM4})^2 |2T_Z^L + T_Z^S|^2 \right]. \end{aligned} \quad (4.3)$$

Note that the input motion of SRM and SR3 are treated coherently, as they will reside on the same platform. To develop the requirements of the HAM-ISIs, we treat the displacement of each chamber  $dx_{\ell,Z}^{HAM4,5}$  to be the same, the transmissions of the triple suspensions is as defined in (11; 10) (shown in Figure 4.9), and the vertical to horizontal coupling factor set to  $10^{-3}$ .

The coupling between the displacements of the PRCL and the gravitational wave readout is not expected to dominate the DARM displacement noise. The original requirements

were determined from the tolerable fluctuations in the mode cleaner length and assumed to be sufficient for the PRCL displacement noise (85). These requirements also serve as a requirement for the rotational degrees of freedom for all HAM-ISIs, assuming radians instead of meters.

Figure 4.10 summarizes the displacement noise requirements for each degree of freedom for the HAM-ISIs under the power and signal recycling cavities, in addition to showing an example amplitude spectral density of ground motion from which the platforms must isolate the suspensions.

Between 2007 and 2008, the H1 and L1 Initial LIGO interferometers received several upgrades that included Advanced LIGO technology prototypes. This intermediary interferometer is referred to as “Enhanced LIGO.” Included in these upgrades were prototype HAM-ISIs, whose preliminary Advanced LIGO design had been completed. At the time, only the requirements for the power-recycling cavity HAM-ISIs were defined, and thus served as the target for these prototypes. Chapter 5 describes the prototype seismic isolation system in great detail, including the mechanical design, modelled performance, and results from two prototypes recently built for L1 and H1 interferometers.

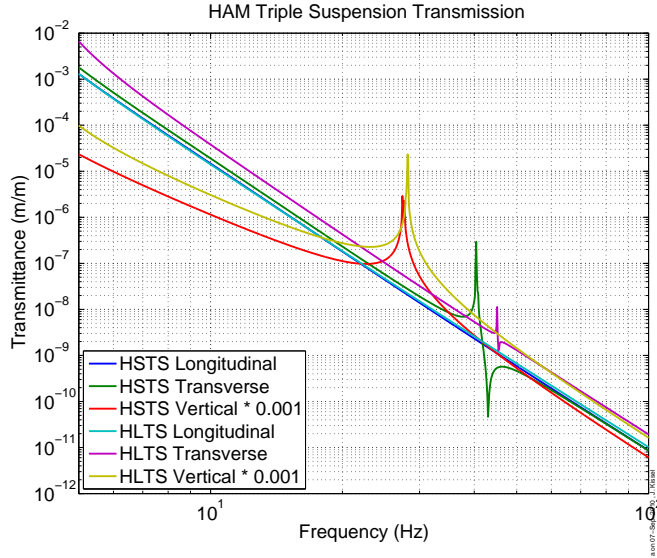


Figure 4.9: Model transmission of the HAM Large Triple and HAM Small triple suspensions for advanced LIGO (12; 13). For each suspension, the transmittance is defined by the input motion, at the suspension point of the first suspended stage, to the final optic motion at the bottom of the third suspension stage. In practice we treat the input motion at the suspension point to be that of the entire support structure which is mounted to the single stage isolation platform.

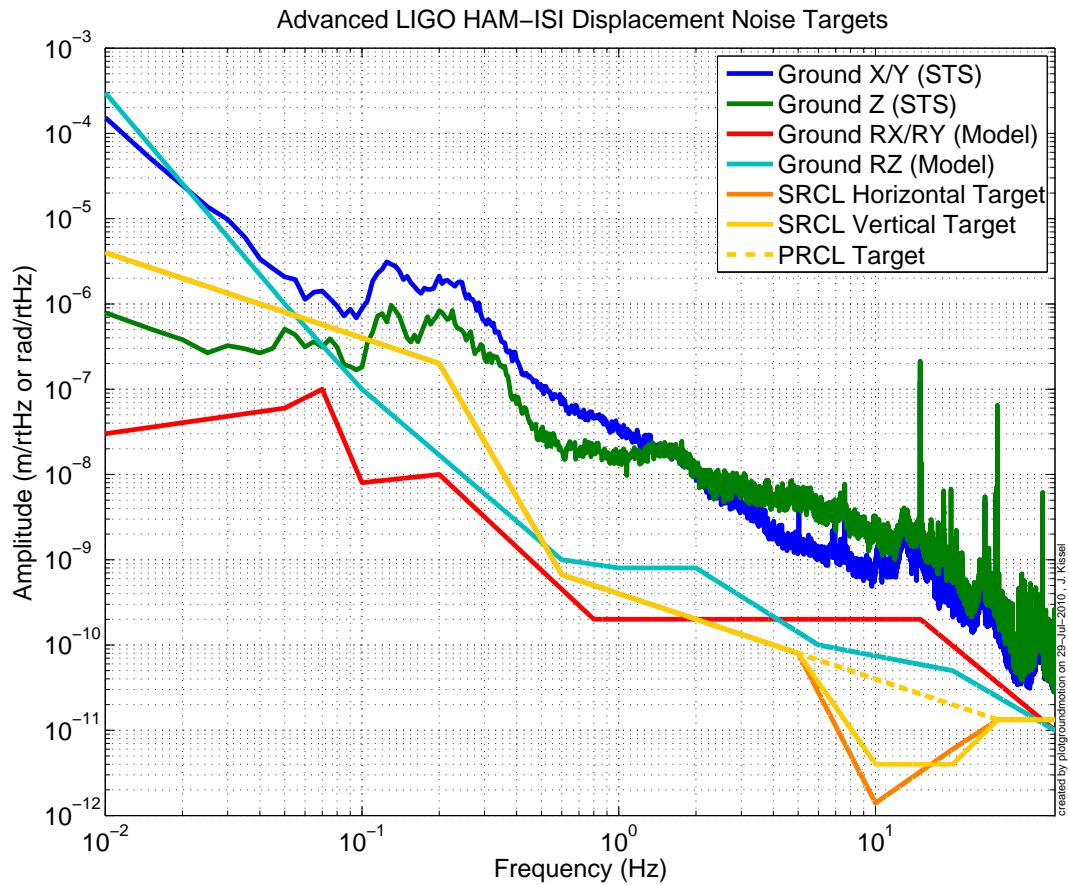


Figure 4.10: Advanced LIGO Target HAM ISI platform displacement noise (13; 12). The PRCL length requirements serve as rotation requirements in  $\text{rad}/\sqrt{\text{Hz}}$  for both recycling cavity lengths. Estimates of the ground motion were measured modeled from the Livingston observatory, assumed to be average representative spectra the site (the Hanford observatory has roughly equivalent ground motion, (14)). Translational degrees of freedom (X, Y, Z) are measured by an STS-2 seismometer on the ground near the HAM6 chamber. Rotational degrees of freedom (RX, RY, RZ) are estimates from a combination of ground STS-2 data interpreted as tilt ( $> 0.3 \text{ Hz}$ ), and differential signal between L4-C seismometers mounted on the four corners of the HAM support structure.

# 5. Prototype HAM-ISI Seismic Isolation System

In preparation for Advanced LIGO, two prototype HAM ISIs were built and installed in H1 and L1 for Enhanced LIGO in 2008. These prototypes were served to demonstrate that the single-stage isolation system can meet Advanced LIGO requirements for the HAM chambers under the power recycling cavity in all six degrees of freedom. This chapter describes the design, model, commissioning and results from these prototypes, in addition to the modifications to their design such that they meet Advanced LIGO requirements for all chambers.

## 5.1 Mechanical Architecture and Design

The HAM ISI was designed by High Precision Devices (HPD, (89)), in collaboration with Brian Lantz and Corwin Hardham using decades of experience with previous active seismic isolation platforms developed for Advanced LIGO (90; 91). The single-stage, HAM ISI consists of two major components, the support stage and suspended stage. An exploded SolidWorks rendering of the HAM ISI is shown in Figure 5.1. The support stage provides a thick, rigid, platform which rests across the support tubes of the HAM chamber against which actuation forces may be applied. The suspended stage is a hexagonal structure upon which all suspensions and auxiliary optics will be mounted. The hexagonal structure is a natural extension of the triangular symmetry of all components of the platform. Passive isolation from the support stage to the suspended stage is achieved from three blade spring and flexure systems between the support and suspended stages. Active isolation and alignment is achieved with an array of inertial sensors and displacement sensors internal the suspended stage, whose signal is fed back to electromagnetic actuators. Further isolation is achieved by correcting the displacement sensor signal with an inertial sensor on the ground.

Given the triangular symmetry of the table, we use two coordinate systems when describing the HAM ISI, defined in Figure 5.2. The colocated basis groups sensors and actuators in the same corners of the suspended stage together. For example, in location 1 in Figure 5.2, there exists a horizontal and vertical actuator, a horizontal and vertical inertial sensor, and a horizontal and vertical displacement sensor. The clusters are labeled H1 and V1 respectively, for a total of six degrees of freedom. The coordinate basis is aligned the interferometer's global coordinate system obeying the canonical Cartesian axes X, Y and Z. Rotational degrees of freedom are denoted by the rotation about those axes, RX, RY and RZ.

The mechanical architecture for the HAM ISI is designed to be stiff, relatively light, and such that it is easy to actively control. The triangular arrangement of the blade spring flexure system allows for motion in all six cartesian degrees of freedom with little cross-coupling. The blade springs are soft in the Z direction, and the flexures are soft in X and Y. The physical properties of the flexures and springs are designed so that the resonant frequencies in the coordinate basis were all between 0.5 and 2 Hz. Almost all of the major components of the system are made from piece-wise bolted light-weight Aluminum 6061, giving the suspended stage a high stiffness-to-weight ratio. Further, the suspended stage has many stiffening ribs, replicating the performance of a solid structure. The lowest non-translational resonances of the suspended stage are above 200 Hz. The range of motion provided by the blade spring

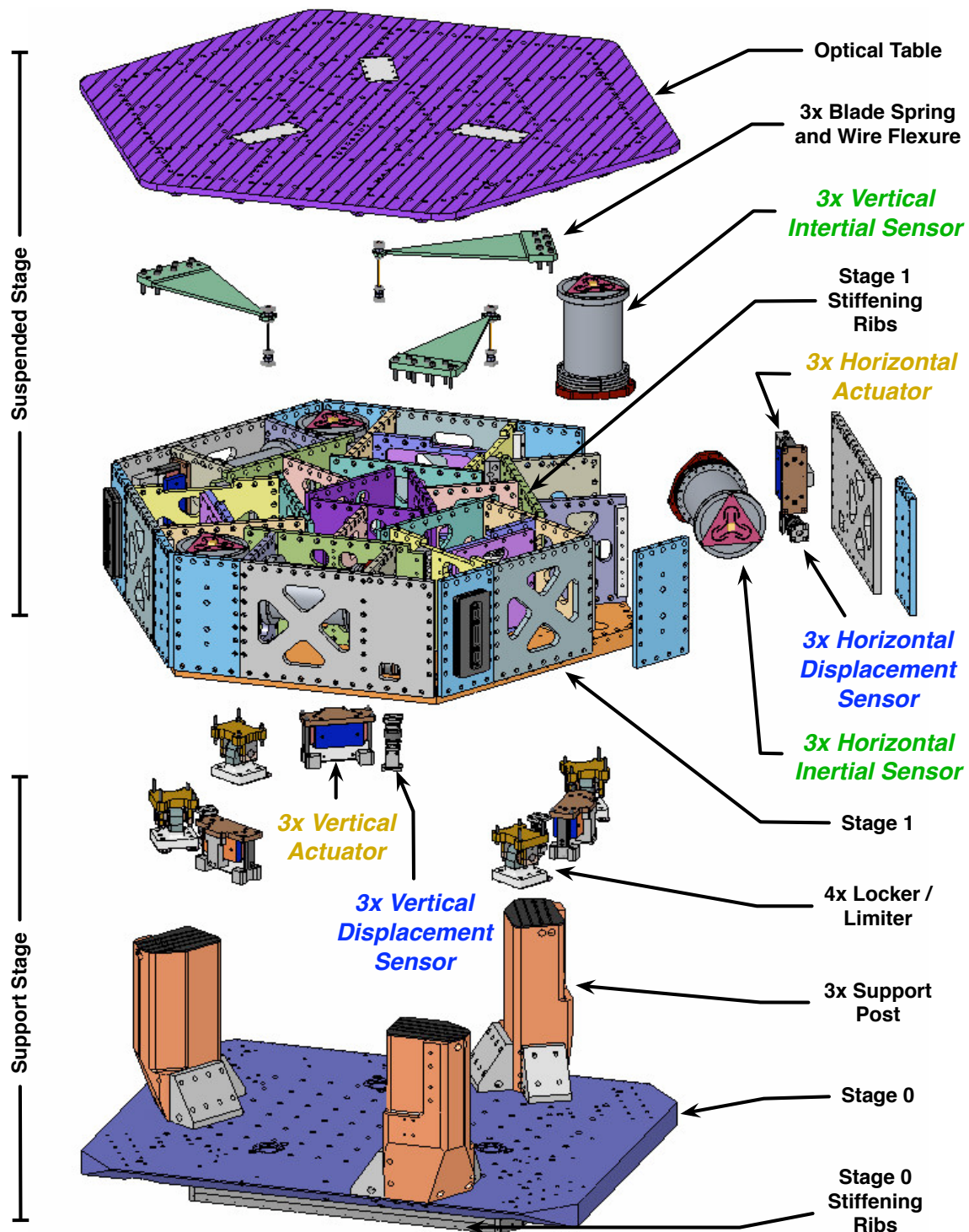


Figure 5.1: SolidWorks rendering of the HAM ISI.

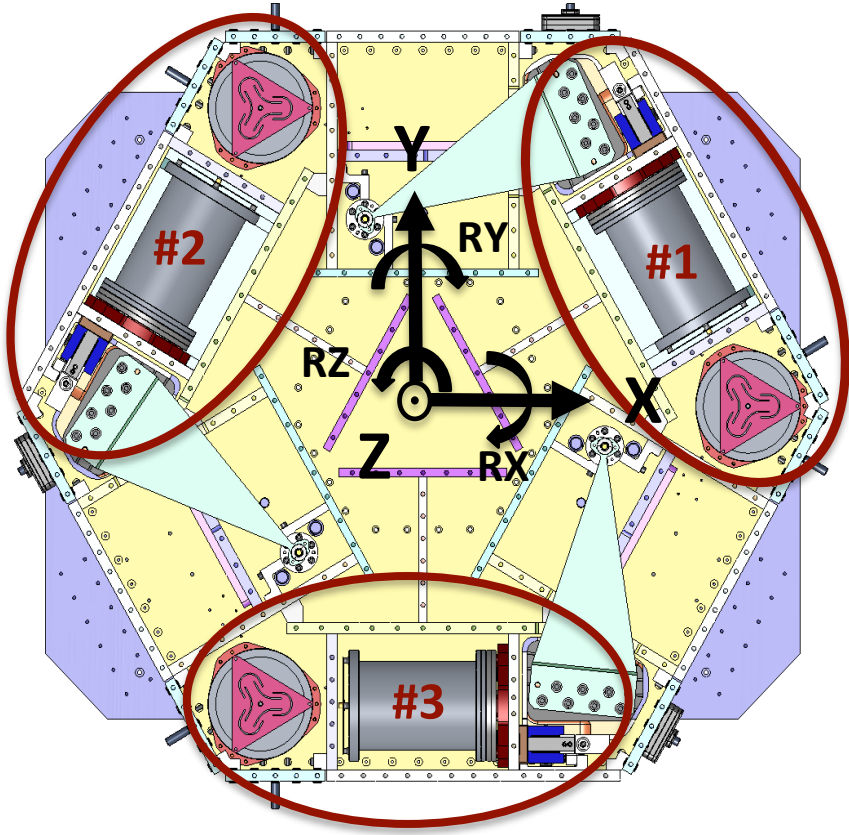


Figure 5.2: HAM ISI Colocated and Cartesian coordinate systems. The colocated basis is defined by the local clusters of instrumentation in the suspended stage. The cartesian basis, whose origin is defined by the suspended stages center of gravity, is aligned with the global interferometer's coordinate system.

and flexure system is constrained by a set of four locker/limiters. When open, they allow the table to move to  $\sim 0.5$  mm in each cartesian degree of freedom; when closed, they over-constrain the suspended stage to virtual immobility. Figure 5.3 shows a picture of the L1 HAM ISI taken just after installation.

An array of six electromagnetic linear actuators have been built internal to and around the suspended stage for active isolation and alignment. These voice coil actuators were designed to meet LIGO specifications by QinetiQ / Planning Services, Inc. (92). In practice, the actuators are only linear up to about 50 Hz, and are whitened between 0.4 Hz and 15.9 Hz with a set of analog filters between the digital-to-analog conversion.

Sensing the motion of suspended stage are colocated sets of inertial sensors and displacement sensors. These two sensor arrays both measure the same physical motion but are useful over different frequency bands. The signal from each array is digitized, rotated into the cartesian basis, normalized to have the same displacement frequency response, and then blended together using complementary low-pass  $F^{LP}$  and high-pass filters  $F^{HP}$ . The sum of the two signals is referred to as a “super sensor.”

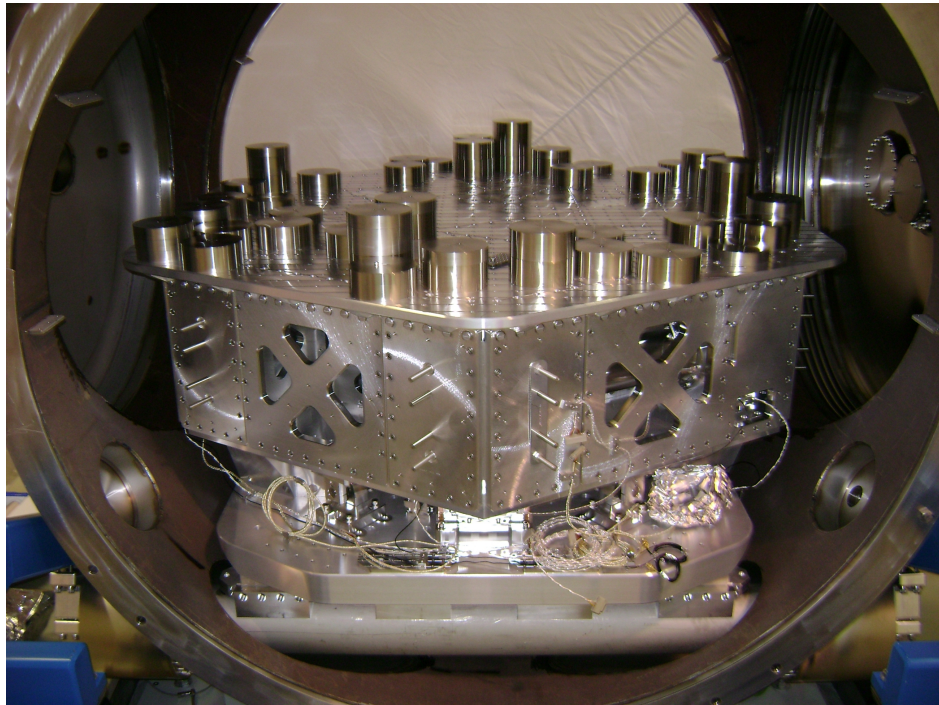


Figure 5.3: Picture of the L1 HAM ISI inside the HAM6 chamber, taken just after installation. The support tubes and support stage are visible on the bottom of the chamber, and the suspended stage takes up most of the middle of the chamber. The optical table is littered with ballast mass, required for the platform to be suspended when there is no payload.

The displacement sensor (DISP) array is a collection of six, MicroSense 8800 capacitive displacement sensors (93), three for sensing vertical and three for horizontal. Each sensor is composed of two parallel plates; one plate is bolted to the support stage, and the other is fixed to the suspended stage. As capacitance is inversely proportional to the distance between the plates, the sensor detects relative motion between the stages. This array is used below 1 Hz down to zero-frequency (DC). This sensitivity range is defined by the instrument noise floor, and the sensitivity to support stage motion above the rigid-body resonances of the suspended stage. The inertial sensor (GEO) array, mounted in the suspended stage is composed of six single degree of freedom inertial sensors. These are GeoTech GS-13 short-period, single axis seismometers (94), or geophones. The geophones are used to determine motion of the suspended stage above about 0.1 Hz. The sensitivity is limited by the noise floor of the instrument at low-frequencies, and notably by tilt of the platform in the horizontal sensors (discussed in Appendix D). Finally, we improve the performance of the displacement sensors by correcting their signal in a 0.1-1 Hz band with a tri-axial inertial sensor on the ground with much better displacement noise performance, a Streckheisen STS-2. Figure 5.4 shows the model displacement noise for each type of sensor used in the HAM ISI.

As the horizontal inertial sensors are limited by tilt-horizontal coupling (see Appendix D), several characteristics of the mechanical design have been developed to reduce the amount of platform tilt under translation. The horizontal actuation plane is designed to be within 10 cm of the vertical center of mass of the suspended stage. This offset (or lack-there-

Table 5.1: Measured properties of prototype HAM ISI mechanical structure.

Property	DOF	H1	L1
Resonant Frequency, $f_0$ [Hz]	X/Y	1.25	1.28
	Z	1.85	1.80
	RX/RY	1.05	1.00
	RZ	0.85	0.8
Blade Spring/Flexure Stiffness, $k$ [N/m or Nm/rad]	X/Y	1.39e5	–
	Z	2.76e5	2.67e5
	RX/RY	2.43e4	–
Offset, LZMP from Actuator Plane, $d$ [mm]	–	1.485	0.725

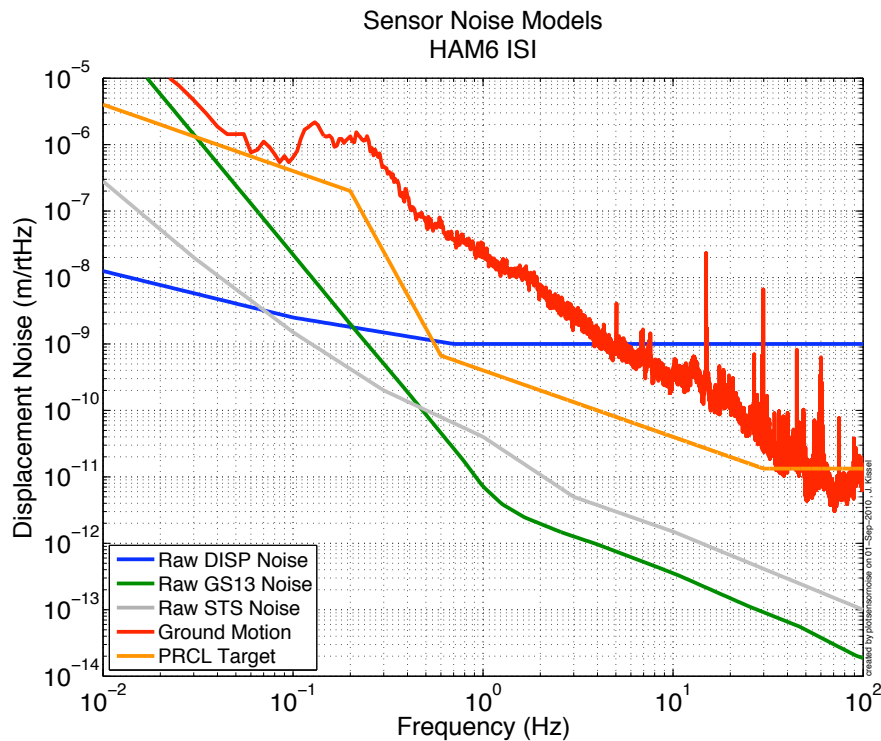


Figure 5.4: Sensor noise models for individual sensors on the HAM ISI, derived from (15). DISP corresponds to the measured noise of the MicroSense capacitive position sensors (used as displacement sensors), and is a factor of 5 above the predicted displacement noise in (15). GS13 corresponds to the best measured noise performance of the GeoTech GS-13, as in (15). STS is a model of the Streckheisen STS-2 derived from a combination of the best measured displacement noise of the Nanometrics Trillium 240 down to 0.5 Hz, and the vendor specifications below 0.5 Hz.

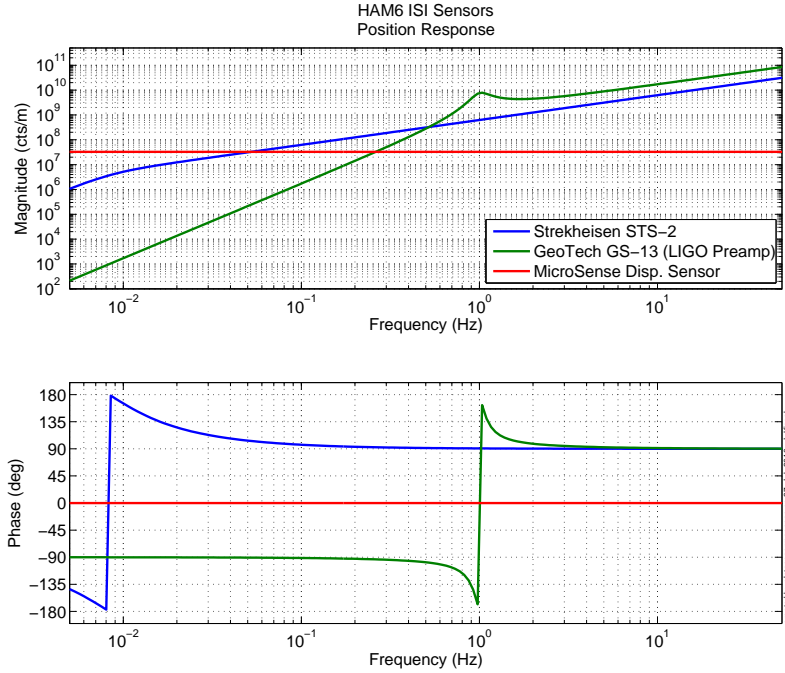


Figure 5.5: Displacement response for Enhanced LIGO sensors. All sensors are readout by a  $2^{16}/40$  cts/V ADC. The GS-13 and STS-2 have generator constants of 2200 and 1500 V / (m/s), respectively, however the GS-13 is amplified by an additional factor of 40.2 to improve its signal-to-noise ratio. The corner frequencies for GS-13 and STS-2 are 1 Hz and 8.3 mHz. The Microsense displacement sensors have a sensitivity of 10 V / mm.

of) ensures the translation and rotational degrees of freedom are independent enough for linear SISO control. Further, the flexure length, shape and stiffness have been designed such that actuation plane is less than  $h = 1$  mm of the lower zero moment plane of the flexure (the point in the pendulum-like flexure at which rotational torque and translational force are balanced producing only translational motion of the suspended mass). This offset (or lack-there-of), in combination with the designed translational and rotational stiffness,  $k_{x_{pm}}$  and  $k_\theta$  of the flexures, yields a tilt-horizontal coupling frequency of less than  $f_{thc} = (1/2\pi)\sqrt{(g h k_{x_{pm}}/k_\theta)} \sim 0.03$  Hz, allowing for the use of the inertial sensors as a strictly horizontal sensor down to this frequency.

Though not a part of the design of the HAM ISI itself, it will become important later to note the support structure upon which the prototype HAM ISIs lie. First, the support structure does not have external pre-isolation from a HEPI system. In addition, the support tubes are connected to angled struts external to the vacuum system where attached to piers on the ground. These struts are referred to as “gullwings” because of their characteristic shape. Figure 5.6 shows a picture of this support structure.

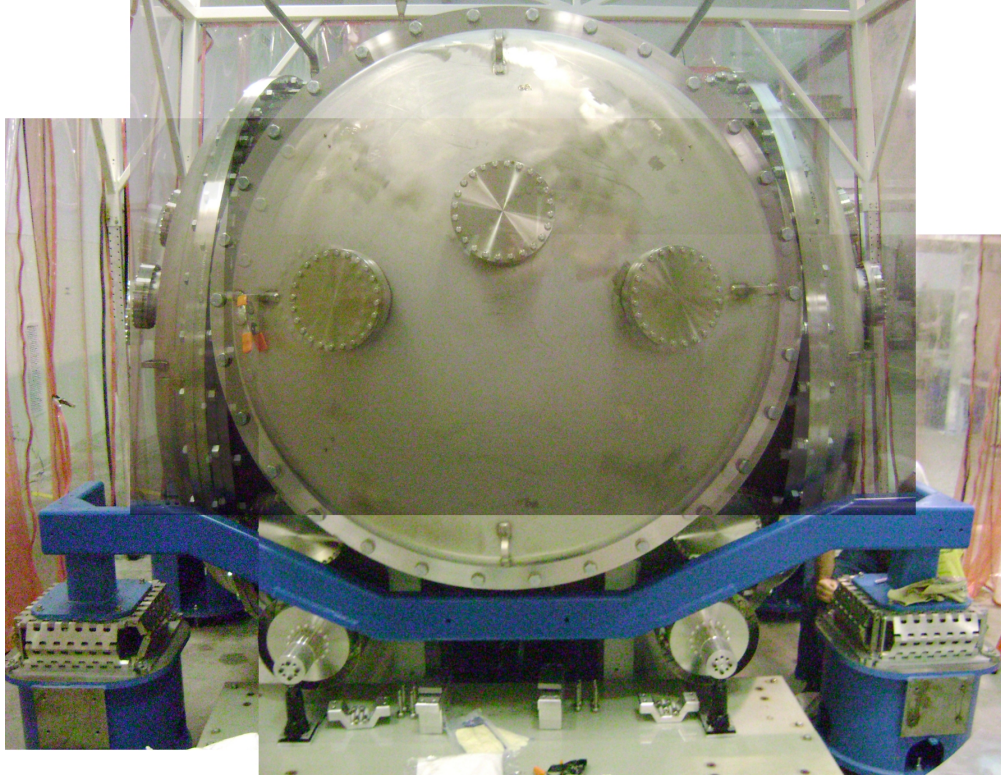


Figure 5.6: External view of the L1 HAM 6 Chamber. The angled struts, or “gullwings” which connect the support tubes to the ground piers, run across the bottom of the picture painted in blue.

## 5.2 Active Control Model

As described in section 5.1, a great deal of care was taken to make a stiff, light mechanical structure with very little cross coupling between the six cartesian degrees of freedom. We benefit from this hard work by employing six, independent, single-input, single-output control loops, whose input signal is composed of the super sensor. We model each control loop to aid the design of the loop’s digital filters and predict the platform’s performance.

The model for the X (and Y) degree of freedom is shown in Figure 5.7. Ground motion,  $x_g$ , is suppressed by the transmission of the passive isolation system, called the “plant,”  $P_x$ . Residual motion is sensed by the displacement and inertial sensors. The displacement sensor signal, sensitive to both platform motion and support stage motion, is corrected for motion of the support stage with a ground inertial sensor signal, high-passed with a filter set  $F_x^{FF}$ , in a feed-forward path. The corrected displacement sensor signal is then low-passed with  $F_x^{LP}$ . The inertial sensor signal is high-passed with a filter  $F_x^{HP}$ , complementary to  $F_x^{LP}$ . From there, the signals are added to form the super sensor. A final control filter  $K_x$  shapes the super sensor signal into a force which is fed back to the actuators, further reducing the motion of the platform.

In addition to ground motion,  $x_g$ , we include several noise sources which we measure or model. For translational degrees of freedom (X and Y), these sources are sensor noise

from each of the sensors: the on-board inertial sensors,  $n_G$ , the displacement sensors  $n_D$ , and ground inertial sensor  $n_S$ ; and residual tilt of the platform,  $t_p$ . We will find that these noises are those limiting the platform performance. Other, non-limiting, noise sources not considered include ground tilt coupling into the ground inertial sensor translation signal, actuator noise, ADC/DAC noise, and non-linear coupling.

The frequency response from the sensors and output from actuators have been compensated and given the appropriate gain to transfer any information in the colocated basis (e.g. sensor noise) into the cartesian basis. The raw sensor's displacement noise (Figure 5.4) for the three on-board sensors (DISPs and GEOs) that make up a given signal in the cartesian basis are assumed to be independent and therefore added in quadrature. The noise for the STS is already in the cartesian basis, and is assumed to be similar for all three degrees of freedom.

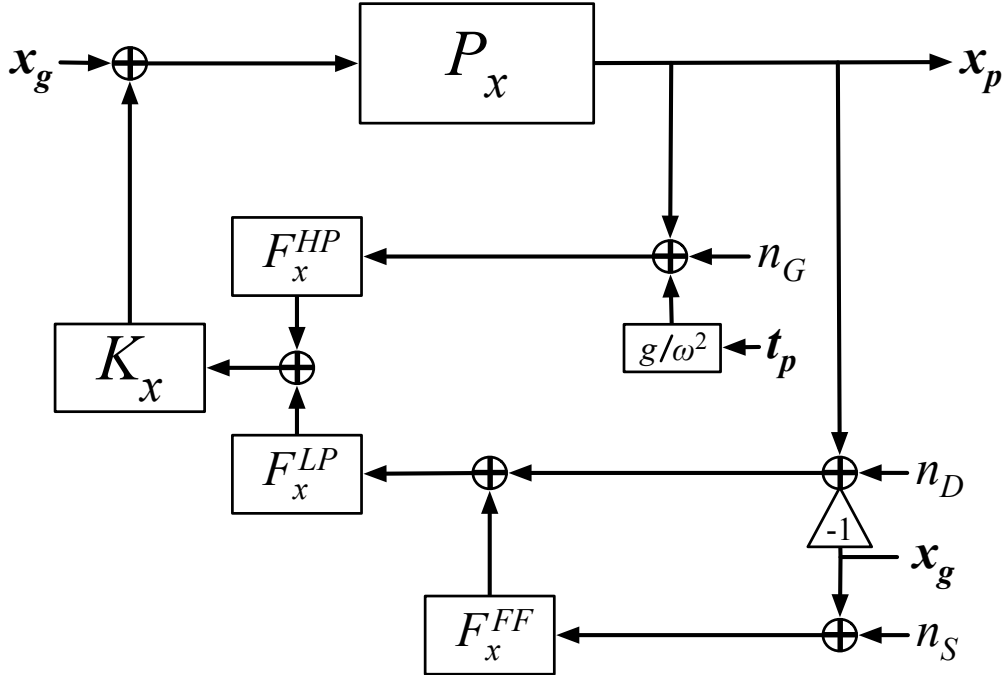


Figure 5.7: Model of active control loop and noise couplings to the platform motion  $x_p$ . The loop shown is for the X translation direction, but where appropriate, noise couplings are treated to be same for all degrees of freedom. These noise sources are input ground motion,  $x_g$ ; sensor noise from the on-board geophones,  $n_G$ , the capacitive displacement sensors  $n_D$ , and ground inertial sensor  $n_S$ ; and platform tilt noise (originating from residual ground motion or sensor noise).

The horizontal platform motion  $x_p$  is determined by working counter-clockwise through the model

$$x_p = P_x x_g + P_x K_x \left[ F_x^{HP} \left( x_p + n_G^x + \frac{g}{\omega^2} t_p \right) + F_x^{LP} (x_p - x_g + n_D^x) + F_x^{LP} F_x^{FF} (x_g + n_S) \right]. \quad (5.1)$$

Defining the open loop transfer function,  $G_x$ , as

$$G_x = P_x K_x (F_x^{HP} + F_x^{LP}) = P_x K_x, \quad (5.2)$$

where we have used  $(F_x^{HP} + F_x^{LP}) = 1$  because they are designed as a complementary pair (see discussion in Section 5.3.2), then we may solve for the platform motion in terms of the uncorrelated noise source terms,

$$\begin{aligned} x_p &= \frac{G_x}{(1 - G_x)} \left( \frac{P_x}{G_x} - F_x^{LP} + F_x^{LP} F_x^{FF} \right) x_g \\ &\quad + \frac{G_x}{(1 - G_x)} F_x^{HP} \frac{g}{\omega^2} t_p \\ &\quad + \frac{G_x}{(1 - G_x)} F_x^{HP} n_G^x \\ &\quad + \frac{G_x}{(1 - G_x)} F_x^{LP} n_D^x \\ &\quad + \frac{G_x}{(1 - G_x)} F_x^{LP} F_x^{FF} n_S \end{aligned} \quad (5.3)$$

We use this model for the two translational degrees of freedom,  $X$  and  $Y$ . Of particular note: in absence of sensor noise  $n_G^x$ ,  $n_D^x$ ,  $n_S^x$ , and if the tilt of the platform  $t_p$  is sufficiently small, at frequencies below 10 Hz where the open loop transfer function has magnitude  $|G| \gg 1$ , the plant has magnitude  $|P| \approx 1$ , the performance of the platform is determined by the shape of the displacement sensor blend filter  $F_x^{LP}$ , and the complement of the feed forward filter  $(1 - F_x^{FF})$ ,

$$x_p(f < 10 \text{ Hz}) \approx F_x^{LP} x_g - F_x^{LP} F_x^{FF} x_g = F_x^{LP} (1 - F_x^{FF}) x_g. \quad (5.4)$$

This fact will play an important role in the design of each of these filters.

The remaining degrees of freedom are calculated in a similar fashion, but are simpler because they are insensitive to tilt of the platform. The model for vertical motion,  $z_p$ , tilt,  $t_p = rx_p = ry_p$ , and rotation about the Z axis,  $rz_p$  are,

$$\begin{aligned} z_p &= \frac{G_z}{1 - G_z} \left( \frac{P_z}{G_z} - F_z^{LP} + F_z^{LP} F_z^{FF} \right) z_g \\ &\quad + \frac{G_z}{(1 - G_z)} F_z^{HP} n_G^z \\ &\quad + \frac{G_z}{(1 - G_z)} F_z^{LP} n_D^z \\ &\quad + \frac{G_z}{(1 - G_z)} F_z^{LP} F_z^{FF} n_S \end{aligned} \quad (5.5)$$

$$t_p = \frac{G_t}{(1 - G_t)} \left( \frac{P_t}{G_t} - F_t^{LP} \right) t_g + \frac{G_x}{(1 - G_x)} F_x^{HP} n_G^t + \frac{G_x}{(1 - G_x)} F_x^{LP} n_D^t \quad (5.6)$$

$$rz_p = \frac{G_{rz}}{(1 - G_{rz})} \left( \frac{P_{rz}}{G_{rz}} - F_{rz}^{LP} \right) rz_g + \frac{G_{rz}}{(1 - G_{rz})} F_{rz}^{HP} n_G^{rz} + \frac{G_{rz}}{(1 - G_{rz})} F_{rz}^{LP} n_D^{rz} \quad (5.7)$$

We use Eqs. 5.3 through 5.7, with known models of the sensor noise and plant to guide the design of the blend filters.

## 5.3 Active Control Design

Developing optimized control loops for the HAM ISI is a multistage, iterative process of measurements and tuning. In order to use the complement of sensors, system identification measurements are required with the platform in the two bases, in various configurations, and over different frequency ranges. In this section we describe the details of the measurement, design, and optimization process. The active control system serves to isolate the table from ground by driving the table into the local inertial frame. To achieve this the blend cross-over frequency must be as low as possible. This is limited by the inertial sensor's sensitivity to tilt at low frequencies (as per Eq. 6.64). Thus, several steps are taken during the commissioning process that are solely to remove excess tilt from the platform motion, and diagonalize the control of the six degrees of freedom.

We commission the damping loops first, in order to reduce the Q of the known resonant features in the plant. This allows for a stable plant upon which to design the isolation loops. Next, we install simple blend filters with a high-cross over frequency such that the control authority is dominated by the displacement sensors at low frequency. This allows for measurement of the tilt-horizontal coupling induced by the displacement sensors. Such measurements are used to compute small de-coupling coefficients in the displacement sensor path, which reduce low-frequency cross-soupling between translation and tilt. Finally, we design and install optimized blend filters with as low a cross-over frequency as possible, redesign the isolation loops if necessary, and implement the feed-forward sensor correction path. The details of these steps are described below.

### 5.3.1 Damping Loops

The damping loops are simple feedback loops using only the inertial sensor velocity signals in the colocated basis. These loops are designed to be unconditionally stable, with authority only around the known resonant frequencies of the blade spring wire flexure system, to reduce the Q of the rigid body translational and rotation modes of the suspended stage. We take advantage of the symmetry of the platform, and design a single filter for all three horizontal colocated degrees of freedom (H1, H2, and H3) and a single filter for the vertical colocated degrees of freedom.

The damping loop control filter modifies the inertial sensor velocity signal in a few simple ways. First, the GS-13 frequency response (Figure 5.5), is modified with an inversion filter to behave like a critically damped inertial sensor whose corner frequency is at 0.2 Hz instead of the natural response of the GS-13 with a corner frequency at 1 Hz with the Q of  $\approx 5$ . This simplifies the loop design by moving the resonant feature inherent to the instrument out of the 1 Hz region, containing the platform resonances the loop is trying to control. Second, the actuator whitening is removed. Finally, a high pass filter with corner frequency at 0.04 Hz ensures the signal is AC coupled, removing contributions from static offsets, and ultra-low frequency noise. Figure 5.8 shows the colocated inertial sensor plant, the control filter, the open loop transfer function ( $G = \text{plant} \times \text{control filter}$ ), and expected suppression ( $1/(1+G)$ ). Figure 5.9 demonstrates the reduction in Q of the blade-spring wire-flexure resonances in the cartesian basis, measured by the inertial sensors.

### 5.3.2 Blend Filters

The response of the super sensor is used as the error signal in the isolation feedback control loop. There are several advantages to using the super sensor as the error signal (90):

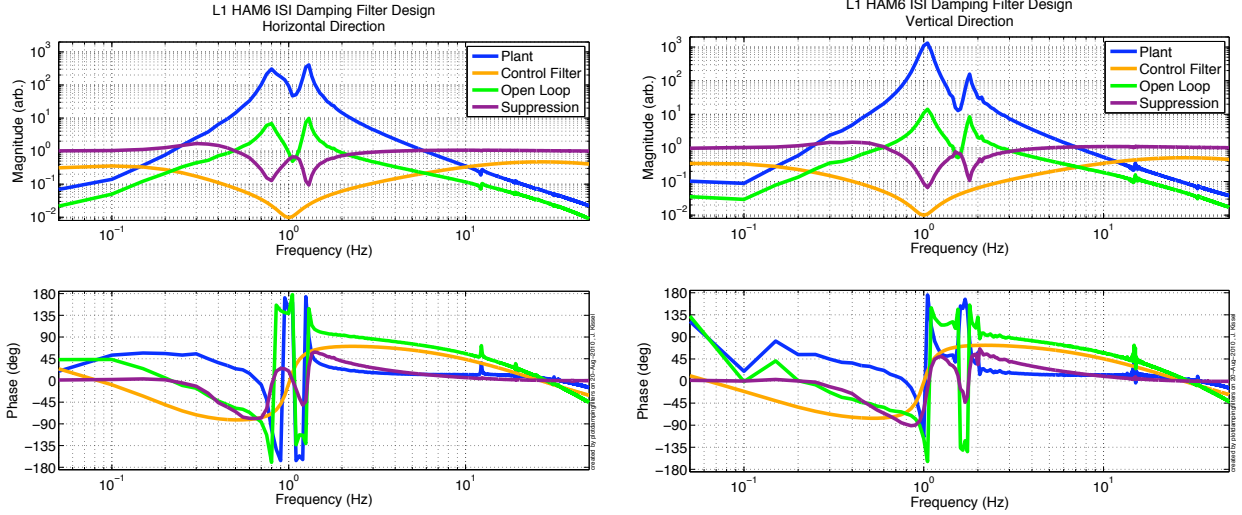


Figure 5.8: Damping loop control filter design for L1 HAM6 ISI, for the horizontal colocated inertial sensors (left), and vertical colocated sensors (right).

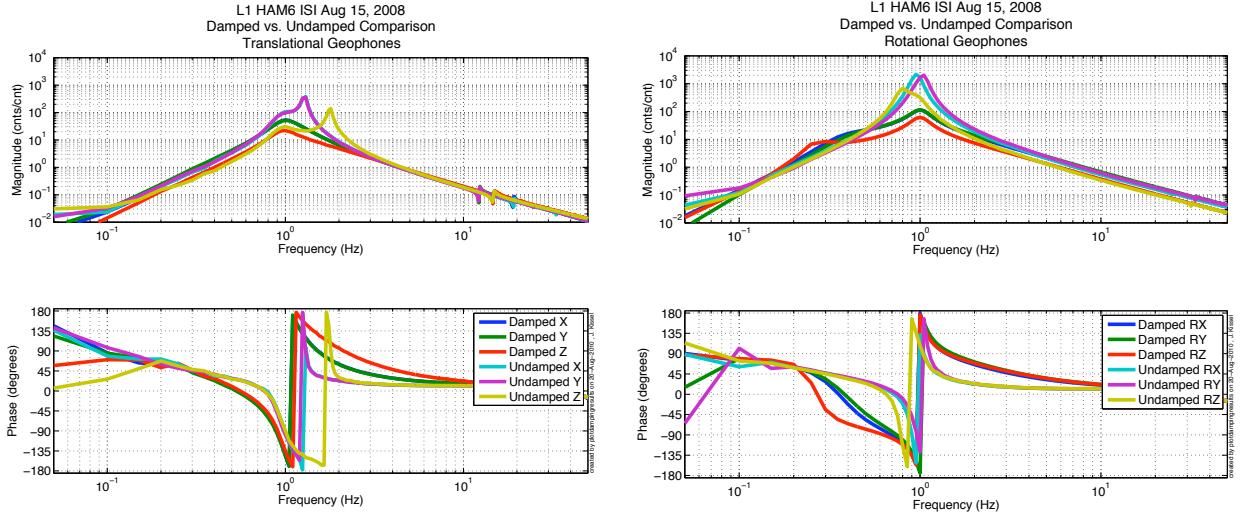


Figure 5.9: Comparison of transfer functions between drive and inertial sensor response in the cartesian basis with damping loops open vs. closed. Translational degrees of freedom are shown on the left, and rotational degrees of freedom on the right.

1. The super sensor will have lower noise than either of the individual sensors alone, over a broad frequency range. The displacement sensors have better noise performance at low frequency, and the inertial sensors at high frequency (See Figure 5.4).
2. The displacement sensors have sensitivity down to zero frequency, allowing for active control of platform alignment. In addition, the control loop may have authority down to zero frequency, instead of a lower unity gain crossing (as with the damping loops) easing control filter design.

3. Unlike the horizontal geophones, the displacement sensors are insensitive non-linear tilt-horizontal coupling at low frequency.
4. Displacement sensors may be corrected using a single (rather expensive) ultra-low noise inertial sensor on the ground (see Section 5.3.5).

Once rotated into the cartesian basis, the inertial sensors and displacement sensors are still in units of arbitrary digital counts of velocity and displacement, respectively. We use the blend filters to serve a two-fold purpose: to remove the sensor response (Figure 5.5), such that both types of sensors are calibrated in physical displacement units of  $nm$ , and to combine these signals with appropriate complementary authority to form the super sensors. These two functions in principle may be separated into two separate filters, however in practice we have found that this causes instabilities in the control loop arising from limitations of the computational algorithm used to calculate the output of the digital filters (95).

Accurate sensor inversion is tested by comparing the calibrated response of both types of sensors to actuator drive. We expect the sensors to match identically within the region where we expect to blend their signals (they may deviate outside this frequency band, for example in the translation degrees of freedom in which the inertial sensors are polluted by tilt at below the band, and displacement sensors are polluted by resonant features in the support stage). Figure 5.10, demonstrates this test for the X degree of freedom of the L1 HAM6 ISI.

Once calibrated, we chose to combine the signals using complimentary high-pass  $F^{HP}$  and low-pass  $F^{LP}$  blend filters for the inertial and displacement sensors, respectively. In this case, complementary implies that the sum of the two complex filters is unity over all frequencies,

$$F^{HP} + F^{LP} = 1 \quad (5.8)$$

The advantage of using a complementary pair is that the super sensor, which serves as the input to the isolation filter control path is independent of the particular details or shape of the blend filters. This allows for the design of the isolation path control filters to be independent of the blend: the same isolation loop will remain stable under multiple configurations of the blend authority. Note that we take advantage of the symmetry in the mechanical design of the platform, and use the same set of filters for the horizontal degrees of freedom (X and Y), and for the tilt degrees of freedom (RX and RY).

We have found in Eq. 5.4, that the performance of the platform is limited by the shape of the displacement sensor blend filter,  $F^{LP}$ , below 10 Hz. We therefore design the blend filters in the following manner. For the translational degrees of freedom (X and Y), a goal is set for the blend cross-over frequency  $f_B$ , determined by the measured tilt horizontal coupling zero  $f_{thc}$ , below which we believe the translational inertial sensor signals are dominated by tilt. Above  $f_B$ , the displacement sensor low-pass,  $F^{LP}$ , is rolled off as quickly as possible. The particular type/shape of low-pass (from as simple as a few poles at the cross-over frequency, to some complicated combination of high-order butterworth or elliptic filters) may be guided by known resonant features of the payload. However, since the filters must be complementary, the shape is not totally arbitrary: there must be a trade-off between rolling off  $F^{LP}$ , while still retaining a sharp, opposing roll-off of the inertial sensor signal using  $F^{HP}$ . Recall the roll-off of the inertial sensor is to remove sensor noise and tilt-horizontal coupling, dominant below  $f_B$ . Further, because these complementary filters must be combined with the sensor response, particular attention must be paid to the high-pass filter  $F^{HP}$ : the inertial sensor response has 3 poles at DC, so the blend filter must have at least 4 zeros to ensure that they still remain AC coupled.

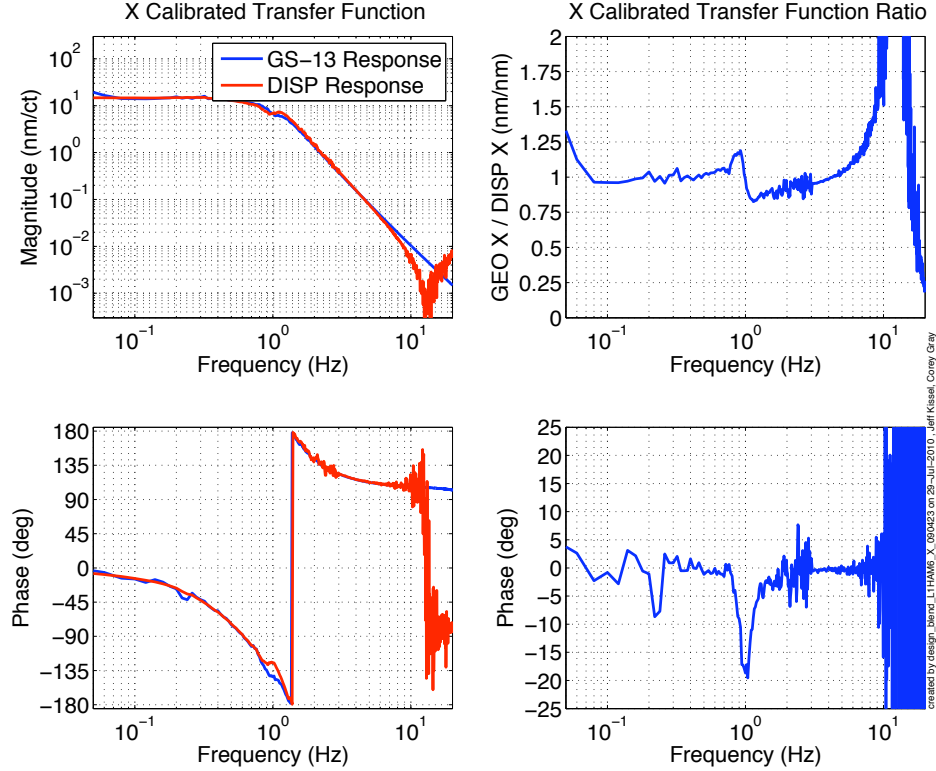


Figure 5.10: Demonstration of calibration accuracy for blend filter design. (Left) Response of displacement sensors and inertial sensors in the X direction, in response to X input. (Right) Ratio between responses. The feature at 1 Hz is from imprecise modeling of the GS-13 instrument response (i.e. the corner frequency and Q are not exactly 1 Hz and 5, respectively). The response of the displacement sensor significantly deviates from the geophone response above 10 Hz due to a resonance in the support structure.

Similar rules are applied in the design of the blend filters for the remaining degrees of freedom. For the RX/RY blend filters, where the isolation requirements from ground are less stringent, we make a sacrifice in loop performance in order to roll off the inertial sensors at higher frequency. The motivation, again is tilt horizontal coupling. For these degrees of freedom, the cartesian inertial sensor are composed of differential signals proportional to V2 and V3 for RX and  $(V2 + V3) - V1$  for RY. Thus, by default, the signal-to-noise ratio for these loops is considerably smaller than for the remaining loops. Uncorrelated noise between these vertical sensors is mis-interpreted as real tilt motion, for which the closed tilt loops will try to correct. In turn, this excess tilt motion couples into the horizontal inertial sensors by our favorite factor  $g/\omega^2$ . Thus, the blend cross-over frequency  $f_B$  is set relatively high, and a more aggressive high-pass filter is applied to the geophones.

Figure 5.11 shows the complementary filters used for the L1 HAM6 ISI. Figure 5.12 shows the super sensor response for all six degrees of freedom. This response is the base upon which the isolation loop control filters are designed.

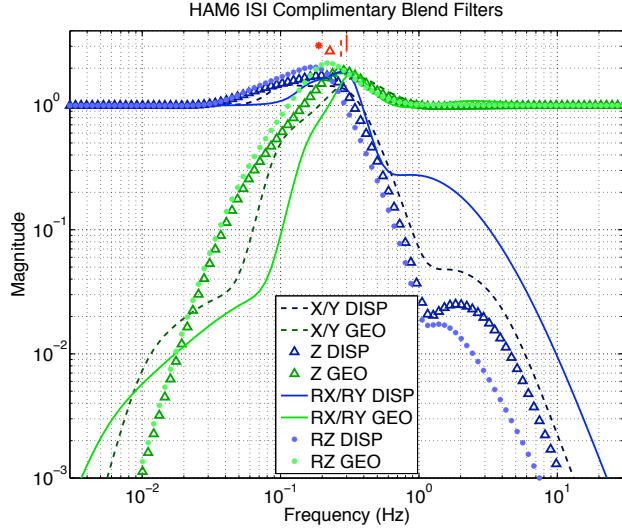


Figure 5.11: Complimentary blend filters used for L1 HAM6 ISI. The low pass filters,  $F^{LP}$  (shown in shades of blue) are used for the displacement sensors, and high pass filters  $F^{HP}$  (shown in shades of green) are used for the inertial sensors. The blend frequencies,  $f_B$ , (shown in red, with markers similar to those indicating the filters themselves) for X/Y, Z, RX/RY, and RZ are 0.27, 0.23, 0.3, and 0.19 Hz, respectively.

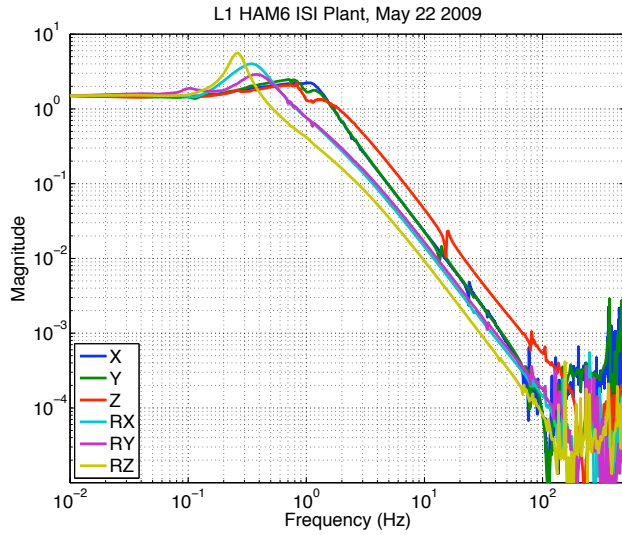


Figure 5.12: Super sensor response to actuator drive for the six cartesian degrees of freedom with damping loops engaged. Here we can fully appreciate the benefit of the simple, stiff, mechanical design. The transfer functions are flat up to the first rigid-body resonances between 0.5 and 2 Hz, and then fall smoothly as  $1/f^2$ , for 2 decades in frequency before other resonant modes begin to appear above 100 Hz.

### 5.3.3 Isolation Loops

Given the simplicity of the super sensor plant, the design of the isolation path control filters becomes relatively easy. As has been shown in Section 5.2, given sufficient loop gain  $G$ , the performance of active isolation is determined by the particular frequency response of the low-pass complementary blend filter  $F^{LP}$ . Therefore, we only need to ensure there is sufficient loop gain in regions where we wish to have active isolation, all other considerations can focused on the practical implementation of the control loops.

For clarity, we split the functionality of the isolation control filter into the product of several individual pieces. The base control filter is a simple set of poles and zeros designed to set the open transfer function unity gain frequency crossing (UGF), and provide a reasonable amount of loop gain at low frequency. This filter is designed to be unconditionally stable up to the designed UGF, such that loop control may be turned on gradually. In addition to this base line filter, interval other filters are applied in the path: a “high-frequency control filter,” and a “boost” filter. The high-frequency control filter is designed solely to reduce the contributions of the non-rigid-body resonances of the platform above 100 Hz, and to further roll off the active control signal so as to not re-introduce and sensor noise present after the sensor blending. The boost filter is applied after the baseline and high-frequency control filters have been turned on, and the loop has the desired UGF. As the name implies, it increases the low frequency gain enhancing the performance, but renders the loop only conditionally stable.

With this separation of tasks in mind, we define the following criteria for the isolation control filter design that are merely based on practicality and ease of use, rather than from a performance stand point. In no particular order,

- The designed unity gain frequency for the open loop transfer function  $G$  should be between 25 - 30 Hz. We rely on the passive isolation system to provide the bulk of the isolation above these frequencies.
- With no low-frequency boost, there should be no poles at DC (integrators) in the isolation loops. In other words the gain at DC should not be infinity. This is a conservative stability rule: we must move 1500 kg of metal when we turn on our loops.
- Again, for the non-boosted loops, we would like a phase margin of at least 40 deg at all frequencies below the designed unity gain frequency. Because we must move large amounts of mass, we ramp up the isolation loops from DC in a rather slow fashion. Hence, we want isolation loops to be unconditionally stable as the unity gain frequency sweeps from DC to the designed UGF.
- Above 100Hz, the open loop transfer function (OLG) and boosted OLG should not be above 0.1. This prevents any high frequency resonances from rearing their ugly heads unexpectedly.
- The suppression should never be greater than 3 at any frequency. This is simply because we want to keep gain peaking to a minimum. A related goal is to have the gain margin be around 4 or 5 dB. In practice, this implies that the slope of the open loop transfer function fall smoothly through the unity gain crossing, with a slope that falls inversely proportional to frequency.
- The suppression around 10 Hz (where Advance LIGO requirements are most stringent on the active control system) should be around 0.3. The criteria is restricted by the limit on suppression and the stability of the control loop.

- The low frequency boost should increase the gain at (and below) 0.1 Hz by at least 40dB (a factor of 100). The low frequency boosted isolation loop may be unconditionally stable, as long as there remains roughly 40 deg phase margin around the UGF and good suppression is maintained around 10 Hz.
- Design the loops as simply as possible. The product of the base, high-frequency, and boost control filters should not need to be more than 4 or 5 groups of 10 second order sections.
- Design and close the RX and RY isolation loops first. This significantly reduces amount of non-linear cross coupling from tilt into the translational degrees of freedom before designing the X, Y, Z, and RZ isolation loops.

Figure 5.13 show the set of isolation control loop filters used for all degrees of freedom, and Figure 5.14 shows the predicted open loop transfer function and suppression obtain from the X control filter design for the L1 HAM6 ISI.

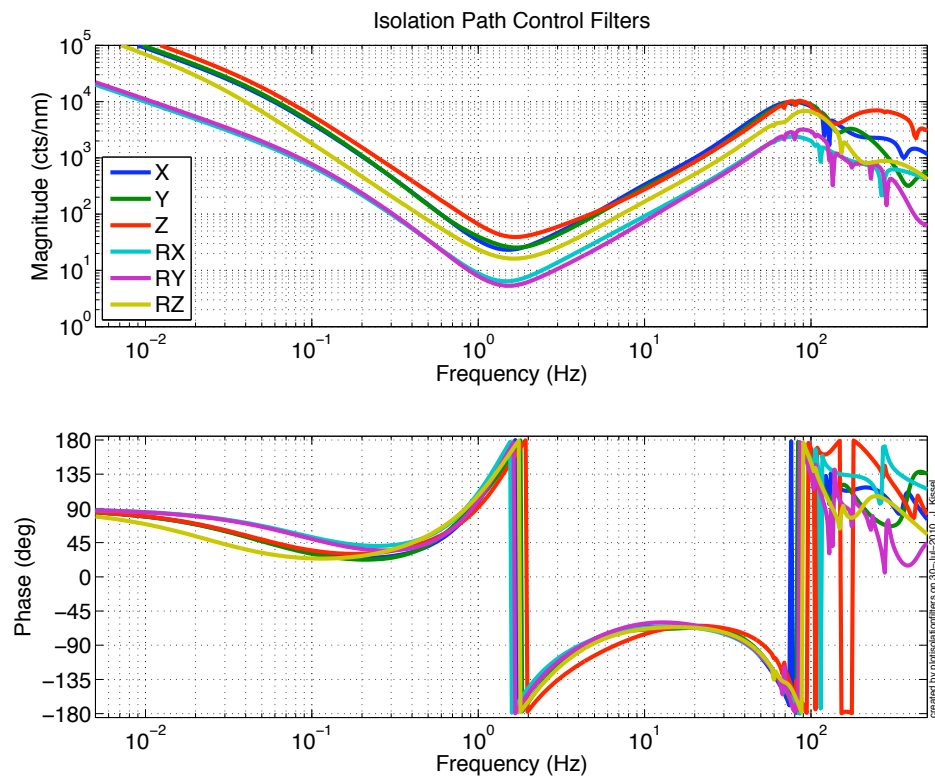


Figure 5.13: Digital control filters used to shape the super sensor signal for the L1 HAM ISI. Because the super sensor response is similar below 100 Hz for all degrees of freedom, the design of the isolation control filters is also almost identical. Above 100 Hz, resonances of the payload and internal structure of the platform require additional filtering.

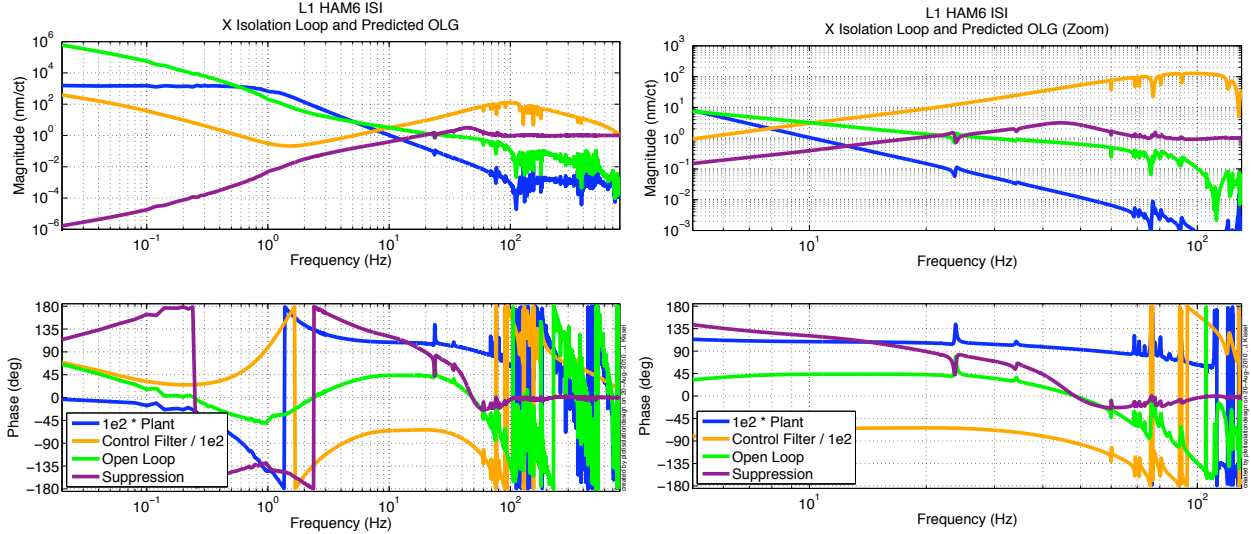


Figure 5.14: Predicted open loop transfer function and suppression for the X isolation control loop for the L1 HAM6 ISI. (Left) Filter design over the entire frequency range, (right) zoom of the design in the region around the open loop transfer function unity gain crossing. Limiting the suppression and stability for all degrees of freedom is the resonance in the support support structure around 15 Hz.

### 5.3.4 Displacement Sensor Alignment

An additional source of low-frequency tilt horizontal coupling may be the misalignment of the capacitive position sensor plates. The sensor heads (on support stage) are designed with the ability to swivel about their mounts, where the sensor target (on the suspended stage) is fixed. This way, if for some reason the target mounting is poorly constructed, the sensor head may be adjusted to compensate. However, even the best construction and mechanical adjustment may leave residual misalignment between the plates. Figure 5.15 demonstrates interval examples of how this alignment may effect the sensed motion of the table.

In order to compensate for this excess tilt-horizontal coupling, we add an additional alignment matrix in the displacement sensor path, before sensor correction. Measurement of this cross-coupling is performed by driving the table at low frequencies with the table controlled by the isolation path using a set of blend filters with high ( $\simeq 1$  Hz) cross-over frequency. The metric for the coupling is the response of an inertial sensor (the cartesian transform of the on-board geophones for L1 HAM6 ISI, or a “witness” STS-2 on the optical table for H1 HAM6 ISI), normalized by the displacement sensors. The normalization removes the actuator response from the measurement, and also removes any confusion between tilt caused by the actuators. The resulting transfer function,  $T_{x \rightarrow x}$  is fit to a linear combination of a model of a purely translational geophone response,  $x_{pm}/x_{sp}$  and of the response under the influence of tilt,  $x_{pm}/\theta$ ,

$$T_{x \rightarrow x} = C_{x \rightarrow x} \left( \frac{x_{pm}}{x_{sp}} \right) + C_{x \rightarrow ry} \left( \frac{x_{pm}}{\theta} \right) \quad (5.9)$$

The inertial sensor response to X drive gives a metric of the tilt in RY, and Y for RX. Figure 5.16 demonstrates this model for the X direction of the H1 HAM6 ISI. The ratio of the

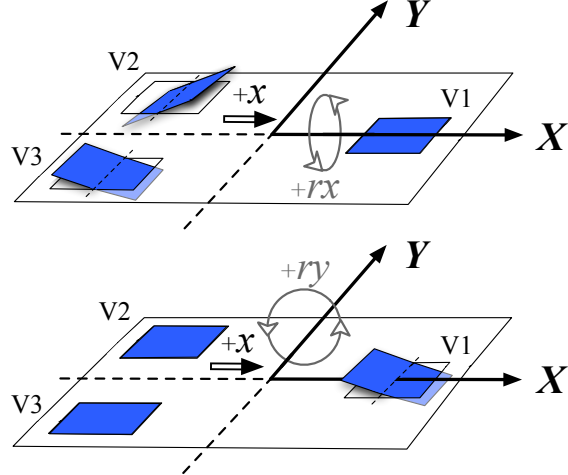


Figure 5.15: Examples of tilt-horizontal cross coupling generated by misaligned capacitive position sensor plates. (Top) Sensor V1 is misaligned from the  $x/y$  plane, such that a real platform translation in the  $+x$  direction is misinterpreted as platform tilt in the  $+rx$  direction, shown in grey. (Bottom) Sensors V2 and V3 are misaligned in opposing directions from the  $x/y$  plane, such that a real platform translation in  $+x$  is misinterpreted as platform tilt in the  $+ry$  direction.

coefficients for translation, is used as the matrix element. The measurement is performed for a drive in X, Y, and Z, yielding an alignment matrix,

$$M_{DA} = \begin{pmatrix} 1 & 0 & 0 & 0 & 0 & 0 \\ 0 & 1 & 0 & 0 & 0 & 0 \\ 0 & 0 & 1 & 0 & 0 & 0 \\ C_{x \rightarrow rx}/C_{x \rightarrow y} & C_{y \rightarrow rx}/C_{y \rightarrow y} & C_{z \rightarrow rx}/C_{z \rightarrow y} & 1 & 0 & 0 \\ C_{x \rightarrow ry}/C_{x \rightarrow x} & C_{y \rightarrow ry}/C_{y \rightarrow x} & C_{z \rightarrow ry}/C_{z \rightarrow x} & 0 & 1 & 0 \\ 0 & 0 & 0 & 0 & 0 & 1 \end{pmatrix} \quad (5.10)$$

For both H1 and L1 HAM ISI, these coefficients shown in  $M_{DA}$  are of order  $10^{-3}$ . Though other elements in the matrix are in principle present, they are difficult to model and quantify in as clear a manner as with those represented. We also found from empirical experiments that these coefficients are of order  $10^{-4}$  or less.

Figure 5.17 shows an example improvement gained by installing the  $X \rightarrow RY$  Matrix element. Similar improvement is achieved for other degrees of freedom.

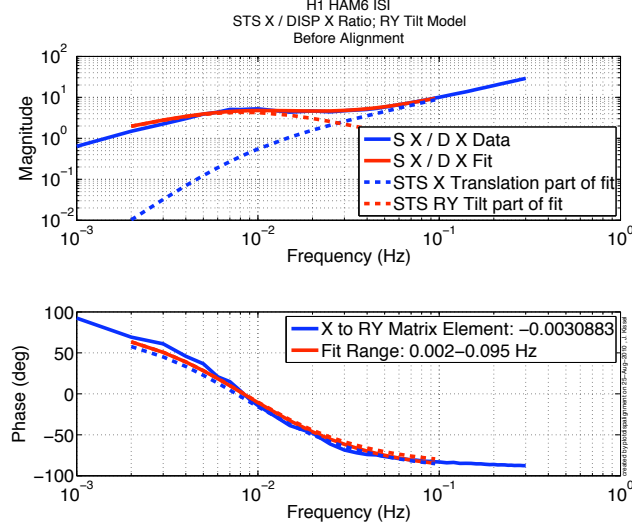


Figure 5.16: Model and measurement of the X response to X drive (in displacement units), before displacement sensor alignment. The measurement is the ratio of a witness STS-2 and cartesian transform of the displacement sensors. The data is shown in solid blue, translational and tilt portions of the model are shown in dashed blue and red (respectively), and the total model is shown in solid red. We see the tilt horizontal coupling frequency is  $f_{thc} = 30$  mHz, and the curvature is negative as there is response minimum.

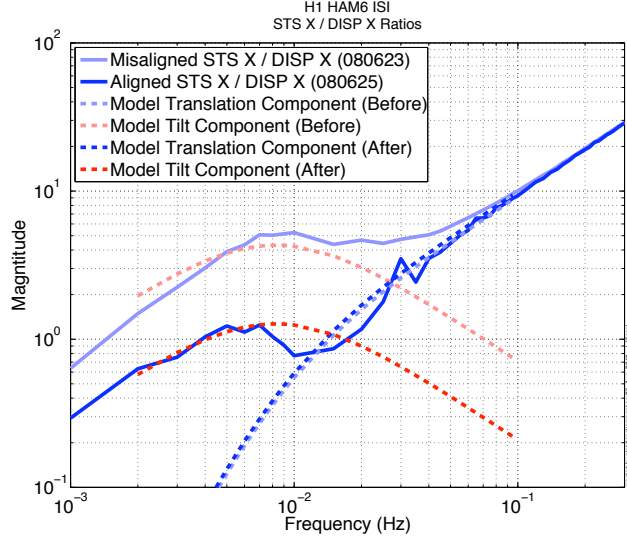


Figure 5.17: Example improvement gained using the displacement sensor alignment coefficient  $C_{x \rightarrow ry}$ , for the H1 HAM6 ISI. The data shows that the tilt due to horizontal drive has reduced by a factor of 4, and  $f_{thc}$  has moved from 30 mHz to 15 mHz.

### 5.3.5 Sensor Correction

The displacement sensor signal is composed of the difference between the motion of the support stage and the suspended stage. The support stage, however, is moving with ground motion. To reduce the support stage's undesired contribution to the displacement sensor signal, we set up an independent inertial sensor on the ground and “correct” the displacement sensor using its signal. This is done using a feed-forward topology. The design of the filter is a trade off between noise of the ground inertial sensor (instrument noise or false translational signal from tilt) and gain match between the inertial sensor and displacement sensors (96; 97). As described in Appendix D, at frequencies below 50 mHz, an inertial sensor’s translational signal is dominated by false interpretation of tilt as translation. In frequency band to be corrected, the gain of the feed-forward signal must match that of the displacement sensor signal for maximum cancellation. In this sense, one can imagine such sensor correction as merely a subset of complementary blend filters as described in Section 5.3.2, where desired feed-forward filter has frequency response similar to the high-pass component of the blends.

Digital filters with finite or infinite impulse response (FIR and IIR filters, respectively) may be used a feed-forward system. In the case of an FIR filter, because the frequency response of the filter is merely the Fourier transform of its coefficients, convex optimization tools can be employed to satisfy the criteria given (96). An additional advantage is the filter may have very sharp frequency discrimination. The main disadvantage of an FIR filter is the high computational cost. In our case, a hybrid, “polyphase” FIR filter system  $F^{FF}$  has been designed (97), that both meets the stringent requirements with relatively low computational cost. The topology of this filter system is shown in Figure 5.18.

The core of the hybrid system is a  $N=128$  coefficient polyphase FIR high-pass filter sampled at  $f_s = 2$  Hz. Between  $f_s$  and  $f_s/N$ , the polyphase FIR filter exactly replicates the desired frequency response. Below  $f_s/N$ , the filter has non-ideal response because this filter is finite. Above  $f_s$ , there exist periodic, aliased, Fourier reflections of the filter response between integer multiples of  $f_s$ . To combat these out-of-band, undesired properties, we split ground signal into interval parallel paths: one in which the FIR filter is applied and the other in which it is not, and then sum the interval paths before being sent to correct the displacement sensors. In the FIR path, we apply a low-pass filter which goes to unity below  $f_s$  rolling off the Fourier reflections above  $f_s$ , and a very-low-frequency high-pass filter whose corner frequency is slightly lower than  $f_s/N$  to reduce the non-ideal finite response. In parallel path, we include a high-pass filter, complementary to the FIR path’s low-pass filter that ensures the total path is unity at high frequency. The frequency response of the total path and each component are shown in Figure 5.19.

The optimal filter for the sensor correction path can be directly measured. The ratio of the closed-loop platform response,  $x_p$ , to ground motion,  $x_g$ , and to an excitation injected just after sensor correction path,  $x_D$ , yields the optimal transfer function between ground motion and sensor correction path,

$$\frac{x_p/x_g}{x_p/x_D} = \frac{x_D}{x_g} = F_{opt.}^{FF} \quad (5.11)$$

Figure 5.20 shows a comparison between the measured optimal filter and the polyphase FIR filter system used for all three degrees of freedom. Though it is clear there is some frequency-dependent gain mismatch between 0.1 and 1 Hz, the mismatch is less than 20% and 5 degrees across the frequency band in which sensor correction improves the performance of the displacement sensors.

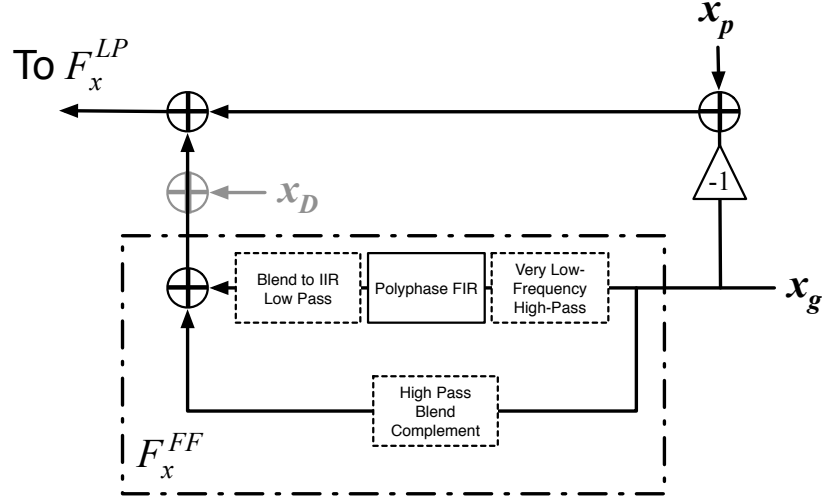


Figure 5.18: Details of the feed forward path for the displacement sensors (zoom from Figure 5.7). The displacement sensors measure the difference between ground motion and platform motion. The components of total feed forward filter  $F_x^{FF}$  (dash-dotted box), include a polyphase FIR filter (solid box), and several other IIR filters (dash boxes) which serve to remove undesired features of the practical implementation of the FIR filter.  $x_D$  is the drive signal temporarily injected to measure the optimal filter for  $F_x^{FF}$ , the excitation.

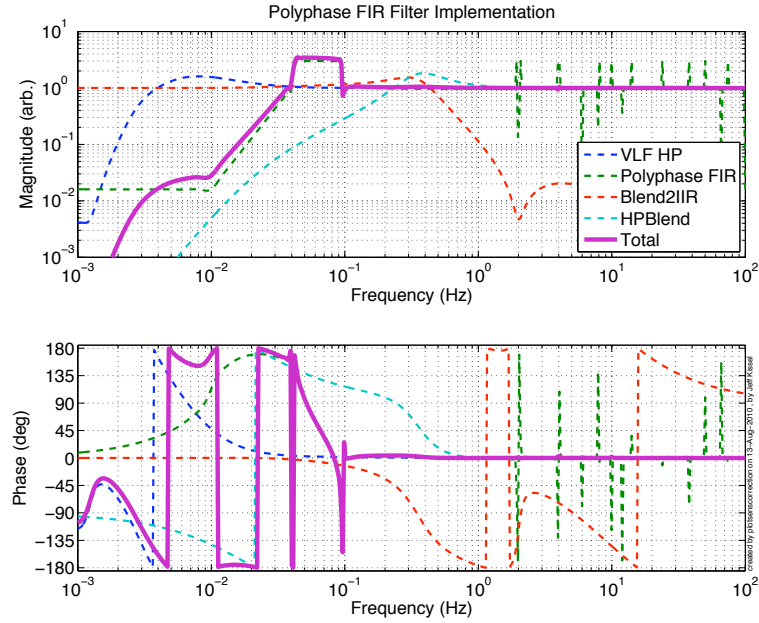


Figure 5.19: Frequency response (in velocity units) of filters used to implement hybrid polyphase FIR feed forward loop.

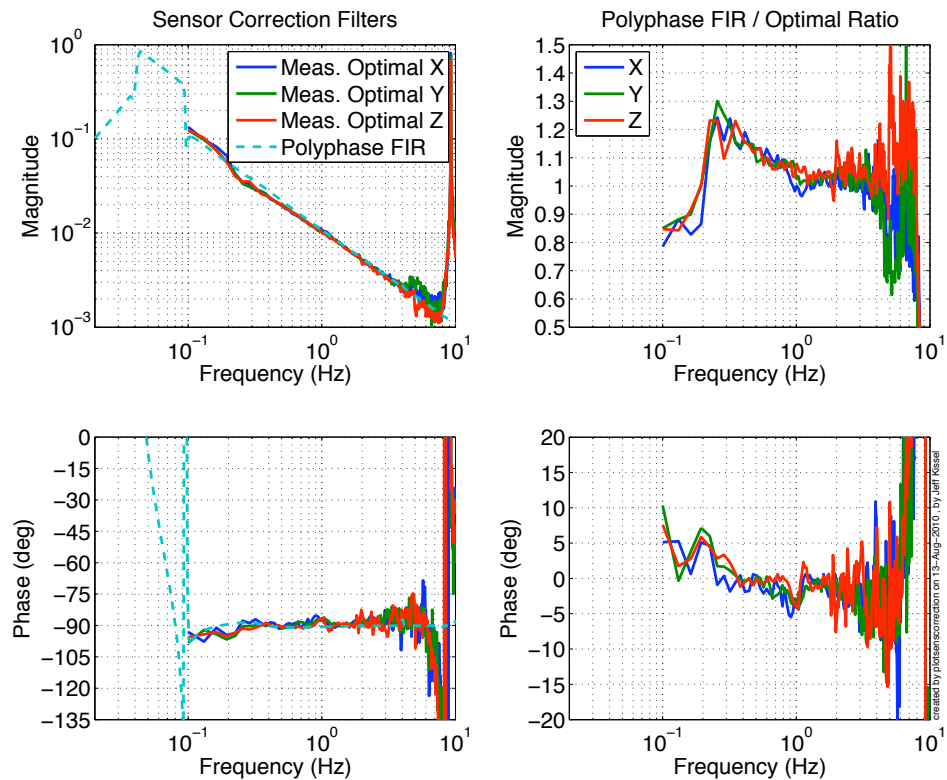


Figure 5.20: Comparison between measured optimal feed forward filter and implemented polyphase FIR filter system (in displacement units) for L1 HAM6 ISI. (Left) Ratio of geophone response to excitation via ground motion and through sensor correction path, compared against the polyphase FIR filter used for all three degrees of freedom. (Right) Ratio of polyphase FIR filter over optimal.

## 5.4 Results

Figures 5.21, 5.22, and 5.23 demonstrate the best performance of the L1 HAM ISI prototype in the X, Y, and Z direction, as measured by a witness inertial sensor on the optical table of the platform. Figures 5.24, 5.25, and 5.26 demonstrate best performance in the RX, RY, and RZ directions. Note, the H1 HAM ISI was also commissioned, and its performance is roughly the same at most frequencies (98).

In general, we see that the performance meets or surpasses Advanced LIGO requirements for the power recycling cavity at almost all frequencies for all degrees of freedom. In addition, the performance is predicted remarkably well using the simple linear model discuss in section 5.2. We also find, as a testament to the symmetric mechanical design of the platform, that similar degrees of freedom (X/Y, and RX/RY) perform almost equivalently. Below 40 mHz, the measured performance of the platform is likely larger than platform actual motion, as the inertial sensors used to measure the respective degrees of freedom are dominated by tilt (for X and Y), or incoherent sensor noise (All rotational degrees of freedom).

However, there are several narrow frequency bands in which the performance does not meet advanced LIGO requirements. Between 10 and 20 Hz, the high Q, broad features are attributed to resonances of the support structure and gullwings (99). These resonances couple into the super sensor via the displacement sensors where the roll-off of the low-pass blend is not fast enough. The roll-off is limited by the required response of its high-pass complement used to remove tilt and sensor noise in the inertial sensors (see Figure 5.11).

For the translational degrees of freedom, between 40 and 90 mHz, ground motion is amplified by the control system. This compromise is accepted in order to increase the performance of the sensor correction above 0.1 Hz. In RX and RY, the (modelled) input motion of the ground is already near or below Advanced LIGO requirements, so the little attention is paid to the performance of the active portion of the isolation system. Above 1 Hz, performance is sacrificed via a shallow roll-off of the displacement sensors such that the differential inertial sensor signal may be aggressively truncated below the blend frequency. If this sacrifice were not made, performance in X and Y would suffer below 0.5 Hz from tilt-horizontal coupling. Indeed, even with such aggressive attenuation, Figure 5.21 shows that this cross-coupling is limiting the performance.

Between 0.1 and 10 Hz, residual ground motion limits the performance for the translational degrees of freedom. As described by Eqs. 5.3 and 5.5, these limitations arise from the displacement sensor low-pass,  $F^{LP}$  and the complement to the sensor correction ( $1 - F^{FF}$ ), driven by the closed loop gain  $G/(1 - G)$ . The design of each of these components trade off between pushing the blend frequency as low as possible, setting the upper unity gain frequency high, and shaping the loop to have as much gain as possible below it, while retaining stability and keeping closed-loop gain peaking above it to a minimum. Above the gullwing resonances ( $> 20$  Hz), the passive isolation of the blade spring wire flexure system takes over. In fact, the gullwings themselves act as an additional layer of passive isolation. As such, we see a drop off in table motion into the noise floor of the measurement above 50 Hz.

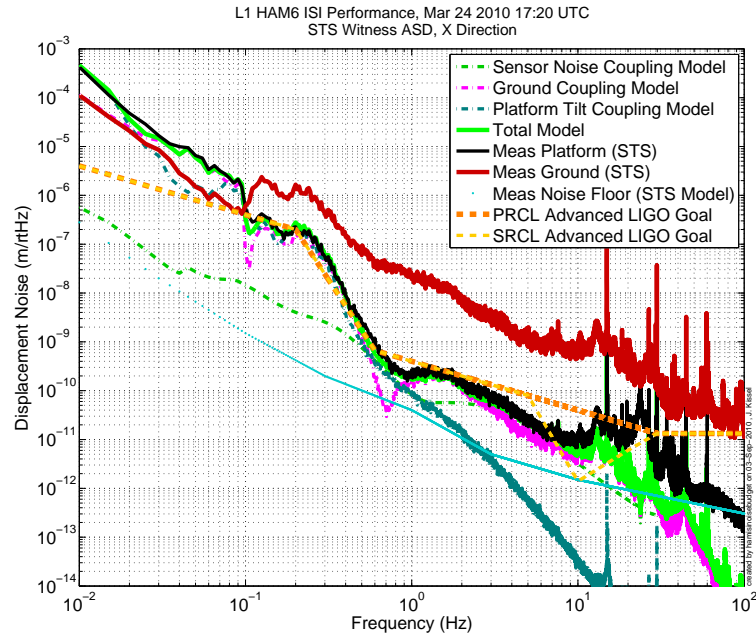


Figure 5.21: Amplitude spectral density of measured and modeled displacement noise for X degree of freedom.

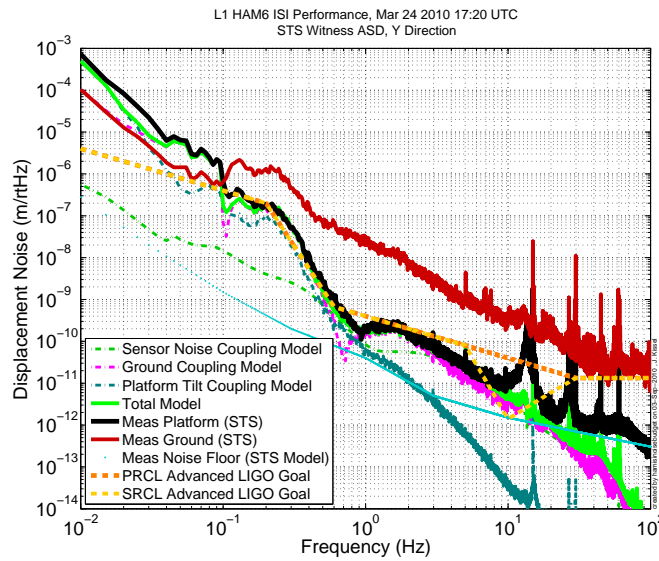


Figure 5.22: Amplitude spectral density of measured and modeled displacement noise for Y degree of freedom.

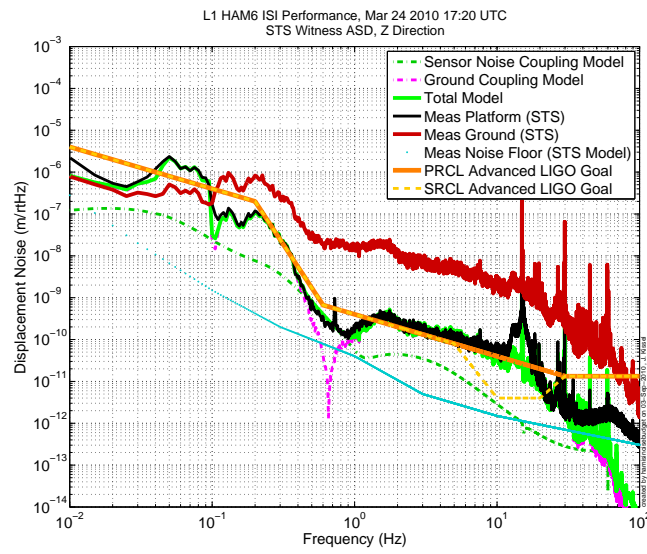


Figure 5.23: Amplitude spectral density of measured and modeled displacement noise for Z degree of freedom.

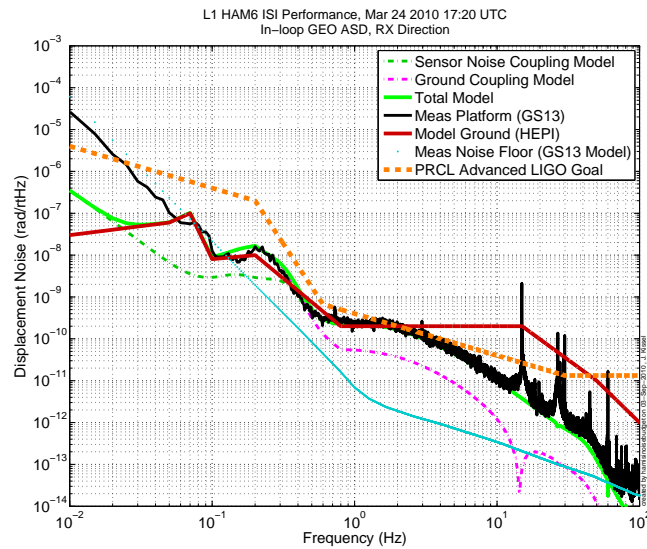


Figure 5.24: Amplitude spectral density of measured and modeled displacement noise for RX degree of freedom.

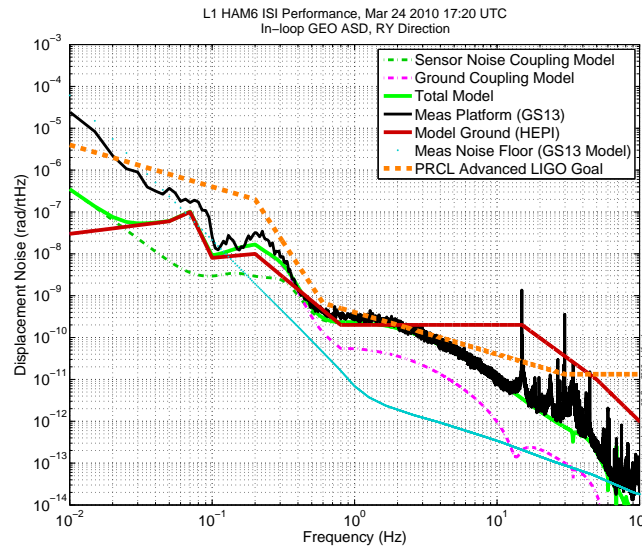


Figure 5.25: Amplitude spectral density of measured and modeled displacement noise for RY degree of freedom.

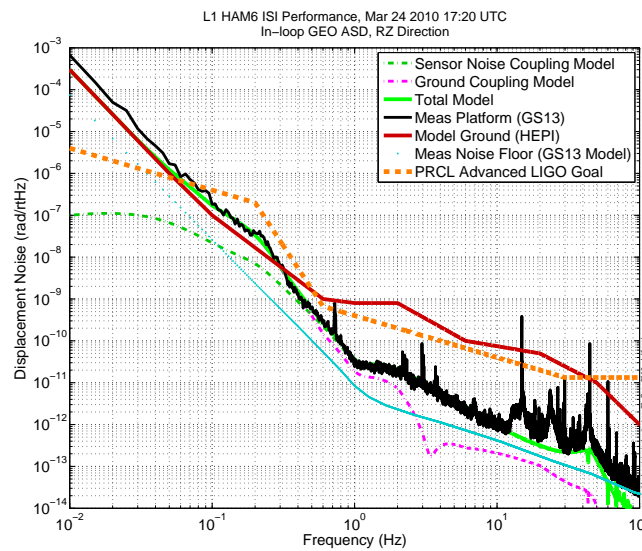


Figure 5.26: Amplitude spectral density of measured and modeled displacement noise for RZ degree of freedom.

## 5.5 The Future

Using the X and Z performance of the prototype L1 HAM ISI as  $dx_\ell$  and  $dx_Z$  in Eq. 4.3, and plugging the result into Eq. 4.1, Figure 5.27 shows the predicted coupling to the DARM displacement noise if no improvements were made to the prototypes. Unfortunately, the narrow frequency band around the gullwing resonances is exactly the region in which displacement of the HAM ISI platforms will move the the triple suspensions of the signal recycling cavity enough to surpass their thermal noise, and therefore directly limit the sensitivity to differential arm displacement. In turn, this reduces the interferometer's sensitivity to continuous wave sources with known spin down rates, and to large mass binary systems (27; 81). As such, several improvements will be made to the prototype design to improve the performance.

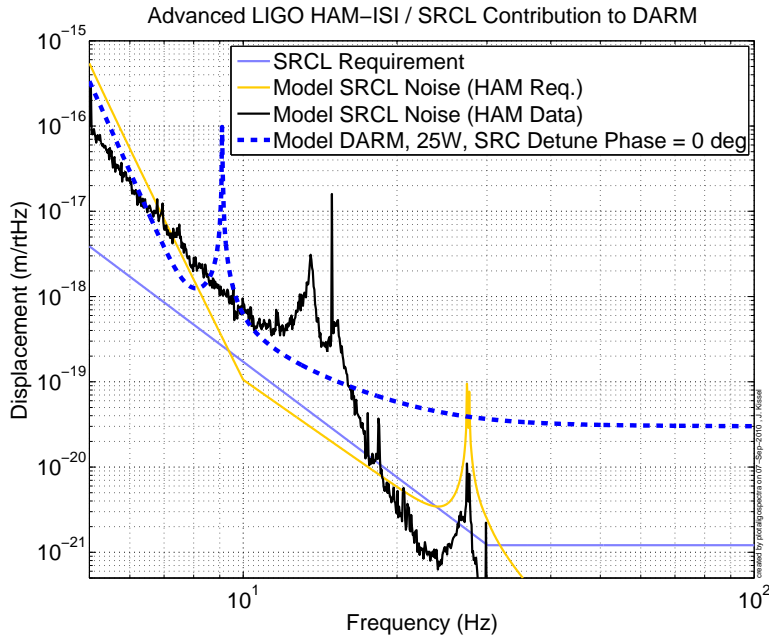


Figure 5.27: Estimated DARM displacement noise (for Mode 1a), if the prototype HAM ISI performance (black), and the SRCL target performance (gold) are used as the input motion to the Advanced LIGO SRCL cavity. The coupling is calculated by combining Eqs. 4.1 and 4.3, assuming the input parameters for Mode 1a ( $P_{arm} = 150$  W,  $T_{ITM} = 0.014$ , and  $\delta L = 10$  pm) and the vertical to horizontal coupling factor for the triple suspensions set to  $dx_\ell/dx_Z = 10^{-3}$ .

First and foremost, all HAM chambers, for every interferometer in Advanced LIGO, will be outfit with hydraulic external pre-isolation, as opposed to just HAMs 1 through 4 of the Livingston interferometer (see Section 4.3, and (2; 82)). This improvement had been established before the performance of the prototype HAM ISIs were known. As has been demonstrated in with the Initial LIGO L1, HEPI's active isolation system is expected to improve the isolation between 0.5 and 5 Hz by a factor of 10. The external isolation system will also make the support structure more compliant, reducing the frequency of the resonant

features, and the internal damping neintervalrk of the actuator HEPI will significantly reduce their Qs. Further, the angled gullwings will be replaced with stiff, straight crossbeams which recover the stiffness lost to HEPI, such that the final HEPI+support structure resonances will be higher in frequency with at least an order of magnitude reduction in Q. Figure 5.28 shows a rendering the Advanced LIGO HAM support structure, including the new crossbeams and HEPI, and Figure 5.29 compares models the support structure response to external drive in each configuration.

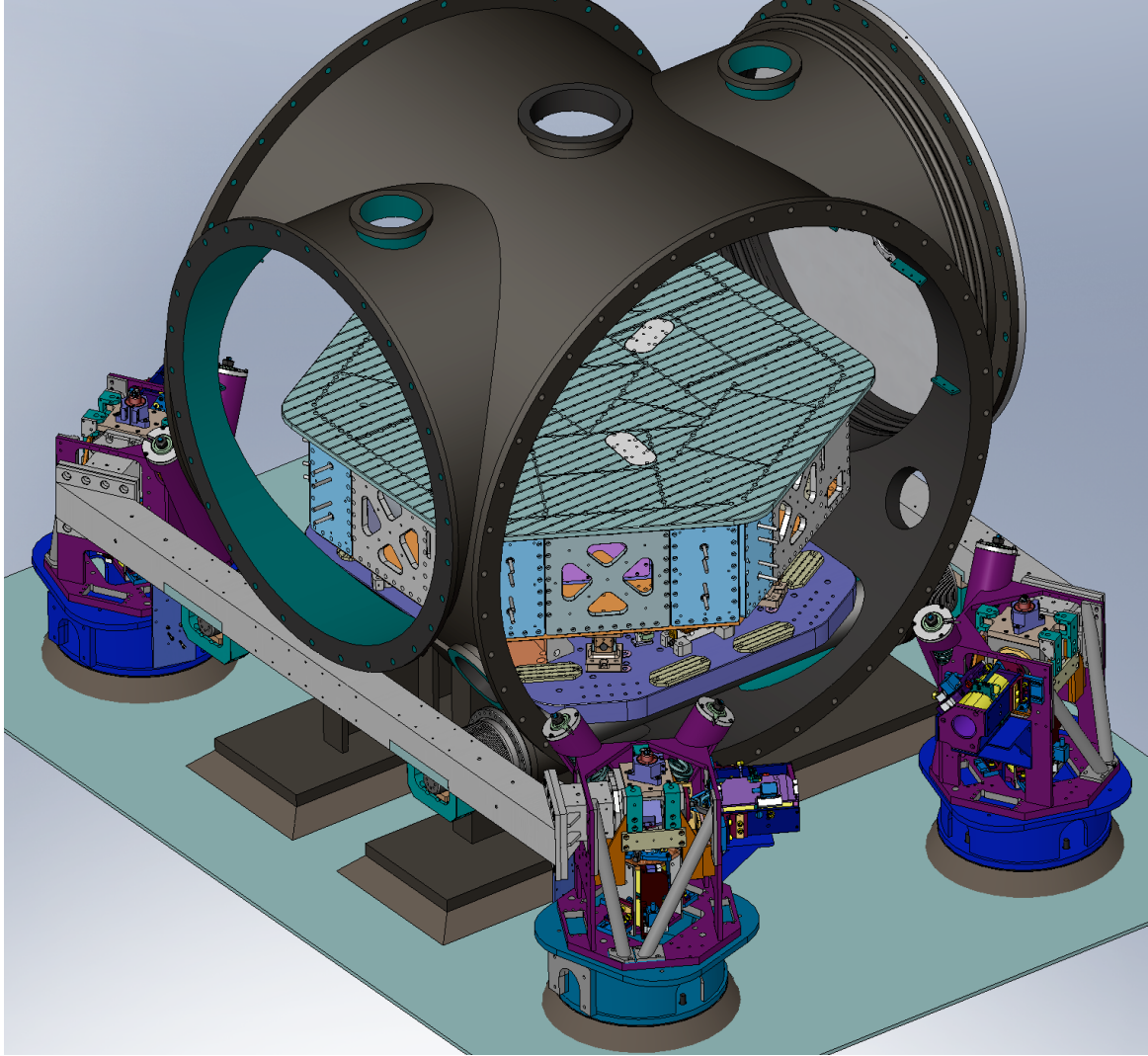


Figure 5.28: SolidWorks rendering of a fully-equipped HAM Chamber. Here, the improvements over Enhanced LIGO are mostly in the support structure, including a HAM-style HEPI system (enclosed in a purple frame) and straight stiff crossbeams (grey). Also visible is one of 6 new L4-C seismometers to be used for further active feed-forward control of the suspended stage.

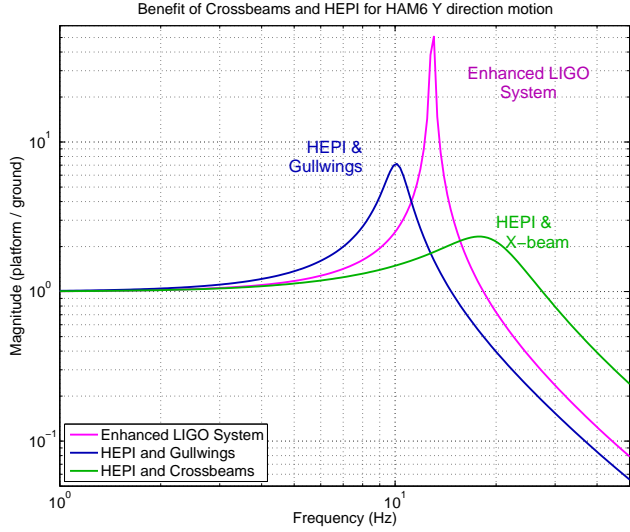


Figure 5.29: Simple model of the improvement in the support structure resonance with the planned improvements to the Advanced LIGO system, i.e. stiffer crossbeams and the addition of HEPI (16). Though feature will remain, the increase in stiffness from the crossbeam moves the fundamental frequency from roughly 13 to 20 Hz, while the addition of HEPI reduces the Q by an order of magnitude.

Second, the HAM ISIs under the signal recycling cavity will be outfitted with an additional array of six inertial sensors (Sercel L4-Cs (100)) on their support stage (see Figure 5.30). With this addition, the plan is to use hierarchical feed-forward control loops: the low-noise, low-corner frequency, ground inertial sensor will be used to correct HEPI's displacement sensors between 0.1 and 0.5 Hz, and the L4-C array will be used to correct the HAM ISI displacement sensor array between 5 and 20 Hz. This additional feed forward, pair with careful tuning of the displacement sensor blend filter should allow the SRCL HAM ISIs to meet their target performance.

Finally, several parallel paths are being followed to improve the performance in the frequency region below 100 mHz. Though the amplification of ground motion in this region was an acceptable compromise for prototype isolation systems, this may not be true for Advanced LIGO. Recall that the target displacement noise was defined such that the RMS motion of the recycling cavities was small enough for  $> 5\text{Hz}$  interferometric alignment control loops. These loops are limited by photodetector noise, which is also expected to limit the 10 - 20 Hz region of the advanced LIGO sensitivity with these bandwidths (86). If the RMS motion of the cavities is large from low frequency HAM ISI motion, then the band-width of the alignment loops must be increased, further reducing the interferometers low-frequency sensitivity to continuous wave and high-mass binary astrophysical sources.

For one, recent work with the Initial LIGO HEPI system has shown that the polyphase FIR feed-forward filter system may be improved by applying a “tweak” filter. This filter reduces the residual mismatch between the optimal filter and implemented filter (as described in section 5.3.5). Where the mismatch is typically measured between the ground inertial sensor and the sensors on the particular chamber’s isolation system, this work uses the

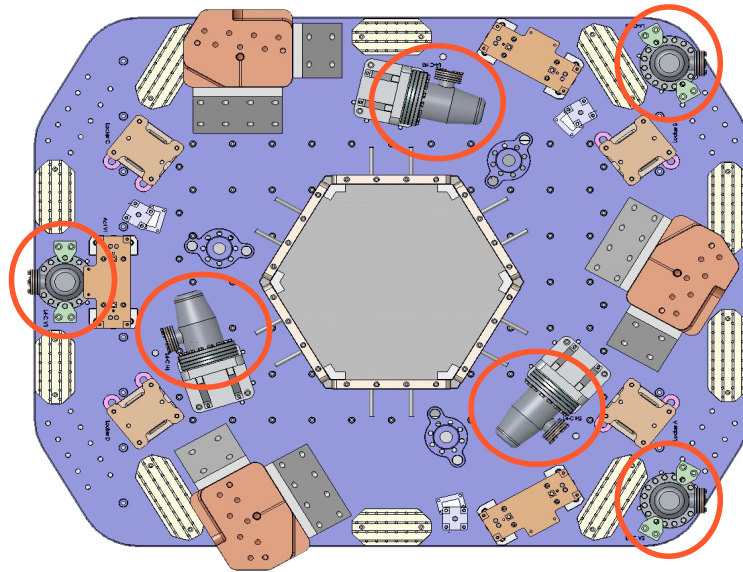


Figure 5.30: SolidWorks rendering of Advanced LIGO HAM ISI support stage, equipped with additional feed-forward L4-Cs circled in red.

multi-chamber longitudinal cavity control signals to measure the mismatch. Since it is these signals which are most relevant to interferometer performance, they serve as ideal metrics for creating the tweak filter, which after installation have been shown to improve the performance of feed-forward system by additional factors of several.

Another interferometric path being explored is referred to as a “suspension point interferometer” (SPI). This system employs high-bandwidth, auxiliary interferometers installed at the suspension point of the optics (i.e. the penultimate masses) as a ultra-sensitive inertial sensor. This sensor’s signal can then be fed-back hierarchically to prior stages to reduce residual motion. Such a system is under development which show 20 dB of isolation below 2 Hz (101). Design of a similar interferometric system, called a “lock-aquisition interferometer” (LAI), that uses the 4 km arm cavities and additional laser (albeit at a different laser wavelength) is virtually complete and is a part of the baseline for Advanced LIGO (102).

As described in Section 5.4, a limiting noise source in this band is tilt of the platform, which in turn is limited by the signal-to-noise ratio of the platforms rotational sensors: differential inertial sensor signals. Several other methods of (relatively) compact tilt-sensors are under investigation such that the feedback systems may be improved. Those under investigation include interferometric gyroscopes (103), mechanical cantilevers (104), and suspended seismometers, (105).

The prototype HAM ISIs have demonstrated they can meet Advanced LIGO requirements over a broad range of frequencies. Where they fail, plans are already in place to improve upon the performance, and with these improvements they are predicted to match, if not beat requirements for all frequencies.

## 6. Conclusions

Gravitational waves from massive, distant, astrophysical sources are predicted to cause strain in the local spacetime of order  $10^{-21}$  or less. In chapter 1, we have reviewed the mathematical framework for describing these waves, and briefly described some expected sources. From this foundation, we have shown how a Michelson interferometer is ideally suited for measuring such strains.

The Laser Interferometer Gravitational Wave Observatory, the first generation of kilometer-scale, power-recycled Fabry-Perot Michelson interferometers was described in chapter 2. A physical description of the interferometers was presented, including the optical layout, readout scheme, and seismic isolation systems. Given this design, the interferometer sensitivity was predicted to be limited by residual seismic motion of the test masses, shot noise in the sensing system, and Brownian motion of the test mass coatings and suspension system. After 5 years of development, this sensitivity was achieved during the two-year science run, known as S5.

The model and measurements techniques responsible for converting the digital differential arm loop error signal into sensitivity to physical differential displacement of the interferometer's arm cavities for S5 were described in chapter 3. Accurate reconstruction or calibration of the interferometer's degree of freedom that is most sensitive to gravitational waves is essential to data analysis. We have demonstrated that our techniques provide calibration that is accurate to within 15% and 5 degrees in magnitude and phase for all three detectors, over the course of the entire two-year S5 science run, confirmed to be absent of systematic uncertainty using several fundamentally different techniques (73). This accuracy, which is the limiting source of uncertainty for all gravitational searches on this data set, has been shown to be limited by the ability to measure the actuation control system above residual seismic motion.

In chapter 4, the next generation of the LIGO detectors has been described. The upgraded detectors, for which design is complete and construction is already well under way, are expected to have an order of magnitude better sensitivity than the first generation detectors and increase the frequency band over which gravitational wave sources are detected. The factor of 10 improvement in sensitivity, in concert with the increase of bandwidth is expected to improve the chances of gravitational wave detection beyond certainty into the realm of regular observation. Particular attention was paid to the dramatically improved seismic isolation system, from which we expect to increase the lower end of the interferometer's bandwidth from 40 Hz to 10 Hz. This improvement will open up the interferometer's sensitivity to higher mass binary astrophysical systems. Finally, we derived the requirements for the single stage active isolation system, which support the input and output optics of the new interferometer, such that their residual displacement does not limit the sensitivity in this frequency band.

In chapter 5, the design, modeling, commissioning, and results from two prototypes of this isolation system, the HAM ISI were discussed. The prototypes have demonstrated that the combination of passive and active isolation techniques were successful in achieving the Advanced LIGO displacement noise requirements at most frequencies. However, perhaps equally important, they have provided invaluable awareness of where the initial design has failed to meet target performance, such that modifications and improvements can be made and the systems final design may meet requirements at all frequencies. Indeed, improving the performance of these isolation systems has been shown to have a direct impact on the interferometer's sensitivity to gravitational waves at the lower limit of the detection frequency band.

Calibrating and improving the performance of the LIGO detectors has been shown to be a truly multi-faceted, challenging endeavor. However, the rewards of our labor will be the detection, and then routine observation of gravitational waves. With this prize comes a whole new branch of astrophysics, from which we expect truly exciting insight into the known and unknown universe.

# Bibliography

- [1] A. Abramovici, et al. LIGO: the laser interferometer gravitational wave observatory. *Science*, 17(256 5505):325, 1992.
- [2] C. Hardham. *Quiet hydraulic actuators for LIGO*. PhD thesis, Stanford University, 2005.
- [3] F. Raab, N. Solomonson, and M. Fine. Seismic isolation design requirements document. LIGO Internal Document, LIGO-T960065, 1997.
- [4] P. M. Morse and K. U. Ingard. *Theoretical Acoustics*. Princeton University Press, 1986.
- [5] D. Coyne. Test mass transmissibility. LIGO Internal Document, LIGO-T970191, 1998.
- [6] M. Sung. S5 V4 time dependent calibration coefficients. <[http://ligo.phys.lsu.edu/sung/Factors/S5/V4/S5V4\\_CalibrationFactors.html](http://ligo.phys.lsu.edu/sung/Factors/S5/V4/S5V4_CalibrationFactors.html)>, 2008.
- [7] F. Matichard. Private Communication, 2010.
- [8] R. Jones, et al. Advanced LIGO SUS ETM production monolithic assembly. LIGO Internal Document, LIGO-D1000759, 2010.
- [9] J. O'Dell, et al. Advanced LIGO quadruple suspension. LIGO Internal Document, LIGO-D0901346, 2010.
- [10] N. Robertson, et al. HAM large triple suspension (HLTS) final design document. LIGO Internal Document, LIGO-T1000012, 2010.
- [11] N. Robertson, et al. HAM small triple suspension (HSTS) final design document. LIGO Internal Document, LIGO-T0900435, 2010.
- [12] N. Roberston, B. Lantz, and J. S. Kissel. MATLAB model of the HAM small triple suspension (HSTS). LIGO Internal Document, LIGO-T090311, 2010.
- [13] N. Roberston and B. Lantz. MATLAB model of the HAM large triple suspension (HLTS). LIGO Internal Document, LIGO-T090310, 2010.
- [14] P. Fritschel, et al. Seismic isolation subsystem design requirements document. LIGO Internal Document, LIGO-E990303, 2001.
- [15] B. Lantz. Sensor noise estimates for advanced LIGO seismic isolation systems. LIGO Internal Document, T0900450, 2009.
- [16] B. Lantz. Influence of hepi and new crossbeams on the 11.4 hz beam-direction peak. Seismic Group Electronic Log Entry #1287 <<http://ligo.phys.lsu.edu:8080/SEI/1287>>, 2008.

- [17] C. Misner, K. Thorne, and J. Wheeler. *Gravitation*. W. H. Freeman Company, 1973.
- [18] R. Adler. *Introduction to general relativity*. McGraw-Hill Companies, Inc., 1975.
- [19] D. McMahon. *Relativity demystified*. McGraw-Hill Companies, Inc., 2006.
- [20] C. D. Ott, et al. Gravitational waves from axisymmetric, rotating stellar core collapse. *Astrophys. J.*, 600(2):834, 2004.
- [21] L. Bildstein. Gravitational radiation and rotation of accreting neutron stars. *Astrophys. J.*, 501(1):L89, 1998.
- [22] B. Allen. The stochastic gravity-wave background: sources and detection. *arXiv:gr-qc/9604033v3*, 1996.
- [23] B. P. Abbott, et al. An upper limit on the stochastic gravitational-wave background of cosmological origin. *Nature*, 460:990, 2009.
- [24] B. P. Abbott, et al. Einstein@home search for periodic gravitational waves in early S5 LIGO data. *Phys. Rev. D*, 80(042003), 2009.
- [25] B. Owen, et al. Gravitational waves from hot young rapidly rotating neutron stars. *Phys. Rev. D*, 58(084020), 1998.
- [26] B. P. Abbott, et al. Upper limits on gravitational wave emission from 78 radio pulsars. *Phys. Rev. D*, 76(042001), 2007.
- [27] K. Belczynski, V. Kalogera, and T. Bulik. A comprehensive study of binary compact objects as gravitational wave sources: evolutionary channels, rates, and physical properties. *Astrophys. J.*, 573(1):407, 2002.
- [28] V. Kalogera, R. Narayan, D. N. Spergel, and J. H. Taylor. The coalescence rate of double neutron star systems. *Astrophys. J.*, 556(1):340, 2001.
- [29] R. Hulse and J. Taylor. Discovery of a pulsar in a binary system. *Astrophys. J.*, 195(2):L51–L53, 1975.
- [30] J. Weisberg and J. Taylor. Relativistic binary pulsar B1913+16: thirty years of observations and analysis. *arXiv:astro-ph/0407149v1*, 2004.
- [31] M. Burgay, et al. An increased estimate of the merger rate of double neutron stars from observations of a highly relativistic system. *Nature*, 426:531, 2003.
- [32] P. Saulson. *Fundamentals of interferometric gravitational wave detectors*. World Scientific, 1994.
- [33] F. Pretorius. Evolution of binary black-hole spacetimes. *Phys. Rev. D*, 95(121101), 2005.
- [34] T. Baumgarte. Learning about compact binary merger: the interplay between numerical relativity and gravitational-wave astronomy. *Phys. Rev. D*, 77(084009), 2008.

- [35] J. G. Baker, et al. Consistency of post-newtonian waveforms with numerical relativity. *Phys. Rev. Lett.*, 99(181101), 2007.
- [36] B. P. Abbott, et al. Predictions for the rates of compact binary coalescences observable by ground-based gravitational-wave detectors. *arXiv:1003.2480v2*, 2010.
- [37] H. Dimmelmeier. Gravitational wave burst signal from core collapse of rotating stars. *Phys. Rev. D*, 78(064056), 2008.
- [38] S. W. Hawking and W. Israel. *Three hundred years of gravitation*. Cambridge University Press, 1987.
- [39] F. A. E. Pirani. On the physical significance of the riemann tensor. *Acta Phys. Pol.*, 15:389, 1956.
- [40] M.E. Gertsenshtein and V.I. Pustovoit. On the detection of low-frequency gravitational waves. *JETP*, 16:433, 1963.
- [41] R. Forward, G. Moss, and L. Miller. Photon-noise-limit laser transducer for gravitational antenna. *Appl. Opt.*, 10:2495, 1971.
- [42] R. Weiss. Electromagnetically coupled broadband gravitational wave antenna. *Quarterly Progress Report of the Research Laboratory of Electronics of the Massachusetts Institute of Technology*, 105:54, 1972.
- [43] R. Drever, et al. A gravity-wave detector using optical cavity sensing. In E. Schmutzler, editor, *Proceedings of the Ninth International Conference on General Relativity and Gravitation*, page 265, Jena, Germany, 1983.
- [44] E. Ponslet. Design of vacuum compatible damped metal springs for passive vibration isolation of the ligo detectors. LIGO Internal Document, LIGO-T960212, 1996.
- [45] R. Drever, et al. Laser phase and frequency stabilization using an optical resonator. *App. Phys. B*, 31(2):97, 1983.
- [46] M. Regehr, F. Raab, and S. Whitcomb. Demonstration of a power recycled Michelson interferometer with Fabry-Perot arms by frontal modulation. *Opt. Lett*, 20(13):1507, 1995.
- [47] D. G. Blair. *The detection of gravitational waves*. Cambridge University Press, 1991.
- [48] B. P. Abbott, et al. LIGO: The laser interferometer gravitational wave observatory. *Rep. Prog. Phys.*, 72(7):6901, 2009.
- [49] P. Fritschel, et al. Readout and control of a power-recycled interferometric gravitational wave antenna. *Appl. Opt.*, 40(28):4988, 2001.
- [50] G. Gonzalez. Suspension thermal noise in the LIGO gravitational wave detector. *Class. Quantum Grav.*, 17(21):4409, 2000.
- [51] G. Harry, et al. Thermal noise from optical coatings in gravitational wave detectors. *Class. Quantum Grav.*, 19(5):897, 2002.

- [52] B. P. Abbott, et al. Sensitivity to gravitational waves from compact binary coalescences achieved during LIGO's fifth and VIRGO's first science run. LIGO Internal Document, T0900499, 2009.
- [53] J. Abadie, et al. Calibration of the LIGO gravitational wave detectors in the fifth science run. *Nucl. Instr. and Meth. A.*, (in prep, doi:10.1016/j.nima.2010.07.089), 2010.
- [54] X. Siemens, et al. Making  $h(t)$  for LIGO. *Class. Quantum Grav.*, 21(20):S1723, 2004.
- [55] K. Kawabe, B. O'Reilly, and X. Siemens. Summary of S5 calibration models and uncertainties. LIGO Internal Document, LIGO-T1000227, 2010.
- [56] M. Rakhmanov, J. D. Romano, and J. T. Whelan. High-frequency corrections to the detector response and their effect on searches for gravitational waves. *Class. Quantum Grav.*, 25(18):4017, 2008.
- [57] W. G. Anderson, P. R. Brady, J. D. E. Creighton, and É. Flanagan. Excess power statistic for detection of burst sources of gravitational radiation. *Phys. Rev. D*, 63(4):2003, 2001.
- [58] W. G. Anderson, P. R. Brady, J. D. E. Creighton, K. Riles, and J. T. Whelan. Beam pattern response functions and times of arrival for earthbound interferometer. LIGO Internal Document, LIGO-T010110, 2001.
- [59] M. Rakhmanov, Savage Jr. R. L., D. Reitze, and D. Tanner. Dynamic resonance of light in fabry-perot cavities. *Phys. Lett. A*, 305(5):239, 2002.
- [60] D. Sigg. Strain calibration of LIGO. LIGO Internal Document, LIGO-T090101, 1997.
- [61] D. Sigg. Frequency response of the LIGO interferometer. LIGO Internal Document, LIGO-T970084, 1997.
- [62] L. Schnupp. Contribution to European Collaboration Meeting on Interferometric Detection of Gravitational Waves, 1988.
- [63] K. Koechner. *Solid-state laser engineering*. Springer-Verlag, 3rd edition, 1992.
- [64] S. Singh, R. G. Smith, and L. G. Van Uitert. Stimulated-emission cross section and fluorescent quantum efficiency of  $\text{Nd}^{3+}$  in yttrium aluminum garnet at room temperature. *Phys. Rev. D*, 10(6):2566, 1974.
- [65] M. Landry. LIGO test mass mechanical resonances. LIGO Internal Document, LIGO-T050089, 2005.
- [66] A. V. Oppenheim and R. W. Schafer. *Digital signal processing*. Prentice-Hall, 1975.
- [67] R. Christi. *Modern digital signal processing*. Brooks/Cole, 1992.
- [68] Y. Aso, et al. Accurate measurement of the time delay in the response of the LIGO gravitational wave detectors. *Class. Quantum Grav.*, 26(5):5010, 2009.

- [69] M. Evans, et al. Lock acquisition of a gravitational wave interferometer. *Opt. Lett.*, 27(8):598, 2002.
- [70] B. P. Abbott, et al. Search for high-frequency gravitational wave bursts in the first calendar year of LIGO's fifth science run. *Phys. Rev. D*, 80(102002), 2009.
- [71] E. Goetz and R. L. Savage Jr. Calibration of the LIGO displacement actuators via laser frequency modulation. *arXiv:1005.3746v1*, 2009.
- [72] E. Goetz, et al. Precise calibration of LIGO test mass actuators using photon radiation pressure. *Class. Quantum Grav.*, 26(24):5011, 2009.
- [73] E. Goetz, et al. Accurate calibration of test mass displacement in the LIGO interferometers. *Class. Quantum Grav.*, 27(8):4024, 2010.
- [74] R. Adhikari, G. Gonzalez, M. Landry, and B. O'Reilly. Calibration of the LIGO detectors for the first LIGO science run. *Class. Quantum Grav.*, 20(17):S903, 2003.
- [75] L. Lindblom. Optimal calibration accuracy for gravitational wave detectors. *Phys. Rev. D*, 80(04):2005, 2009.
- [76] G. Harry for the LSC. Advanced LIGO: the next generation of gravitational wave detectors. *Class. Quantum Grav.*, 27(8):4006, 2009.
- [77] P. Fritschel, et al. Second generation instruments for the laser interferometer gravitational wave observatory (LIGO). In M. Cruise and P. Saulson, editors, *Proceedings of SPIE*, volume 4856, page 282, Bellingham, WA, 2003.
- [78] R. Adhikari. *Sensitivity and noise analysis of 4 km laser interferometric gravitational wave antennae*. PhD thesis, California Institute of Technology, 2004.
- [79] A. Buonanno, Y. Chen, and N. Mavalvala. Quantum noise in laser-interferometer gravitational-wave detectors with a heterodyne readout scheme. *Phys. Rev. D*, 67(12):2005, 2003.
- [80] G. Harry, et al. Titania-doped tantalum / silica coatings for gravitational wave detection. *Class. Quantum Grav.*, 24(2):405, 2007.
- [81] R. N. Manchester, et al. The australia telescope national facility pulsar catalogue. *Astrophys. J.*, 129(4):1993, 2005.
- [82] S. Wen. *Improved seismic isolation for the Laser Interferometer Gravitational Wave Observatory with a hydraulic external pre-isolator system*. PhD thesis, Louisiana State University, 2009.
- [83] N. Robertson, et al. Seismic isolation and suspension systems for advanced LIGO. In J. Hough and G. H. Sanders, editors, *Proceedings of SPIE*, volume 5500, page 81, Bellingham, WA, 2003.
- [84] F. Maticichard, et al. Prototyping, testing, and performance of the two-stage seismic isolation system for advanced LIGO gravitational wave detectors. In *Proceedings of ASPE*, page 75, Massachusetts Institute of Technology, Cambridge, MA, 2010.

- [85] P. Fritschel. HAM seismic isolation requirements. LIGO Internal Document, LIGO-T060075, 2006.
- [86] L. Barsotti and M. Evans. Modeling of alignment sensing and control for advanced LIGO. LIGO Internal Document, LIGO-T0900511, 2010.
- [87] M. Evans and P. Fritschel. Displacement noise requirements in advanced LIGO triple suspensions. LIGO Internal Document, LIGO-T080192, 2008.
- [88] B. Lantz. Revised HAM-ISI performance targets for advanced LIGO signal recycling cavity chambers. LIGO Internal Document, T1000216, 2010.
- [89] High Precision Devices. <<http://www.hpd-online.com/>>.
- [90] W. Hua, et al. Low-frequency active vibration isolation for advanced LIGO. In J. Hough and G. H. Sanders, editors, *Proceedings of SPIE*, volume 5500, page 194, Bellingham, WA, 2004.
- [91] R. Abbott, et al. Seismic isolation enhancements for initial and advanced LIGO. *Class. Quantum Grav.*, 21(5):S915, 2004.
- [92] QinetiQ, North America. <<http://www.qinetiq-na.com/index.htm>>.
- [93] MicroSense, LLC. <<http://www.microsense.net/>>.
- [94] GeoTech, Inc. <<http://www.geoinstr.com/s-13.htm>>.
- [95] M. Evans. Digital filter noise. LIGO Internal Document, LIGO-G0900928, 2009.
- [96] W. Hua. *Low frequency vibration isolation and alignment system for advanced LIGO*. PhD thesis, Stanford University, 2005.
- [97] W. Hua, et al. Polyphase FIR complementary filters for control systems. In *Proceedings of ASPE*, volume 32, page 75, Massachusetts Institute of Technology, Cambridge, MA, 2004.
- [98] J. S. Kissel, C. Gray, and R. Mittleman. H1 HAM6 ISI eLIGO final performance measurements (March 13 2009). LIGO Internal Document, LIGO-T1000483, 2009.
- [99] J. S. Kissel. eLIGO HAM6 ISI plant comparisons. LIGO Internal Document, LIGO-T080274, 2009.
- [100] Sercel. <<ftp://ftp.sercel.com/pdf/brochures/Analog\%20Seismic\%20Sensors\%20Specifications.pdf>>.
- [101] Y. Aso, et al. Active vibration isolation using a suspension point interferometer. *J. Phys: Conf. Ser.*, 32:451, 2006.
- [102] A. F. Brooks, D. Yeaton-Massey, and R. Adhikari. Auxiliary locking system for the advanced LIGO gravitational wave interferometer. *Frontiers in Optics, OSA Technical Digest*, JWC20, 2009.
- [103] A. Heptonstall, et al. Passive ring laser gyro for rotation sensing. LIGO Internal Document, LIGO-T0900609, 2009.

- [104] R. DeSalvo. LIGO knife-edge tiltmeter development presentation 2010. LIGO Internal Document, LIGO-G1000704, 2010.
- [105] M. Evans and F. Matichard. Tilt-free inertial sensing, 2010.
- [106] J. Bendat and A. Piersol. *Random data: analysis & measurement procedures*. Wiley-Interscience, 3rd edition, 2000.
- [107] L. Rolland. VIRGO actuator gain calibration: methods and results. Period September 2006 to April 2007. VIRGO Internal Document, VIR-0005A-07, 2007.

# Appendix A: LIGO Amplitude Spectral Density

A common figure of merit used to measure the frequency content of a given signal in LIGO is the “one-sided amplitude spectral density” (ASD). The ASD is derived from standard frequency domain analysis (106), but we review its derivation here. We begin by defining the cross-correlation function between two signals,

$$S_{xy}(f, T) = \frac{1}{T} \tilde{X}^*(f, T) \tilde{Y}(f, T), \quad (6.1)$$

where  $\tilde{X}(f, T)$  is the Fourier transform of a given signal  $x(t, T)$  measured over a time period  $T$ . We assume a real time series, or

$$x^*(t) = x(t) \quad \text{or} \quad \tilde{X}^*(f) = \tilde{X}(-f), \quad (6.2)$$

such that the Fourier transform takes the form

$$\tilde{X}(f, T) = \frac{\sqrt{2}}{\sqrt{2\pi}} \int_0^T x(t) e^{-2\pi i f t} dt, \quad (6.3)$$

i.e. the Fourier transform is “one-sided.”

We reduce the cross-correlation function  $S_{xy}(f, T)$  to a function of frequency only, by assuming our measurement time period  $T$  is large compared to the periods of signal oscillation  $1/f$ ,

$$S_{xy}(f) = \lim_{T \rightarrow \infty} (\mathbb{E}[S_{xy}(f, T)]), \quad (6.4)$$

where the operator “ $\mathbb{E}[x]$ ” is the ensemble average,

$$\mathbb{E}[x] = \frac{1}{N} \sum_{i=1}^N x_i. \quad (6.5)$$

We define the power spectral density  $S_{xx}(f)$ , as the signal cross-correlated with itself (called “auto-correlation”), as

$$S_{xx}(f) = \lim_{T \rightarrow \infty} \left( \frac{1}{N} \sum_{i=1}^N \frac{1}{T_i} \tilde{X}^*(f, T_i) \tilde{X}(f, T_i) \right). \quad (6.6)$$

In practice, we do not have an infinite time series so we divide the total time series into sufficiently long intervals of equal length ( $T_i = T$ ), take the ensemble average of all intervals, and ignore the limit:

$$S_{xx}(f) = \frac{1}{NT} \sum_{i=1}^N \tilde{X}_i^*(f, T) \tilde{X}_i(f, T). \quad (6.7)$$

Finally, we form the ASD from the square root of the power in each average,

$$A_{xx}(f) = \frac{1}{NT} \sum_{i=1}^N \sqrt{\tilde{X}_i^*(f, T) \tilde{X}_i(f, T)}. \quad (6.8)$$

All information stored in the time-series can be recovered from the power spectrum, by integrating over frequency in a band-limited fashion (“Mean Square,” *MS*), and taking the square root (“Root Mean Square,” *RMS*),

$$x_{MS}(t) = \frac{1}{NT} \sum_{i=1}^N \int_{f1}^{f2} \tilde{X}_i^*(f, T) \tilde{X}_i(f, T) df \quad (6.9)$$

$$x_{RMS}(t) = \sqrt{\frac{1}{NT} \sum_{i=1}^N \int_{f1}^{f2} \tilde{X}_i^*(f, T) \tilde{X}_i(f, T) df}, \quad (6.10)$$

which can be compared with the original time series, in a similar fashion,

$$x_{RMS}(t) = \sqrt{\frac{1}{NT} \sum_{i=1}^N \int_0^T x_i^*(t) x_i(t) dt}. \quad (6.11)$$

Note, for a proper comparison, if the integral in Eq. 6.9 and 6.10 are limited to frequencies  $f_1 < f < f_2$ , then a band-pass filter over the same frequency range should be applied to  $x_i(t)$  before comparison.

## Appendix B: The Free-Swinging Michelson Techniques<sup>4</sup>

The technique used for determining the actuation coefficients,  $\mathcal{K}_A^{x,y}$ , for the fifth science run is known as the “free-swinging Michelson” technique. This technique uses the interferometer’s well-known Nd:YAG laser wavelength ( $\lambda = 1064.1 \pm 0.1$  nm, (63; 64)) as the calibrated length reference while using the test mass coil actuators to cause a change in length of simple interferometer configurations. The technique may be used in two similar methods: the “Simple Michelson” and “Asymmetric Michelson” methods.

The Simple Michelson method is composed of two steps. The first step determines the actuation scaling coefficient for the input test masses  $\mathcal{K}_i$  with the interferometer in a non-standard configuration called a frequency-modulated simple Michelson (see left panel of Figure 6.1). The second step determines the end test mass actuation coefficient,  $\mathcal{K}_A$ , from the input test coefficient,  $\mathcal{K}_i$ , and transfer function measurements of the input and end test masses of a single Fabry Perot arm cavity (see right panel of Figure 6.1). The Asymmetric Michelson determines  $\mathcal{K}_A$  directly using the configuration shown in Figure 6.4. Both free-swinging Michelson methods are described below.

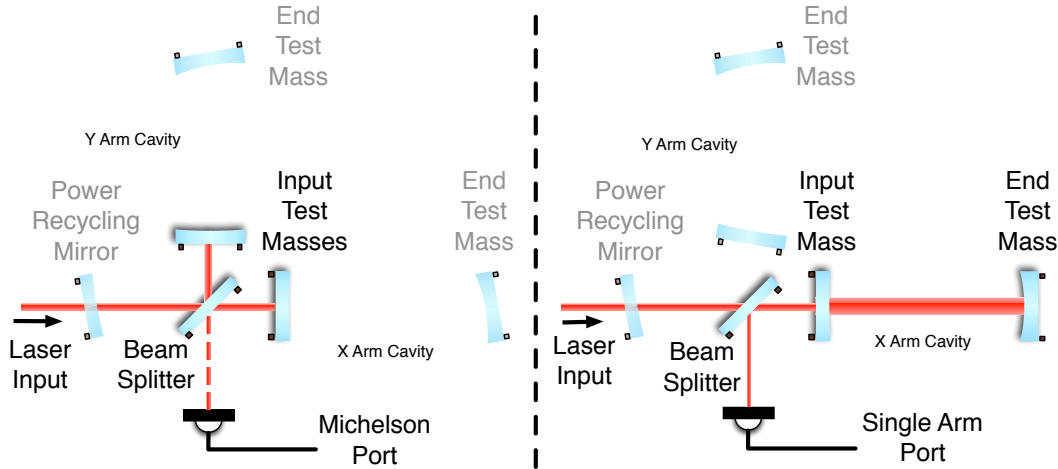


Figure 6.1: Interferometer configurations used during the simple Michelson method of measuring the actuation scaling coefficient. Left: The simple Michelson configuration, where the power recycling mirror and end test masses are misaligned. Right: The single arm configuration, with the power recycling mirror and the opposing arm’s input and end test mass are misaligned.

---

<sup>4</sup>Much of the material presented in this Appendix has been published in (53) and is reproduced here with expressed permission from Dr. William Barletta, Coordinating Senior Editor of Nuclear Instruments and Methods A (see Appendix E).

## Simple Michelson Method

The Pound-Drever Hall error signal at the anti-symmetric port,  $q_{AS}$ , for a frequency-modulated simple Michelson interferometer is

$$q_{AS} = \frac{1}{2} A_{pp} \sin\left(\frac{4\pi}{\lambda} \Delta\ell\right), \quad (6.12)$$

where  $A_{pp}$  is the peak-to-peak amplitude of the signal (proportional to the input power, the product of Bessel functions of modulation strength, and the transmission of the sidebands into the antisymmetric port from the Michelson asymmetry),  $\lambda = 1064$  nm is the wavelength of the input laser light, and  $\Delta\ell = \ell_x - \ell_y$  is the differential arm length of the Michelson.  $A_{pp}$  is measured by aligning the simple Michelson and recording the  $q_{AS}$  time series as it is left uncontrolled. In this configuration, external noise sources (e.g. residual ground motion) are large enough to cause the Michelson to sweep through many interference fringes.

For the simple Michelson, when  $\Delta\ell/\lambda \ll 1$ ,

$$q_{AS} \approx k\Delta\ell \quad (6.13)$$

with the simple Michelson's "optical gain,"

$$k = (2\pi/\lambda)A_{pp}, \quad (6.14)$$

which has units of digital signal counts per meters of input test mass motion. After a measurement of  $A_{pp}$  is obtained, we control the optics using their coil actuators, forcing the Michelson into the linear regime where Eq. 6.14 is valid.

The actuation function of the suspended input test masses can be approximated by the center-of-mass force-to-displacement transfer function,  $P_{cm}^i$  with a scaling coefficient,  $\mathcal{K}_i$ . We obtain a measurement of  $\mathcal{K}_i$  for a given input test mass by introducing a digital excitation  $exc_i$  into the control loop that is much larger than residual external noise sources. The excitation is performed over many frequencies in the gravitational wave band; assuming the model is complete, the coefficient should be frequency-independent across the band. We obtain a solution for the digital excitation counts on the input test mass in terms of meters of resulting motion as measured by  $q_{AS}$  (normalized by the pendulum response  $P_{cm}^i$ ),

$$\mathcal{K}_i = \left( \frac{q_{AS}}{exc_i} \right) \left( \frac{1 + G_{SM}}{k} \right) \left( \frac{1}{P_{cm}^i} \right). \quad (6.15)$$

The first term is the measured response of the Michelson during the single input test mass excitation. The second term contains the open loop transfer function  $G_{SM}$  of the simple Michelson control loop (measured just prior to measuring the response to excitation) and the quantity  $k$  is as defined in Eq. 6.14. We take the median of  $\mathcal{K}_i$  (denoted with "bra" "kets,"  $\langle \rangle$ ), over the measured frequency points to remove measurement outliers and residual frequency dependence (or time dependence of  $k$ , as discussed in §3.3). Figure 6.2 shows an example measurement of  $\mathcal{K}_i$  for each input test mass in H2.

We then configure the interferometer to form a single Fabry-Perot cavity composed of one arm of the interferometer, and control it such that the cavity is under resonance (see Figure 6.1). In this configuration, the response of the single arm cavity (now recorded by the in-phase demodulated output  $i_{AS}$ , see (61) for details) to sequential length excitations of the input test mass,  $exc_i$ , and end test mass,  $exc_e$ , are measured. The ratio,  $\mathcal{R}_{ie}$  of these

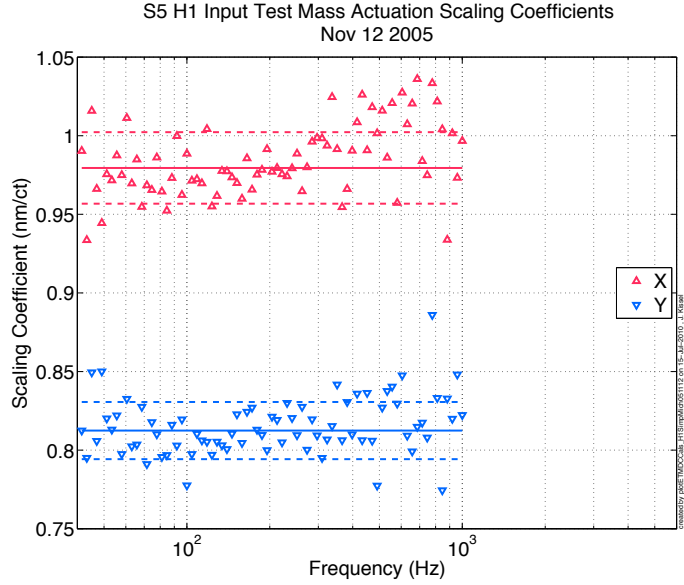


Figure 6.2: Example actuation scaling coefficients for the H2 input test masses  $\mathcal{K}_i^{x,y}$ , measured using the simple Michelson method. Top:  $\mathcal{K}_i$  as a function of frequency for the X and Y input test mass. Solid lines indicate the median of the data points  $\langle \mathcal{K}_i \rangle$ , dashed lines indicate  $1\sigma$  error bars (the standard deviation of all frequency points).

two transfer functions can then be used to write the actuation coefficient for the end test masses as

$$\mathcal{K}_A = \mathcal{R}_{ie} \left( \frac{P_{cm}^i}{P_{cm}} \right) \langle \mathcal{K}_i \rangle = \left( \frac{i_{AS}}{exc_e} \right) \left( \frac{exc_i}{i_{AS}} \right) \left( \frac{P_{cm}^i}{P_{cm}} \right) \langle \mathcal{K}_i \rangle, \quad (6.16)$$

where  $\mathcal{K}_A$  has units of test mass motion in meters (as measured by  $q_{AS}$ ) per count of digital excitation. Figure 6.3 shows a measurement of  $\mathcal{K}_A$  for each test mass in H1. As in the first step, the median of the frequency points measured in  $\mathcal{K}_A$  is used to form a single value for the coefficient over the measurement bands.

## Asymmetric Michelson Method

During the latter part of the science run, a more direct approach of determining the actuation coefficient  $\mathcal{K}_A$  was taken, using the “asymmetric Michelson technique.” This method is similar in principle to the simple Michelson version of the free-swinging Michelson technique, however, we configure the interferometer as shown in Figure 6.4. In this method the response of the end test mass is measured directly and

$$\mathcal{K}_A = \left( \frac{q_{AS}}{exc_e} \right) \left( \frac{1 + G_{AM}}{k} \right) \left( \frac{1}{P_{cm}} \right). \quad (6.17)$$

Figure 6.5 shows an example result for L1.

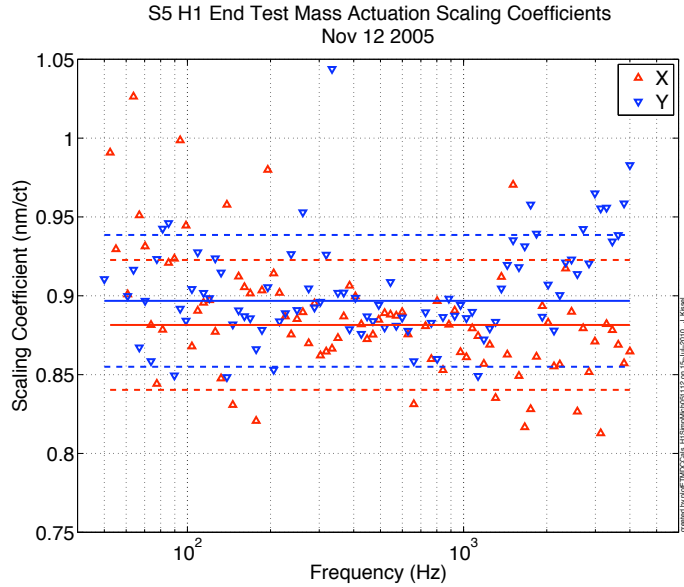


Figure 6.3: Example actuation scaling coefficients for the H1 end test masses  $\mathcal{K}_A^{x,y}(f)$ , measured using the simple Michelson method. Top:  $\mathcal{K}_A$  as a function of frequency for the X and Y end test mass. Solid lines indicate the median of the data points  $\langle \mathcal{K}_A^{x,y} \rangle$ , dashed lines indicate  $1\sigma$  error bars (see §3.3 for description).

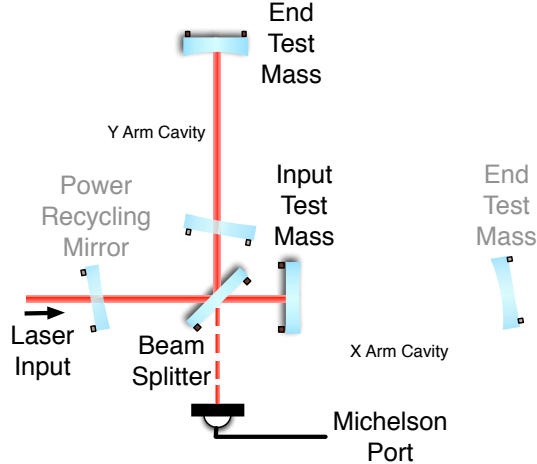


Figure 6.4: “Asymmetric Michelson” configuration of the interferometer. With the power recycling mirror misaligned, an input test mass and opposing end test mass are aligned.

The quantity  $k$  may vary slowly over the measurement period due to input laser power fluctuations, interferometer alignment, etc. The asymmetric Michelson is particularly sensitive to these variations as round trip power loss is large. For this method, we employ a more

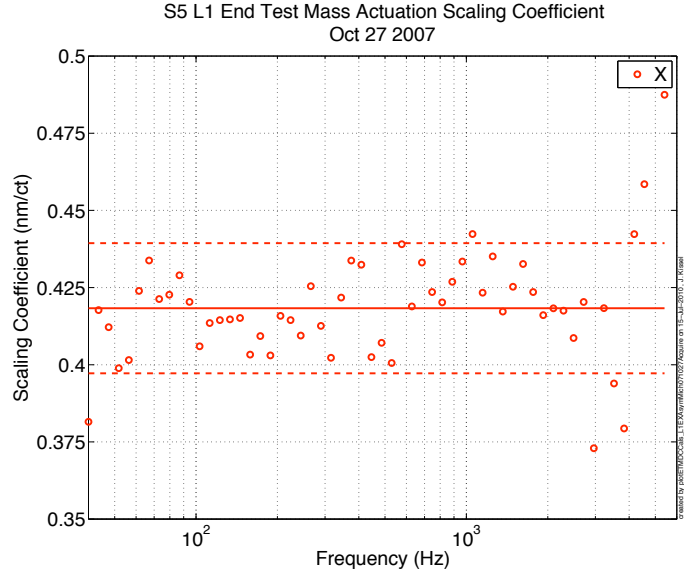


Figure 6.5: Example actuation scaling coefficient for the L1 X arm end test mass  $\mathcal{K}_A^x$ , measured using the asymmetric Michelson method. Top:  $\mathcal{K}_A^x$  as a function of frequency. Solid lines indicate the median of the data points  $\langle \mathcal{K}_A^x \rangle$ , dashed lines indicate  $1\sigma$  error bars. Bottom: Histograms for  $\mathcal{K}_A^x$ , with the median shown in solid pink, and error bars in dashed pink.

sophisticated technique for determining the amplitude  $A_{pp}$ , developed originally by Rolland et al (107). A plot of  $q_{AS}$  versus the total power incident on the photodiodes should be an ellipse whose semi-minor axis is  $A_{pp}/2$ . We obtain a fit to this ellipse and extract  $A_{pp}$  with a quantifiable statistical error.

## Results

Using the above methods, the actuation coefficient is measured many times for each optic in each interferometer over the course of the science run, and the mean of all measurements' medians in magnitude is used as the actuation scaling coefficient for all model epochs. Only the magnitude is used, as the phase of each measurement is consistent with zero. Figure 6.7 shows the representative median and estimated uncertainty for each of these measurements. Table 6.1 summarizes the actuation coefficients used in the actuation model,  $\langle \mathcal{K}_A \rangle$  for the three interferometers in the fifth science run, using either simple Michelson or asymmetric Michelson techniques, with statistical uncertainty as described in §3.2.1.

Each simple Michelson measurement of a given optic's coefficient is assigned magnitude and phase uncertainty,

$$\left( \frac{\sigma_{|\mathcal{K}_A|}}{|\mathcal{K}_A|} \right)^2 = \left[ \frac{\text{std}(|\mathcal{K}_i|)}{\langle |\mathcal{K}_i| \rangle} \right]^2 + \left[ \frac{1}{\langle |\mathcal{R}_{ie}| \rangle} \frac{\text{std}(|\mathcal{R}_{ie}|)}{\sqrt{N}} \right]^2 \quad (6.18)$$

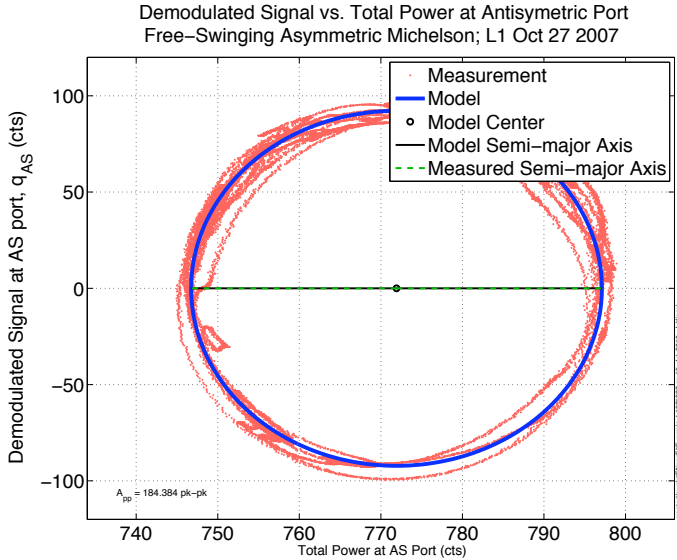


Figure 6.6: An example ellipse produced by photodiode demodulated signal  $q_{AS}$  versus total power, and corresponding fit to the ellipse used to determine  $A_{pp}$  in asymmetric Michelson method.

Table 6.1: Summary of the actuation scaling coefficients measured during S5. These single numbers are formed by the mean of each measurement's median  $\langle \mathcal{K}_A \rangle_j$  (6 for each end test mass in H1, 5 in H2, and 14 and 15 for the X and Y test masses, respectively in L1). Only statistical uncertainty is reported here; systematic uncertainty is folded into the total uncertainty of the actuation function.

	$\mathcal{K}_A^x$ (nm/ct)	$\mathcal{K}_A^y$ (nm/ct)
H1	$0.847 \pm 0.024$	$0.871 \pm 0.019$
H2	$0.934 \pm 0.022$	$0.958 \pm 0.034$
L1	$0.434 \pm 0.039$	$0.415 \pm 0.034$

$$\sigma_{\phi_{\mathcal{K}_A}}^2 = \text{std}(\phi_{\mathcal{K}_i})^2 + \left[ \frac{\text{std}(\phi_{\mathcal{R}_{ie}})}{\sqrt{N}} \right]^2 \quad (6.19)$$

and asymmetric Michelson measurement is assigned magnitude and phase uncertainty

$$\left( \frac{\sigma_{|\mathcal{K}_A|}}{|\mathcal{K}_A|} \right)^2 = \left[ \frac{\text{std}(|\mathcal{K}_A|)}{\langle |\mathcal{K}_A| \rangle} \right]^2 \quad (6.20)$$

$$\sigma_{\phi_{\mathcal{K}_A}}^2 = \text{std}(\phi_{\mathcal{K}_A})^2 \quad (6.21)$$

In simple Michelson technique, measurements of  $\mathcal{K}_i$  were found to be inconsistent with a Gaussian distribution across the frequency band. We therefore estimate the uncertainty in

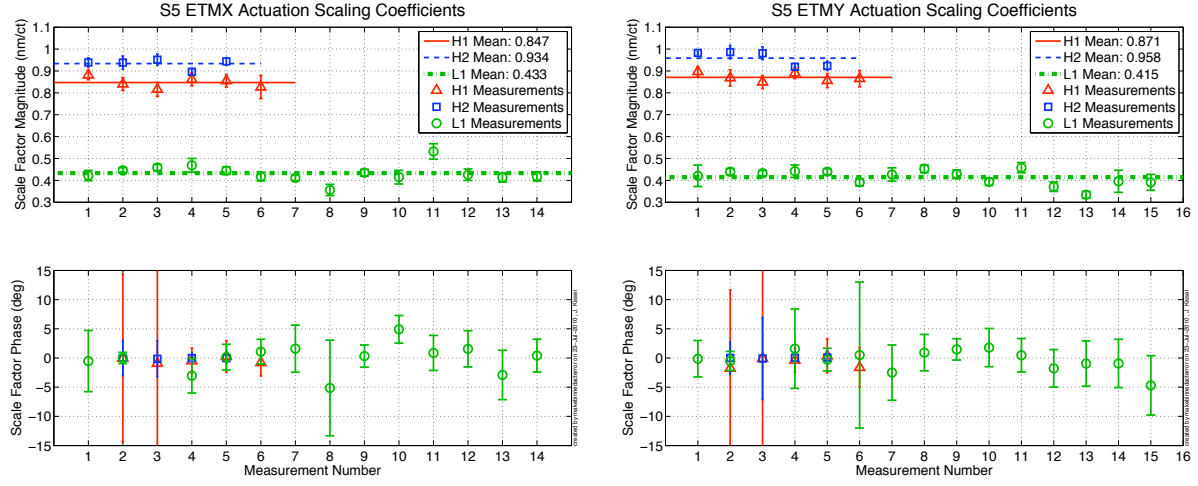


Figure 6.7: Individual measurement medians and uncertainties of the actuation scaling coefficients,  $\langle \mathcal{K}_A^x \rangle_j$  (left) and  $\langle \mathcal{K}_A^y \rangle_j$  (right), measured over the course of the fifth science run. Measurement numbers 6 in H1 and 7 through 15 in L1 used the asymmetric Michelson technique, the remainder were measured with the simple Michelson technique. Only the magnitude for each measurement (top panels) is used to determine the total scaling coefficient for each test mass (indicated by horizontal lines), as the phase (bottom panels) is consistent with zero. The statistical uncertainty of actuation function is the quadrature sum of each arm's actuation coefficient uncertainty, which takes the larger of the standard deviation of each measurements median,  $\langle \mathcal{K}_A \rangle_j$  or the mean uncertainty divided by the number of measurements  $\sigma_{\mathcal{K}_A,j}$ .

the median,  $\langle \mathcal{K}_i \rangle$  to be the standard deviation alone. However, in the second step (Eq. 6.16), we have found the single arm transfer function ratio,  $R_{ie}$ , to be consistent with a Gaussian distribution across the frequency band, so we estimate the median uncertainty as though it were a gaussian distribution and divide the standard deviation by  $\sqrt{N}$  where  $N$  is the number of frequency points. In the asymmetric Michelson method, where the measurement of  $\mathcal{K}_A$  is similar to that of  $\mathcal{K}_i$  in the simple Michelson method, we again do not assume a Gaussian distribution over the measurement band, and take the standard deviation alone.

# Appendix C: Uncertainty Estimation of the LIGO Response Function

## Response Function Model

The LIGO interferometers' digital response to length change  $\Delta L$  is

$$R_L(f, t) \equiv \frac{1 + \gamma(t) G_L(f)}{\gamma(t) C_L(f)} \quad (6.22)$$

where

$$\Delta L_{ext}(f, t) = R_L(f, t) e_D(f) \quad (6.23)$$

with  $e_D(f)$  as the digital readout of light captured at the anti-symmetric port and  $\Delta L_{ext}(f, t)$  is the external length disturbance composed of both signal and noise. The terms in the response function are the following: the interferometer's response to DARM length changes known as the length sensing function  $C_L(f)$  (its slow time dependence is tracked by the real, positive coefficient  $\gamma(t)$ ), and the open loop gain of the differential arm (DARM) length control loop  $G_L(f) = A(f) D(f) C_L(f)$ , whose components (besides  $C_L(f)$ ) are the actuation function of the test masses which define the DARM length degree of freedom  $A(f)$ , the digital control filters  $D(f)$ . The loop is drawn schematically in Figure 3.1.

This appendix serves to define the assumptions made about, and derive equations for, the dominant uncertainty terms in the magnitude and phase of the response function the error budget. For convenience and legibility, we drop all function dependence and subscripts in our notation in the remainder of this document, such that  $R_L(f, t) = R$ ,  $G_L(f) = G$ ,  $A(f) = A$ ,  $D(f) = D$ ,  $C_L(f)$ , and  $\gamma(t) = \gamma$ .

## Assumptions about the Response Function Uncertainty

Standard analysis techniques (106) tell us that if we approximate a non-linear function  $f(x_i)$  using a taylor expansion then to first order,

$$f \simeq f_0 + \sum_{i=1}^N \left( \frac{\partial f}{\partial x_i} \right) x_i \quad (6.24)$$

then the variance or “uncertainty” on  $f(x_i)$  for N variables  $x_i$  is

$$\sigma_f^2 = \sum_{i,j}^N \left( \frac{\partial f}{\partial x_i} \right) \left( \frac{\partial f}{\partial x_j} \right) \sigma_{x_i x_j}^2 = \sum_i^N \left( \frac{\partial f}{\partial x_i} \right)^2 \sigma_{x_i}^2 + \sum_{i \neq j}^N \left( \frac{\partial f}{\partial x_i} \right) \left( \frac{\partial f}{\partial x_j} \right) \sigma_{x_i x_j}^2 \quad (6.25)$$

where we have divided the uncertainty into uncorrelated terms and correlated terms containing

$$\sigma_{x_i}^2 = \lim_{n \rightarrow \infty} \left[ \frac{1}{n} \sum_k^n \left[ (x_i)_k - \bar{x}_i \right]^2 \right], \quad (6.26)$$

and

$$\sigma_{x_i x_j}^2 = \lim_{n \rightarrow \infty} \left[ \frac{1}{n} \sum_k^n \left[ (x_i)_k - \bar{x}_i \right] \left[ (x_j)_k - \bar{x}_j \right] \right] \quad (6.27)$$

where  $n$  is the number the measurements of a given set of  $N$  variables.

In principle, we must therefore find the uncertainty in all components of the response function (Eq. 6.22). However, in practice we model the sensing function  $C$  as it is intrinsically difficult at best to measure independently i.e. without the interferometer under control of the closed loop. Hence, in order to estimate the uncertainties in the response function, we re-cast it in terms of quantities that can be easily measured, (remembering that  $C = G/AD$ )

$$R = A D \frac{(1 + \gamma G)}{\gamma G} \quad (6.28)$$

Ignoring that the functions  $A$ ,  $D$  and  $G$  are complex for the time being, we find the uncertainty on Eq. 6.28 to be

$$\begin{aligned} \sigma_R^2 &= \sigma_A^2 \left( \frac{\partial R}{\partial A} \right)^2 + \sigma_D^2 \left( \frac{\partial R}{\partial D} \right)^2 + \sigma_G^2 \left( \frac{\partial R}{\partial G} \right)^2 + \sigma_\gamma^2 \left( \frac{\partial R}{\partial \gamma} \right)^2 \\ &\quad + 2 \sigma_{AD}^2 \left( \frac{\partial R}{\partial A} \right) \left( \frac{\partial R}{\partial D} \right) + 2 \sigma_{AG}^2 \left( \frac{\partial R}{\partial A} \right) \left( \frac{\partial R}{\partial G} \right) + 2 \sigma_{A\gamma}^2 \left( \frac{\partial R}{\partial A} \right) \left( \frac{\partial R}{\partial \gamma} \right) \\ &\quad + 2 \sigma_{DG}^2 \left( \frac{\partial R}{\partial D} \right) \left( \frac{\partial R}{\partial G} \right) + 2 \sigma_{D\gamma}^2 \left( \frac{\partial R}{\partial D} \right) \left( \frac{\partial R}{\partial \gamma} \right) + 2 \sigma_{G\gamma}^2 \left( \frac{\partial R}{\partial G} \right) \left( \frac{\partial R}{\partial \gamma} \right) \end{aligned} \quad (6.29)$$

We do not assign any uncertainty to the digital filters  $D$ . This function is a well known digital quantity and any uncertainties are negligible compared with those of all other terms in the response function. Hence, for the purposes of propagation we assume  $D_k - \bar{D} = 0$  for all  $n$  measurements, drop it from the error budget, and

$$\begin{aligned} \sigma_R^2 &= \sigma_A^2 \left( \frac{\partial R}{\partial A} \right)^2 + \sigma_G^2 \left( \frac{\partial R}{\partial G} \right)^2 + \sigma_\gamma^2 \left( \frac{\partial R}{\partial \gamma} \right)^2 \\ &\quad + 2 \sigma_{AG}^2 \left( \frac{\partial R}{\partial A} \right) \left( \frac{\partial R}{\partial G} \right) + 2 \sigma_{A\gamma}^2 \left( \frac{\partial R}{\partial A} \right) \left( \frac{\partial R}{\partial \gamma} \right) \\ &\quad + 2 \sigma_{G\gamma}^2 \left( \frac{\partial R}{\partial G} \right) \left( \frac{\partial R}{\partial \gamma} \right). \end{aligned} \quad (6.30)$$

As  $\gamma$  is a function of time alone, and  $A$  and  $G$  are functions of frequency alone, we assume  $\gamma$  is by definition are uncorrelated with  $A$  and  $G$ : on average, we expect to find equal

distributions of positive and negative values for their respective covariant terms such that they vanish in the limit of a large random selection of observations. This leaves only the actuation function  $A$  and open loop gain  $G$  to have some possible correlation, and the relative uncertainty becomes

$$\frac{\sigma_R^2}{R^2} = \left[ \frac{\sigma_A^2}{R^2} \left( \frac{\partial R}{\partial A} \right)^2 + \frac{\sigma_G^2}{R^2} \left( \frac{\partial R}{\partial G} \right)^2 + 2 \frac{\sigma_{AG}^2}{R^2} \left( \frac{\partial R}{\partial A} \right) \left( \frac{\partial R}{\partial G} \right) \right] + \frac{\sigma_\gamma^2}{R^2} \left( \frac{\partial R}{\partial \gamma} \right)^2. \quad (6.31)$$

We can write out each weighting coefficient explicitly using Eq. 6.28

$$\begin{aligned} \left( \frac{\partial R}{\partial A} \right) &= D \frac{1 + \gamma G}{\gamma G} & \left( \frac{\partial R}{\partial G} \right) &= -AD \frac{1}{\gamma G^2} & \left( \frac{\partial R}{\partial \gamma} \right) &= -AD \frac{1}{\gamma^2 G} \\ \frac{1}{R^2} \left( \frac{\partial R}{\partial A} \right)^2 &= \frac{1}{A^2} & \frac{1}{R^2} \left( \frac{\partial R}{\partial G} \right)^2 &= \frac{1}{G^2} \left( \frac{1}{1 + \gamma G} \right)^2 &= W^2 \frac{1}{G^2} \\ \frac{1}{R^2} \left( \frac{\partial R}{\partial \gamma} \right)^2 &= \frac{1}{\gamma^2} \left( \frac{1}{1 + \gamma G} \right)^2 &= W^2 \frac{1}{\gamma^2} \\ \frac{1}{R^2} \left( \frac{\partial R}{\partial A} \right) \left( \frac{\partial R}{\partial G} \right) &= -\frac{1}{A} \frac{1}{G} \left( \frac{1}{1 + \gamma G} \right) &= -W \frac{1}{A} \frac{1}{G} \end{aligned} \quad (6.32)$$

where we've defined the weighting function

$$W \equiv \frac{1}{1 + \gamma G}. \quad (6.33)$$

In doing so, we find that assuming  $A$  and  $G$  are correlated *reduces* the estimate of the total response function uncertainty,

$$\frac{\sigma_R^2}{R^2} = \left[ \frac{\sigma_A^2}{A^2} + W^2 \frac{\sigma_G^2}{G^2} - 2W \frac{\sigma_{AG}^2}{AG} \right] + W^2 \frac{\sigma_\gamma^2}{\gamma^2} \quad (6.34)$$

as opposed to if we assume they are uncorrelated,

$$\frac{\sigma_R^2}{R^2} = \left[ \frac{\sigma_A^2}{A^2} + W^2 \frac{\sigma_G^2}{G^2} \right] + W^2 \frac{\sigma_\gamma^2}{\gamma^2} \quad (6.35)$$

In principle, there is a third, “worst case” scenario, in which  $\sigma_{AG}^2$  is negative implying that  $A$  and  $G$  are *anti*-correlated. In this case, the uncertainty is inflated to

$$\frac{\sigma_R^2}{R^2} = \left[ \frac{\sigma_A^2}{A^2} + W^2 \frac{\sigma_G^2}{G^2} + 2W \frac{|\sigma_{AG}|}{AG} \right] + W^2 \frac{\sigma_\gamma^2}{\gamma^2}. \quad (6.36)$$

However, we can imagine no physical grounds for this case to occur.

We adopt the conservative assumption that  $A(f)$  and  $G(f)$ , and therefore all terms in response function are uncorrelated,

$$\frac{\sigma_R^2}{R^2} = \frac{\sigma_A^2}{R^2} \left( \frac{\partial R}{\partial A} \right)^2 + \frac{\sigma_G^2}{R^2} \left( \frac{\partial R}{\partial G} \right)^2 + \frac{\sigma_\gamma^2}{R^2} \left( \frac{\partial R}{\partial \gamma} \right)^2. \quad (6.37)$$

Though we suspect that the uncertainty in  $G$  comes from our uncertainty in  $A$ , we have no direct evidence that this is the case. It is conceivable (in fact, probable) that there is uncertainty in our model of  $C$ . Hence, we adopt this conservative assumption, which implies that we treat the uncertainty in  $G$  as though it were composed entirely of the uncertainty in  $C$ .

Though we take  $A$  and  $G$  to be uncorrelated in the overall response function uncertainty estimate, we assign the systematic uncertainty in  $A$  to be the larger of the frequency dependent uncertainty in the measurements of  $A$  and the residuals between model and measurement of  $G$ . In practice

## The Complex Uncertainty Estimation

We choose to report the variance separated into the magnitude and phase of the complex response function. If the magnitude and phase of a given complex function  $X$  are defined as usual,

$$|X| = \sqrt{(X X^*)}$$

$$\phi_X = \arctan \left( \frac{\Im m\{X\}}{\Re e\{X\}} \right) = \arctan \left( \frac{1}{i} \frac{X - X^*}{X + X^*} \right)$$

then the magnitude and phase of Eq. (6.28) is

$$|R| = \sqrt{\left( \frac{|A||D|}{\gamma|G|} \right)^2 (1 + (\gamma|G|)^2 + 2\gamma|G| \cos(\phi_G))} \quad (6.38)$$

$$\phi_R = \arctan \left( \frac{\gamma|G| \sin(\phi_A + \phi_D) + \sin(\phi_A + \phi_D - \phi_G)}{\gamma|G| \cos(\phi_A + \phi_D) + \cos(\phi_A + \phi_D - \phi_G)} \right) \quad (6.39)$$

The remainder of this document will focus on the details of calculating the (relative) uncertainty in magnitude ( $\sigma_{|R|}/|R|$ )<sup>2</sup> and (absolute) uncertainty in phase  $\sigma_{\phi_R}^2$  of our response function model  $R$ .

## Relative Magnitude Uncertainty

We know  $|R| = f(|A|, |D|, |G|, \phi_G, \gamma)$ . As described in §6, we ignore terms involving uncertainty in  $\sigma_{|D|}$ , and we treat all remaining variables as uncorrelated, such that

$$\sigma_{|R|}^2 = \left( \frac{\partial|R|}{\partial|A|} \right)^2 \sigma_{|A|}^2 + \left( \frac{\partial|R|}{\partial|G|} \right)^2 \sigma_{|G|}^2 + \left( \frac{\partial|R|}{\partial\phi_G} \right)^2 \sigma_{\phi_G}^2 + \left( \frac{\partial|R|}{\partial\gamma} \right)^2 \sigma_\gamma^2 \quad (6.40)$$

and therefore the relative variance is

$$\begin{aligned}\frac{\sigma_{|R|}^2}{|R|^2} &= \left(\frac{\partial|R|}{\partial|A|}\right)^2 \frac{\sigma_{|A|}^2}{|R|^2} + \left(\frac{\partial|R|}{\partial|G|}\right)^2 \frac{\sigma_{|G|}^2}{|R|^2} + \left(\frac{\partial|R|}{\partial\phi_G}\right)^2 \frac{\sigma_{\phi_G}^2}{|R|^2} + \left(\frac{\partial|R|}{\partial\gamma}\right)^2 \frac{\sigma_\gamma^2}{|R|^2} \\ &= \left(\frac{(\partial_{|A|}|R|)^2}{|R|^2}\right) \sigma_{|A|}^2 + \left(\frac{(\partial_{|G|}|R|)^2}{|R|^2}\right) \sigma_{|G|}^2 + \left(\frac{(\partial_{\phi_G}|R|)^2}{|R|^2}\right) \sigma_{\phi_G}^2 + \left(\frac{(\partial_\gamma|R|)^2}{|R|^2}\right) \sigma_\gamma^2 \\ \left(\frac{\sigma_{|R|}}{|R|}\right)^2 &= \left(\frac{\partial_{|A|}|R|}{|R|}\right)^2 \sigma_{|A|}^2 + \left(\frac{\partial_{|G|}|R|}{|R|}\right)^2 \sigma_{|G|}^2 + \left(\frac{\partial_{\phi_G}|R|}{|R|}\right)^2 \sigma_{\phi_G}^2 + \left(\frac{\partial_\gamma|R|}{|R|}\right)^2 \sigma_\gamma^2 \quad (6.41)\end{aligned}$$

The weighting coefficients for each variance term in Eq. (6.41) are

$$\left(\frac{\partial_{|A|}|R|}{|R|}\right)^2 = \frac{1}{|A|^2} \quad (6.42)$$

$$\left(\frac{\partial_{|G|}|R|}{|R|}\right)^2 = \frac{1}{|G|^2} \frac{(1 + \gamma|G| \cos \phi_G)^2}{(1 + (\gamma|G|)^2 + 2\gamma|G| \cos \phi_G)^2} \quad (6.43)$$

$$\left(\frac{\partial_{\phi_G}|R|}{|R|}\right)^2 = \frac{(\gamma|G|)^2 \sin^2(\phi_G)}{(1 + (\gamma|G|)^2 + 2\gamma|G| \cos \phi_G)^2} \quad (6.44)$$

$$\left(\frac{\partial_\gamma|R|}{|R|}\right)^2 = \frac{1}{\gamma^2} \frac{(1 + \gamma|G| \cos \phi_G)^2}{(1 + (\gamma|G|)^2 + 2\gamma|G| \cos \phi_G)^2} \quad (6.45)$$

Eqs. (6.43), (6.44), and (6.45), can be cleaned up a bit if we note that the real and imaginary parts of the weighting function  $W$  are

$$\begin{aligned}W &\equiv \frac{1}{1 + \gamma G} \\ \Re e \{W\} &= \Re e \left\{ \frac{1}{1 + \gamma G} \right\} \\ &= \frac{1}{2} \left( \frac{1}{1 + \gamma G} + \frac{1}{1 + \gamma G^*} \right) \\ &= \frac{1}{2} \left( \frac{1}{1 + \gamma|G|e^{i\phi_G}} + \frac{1}{1 + \gamma|G|e^{-i\phi_G}} \right) \\ &= \frac{1}{2} \left( \frac{(1 + \gamma|G|e^{-i\phi_G}) + (1 + \gamma|G|e^{i\phi_G})}{(1 + \gamma|G|e^{i\phi_G})(1 + \gamma|G|e^{-i\phi_G})} \right) \\ &= \frac{1}{2} \left( \frac{2 + \gamma|G|(e^{i\phi_G} + e^{-i\phi_G})}{(1 + (\gamma|G|)^2) + \gamma|G|(e^{i\phi} + e^{-i\phi})} \right) \\ &\quad \left( \frac{e^{i\theta} + e^{-i\theta}}{2} = \cos \theta \right) \\ \Re e \{W\} &= \frac{1 + \gamma|G| \cos(\phi_G)}{(1 + (\gamma|G|)^2 + 2\gamma|G| \cos(\phi_G))} \\ \Rightarrow \Re e \{W\}^2 &= \frac{(1 + \gamma|G| \cos(\phi_G))^2}{(1 + (\gamma|G|)^2 + 2\gamma|G| \cos(\phi_G))^2} \quad (6.46)\end{aligned}$$

$$\begin{aligned}
\Im m \{W\} &= \Im m \left\{ \frac{1}{1 + \gamma G} \right\} \\
&= \frac{1}{2i} \left( \frac{1}{1 + \gamma G} - \frac{1}{1 + \gamma G^*} \right) \\
&= \frac{1}{2i} \left( \frac{1}{1 + \gamma |G| e^{i\phi_G}} - \frac{1}{1 + \gamma |G| e^{-i\phi_G}} \right) \\
&= \frac{1}{2i} \left( \frac{(1 + \gamma |G| e^{-i\phi_G}) - (1 + \gamma |G| e^{i\phi_G})}{(1 + \gamma |G| e^{i\phi_G})(1 + \gamma |G| e^{-i\phi_G})} \right) \\
&= \frac{1}{2i} \left( \frac{-\gamma |G| (e^{i\phi_G} - e^{-i\phi_G})}{(1 + (\gamma |G|)^2) + \gamma |G| (e^{i\phi} + e^{-i\phi})} \right) \\
&\quad \left( \frac{e^{i\theta} - e^{-i\theta}}{2i} = \sin \theta \right) \\
\Im m \{W\} &= \frac{\gamma |G| \sin(\phi_G)}{(1 + (\gamma |G|)^2 + 2\gamma |G| \cos(\phi_G))} \\
\Rightarrow \Im m \{W\}^2 &= \frac{(\gamma |G|)^2 \sin^2(\phi_G)}{(1 + (\gamma |G|)^2 + 2\gamma |G| \cos(\phi_G))^2} \tag{6.47}
\end{aligned}$$

Thus, we combine Eqs. (6.41) through (6.47) to arrive at our final expression for the relative magnitude uncertainty on the response function,

$$\left( \frac{\sigma_{|R|}}{|R|} \right)^2 = \left( \frac{\sigma_{|A|}}{|A|} \right)^2 + \Re e\{W\}^2 \left( \frac{\sigma_{|G|}}{|G|} \right)^2 + \Im m\{W\}^2 \sigma_{\phi_G}^2 + \Re e\{W\}^2 \left( \frac{\sigma_\gamma}{\gamma} \right)^2 \tag{6.48}$$

## Phase Uncertainty

The calculation of the phase uncertainty is quite similar. We know  $\phi_R = f(\phi_A, \phi_D, |G|, \phi_G, \gamma)$ , but we ignore uncertainty in  $\phi_D$  and take the conservative estimate that all other uncertainties are uncorrelated such that the absolute variance in phase is

$$\sigma_{\phi_R}^2 = \left( \frac{\partial \phi_R}{\partial \phi_A} \right)^2 \sigma_{\phi_A}^2 + \left( \frac{\partial \phi_R}{\partial |G|} \right)^2 \sigma_{|G|}^2 + \left( \frac{\partial \phi_R}{\partial \phi_G} \right)^2 \sigma_{\phi_G}^2 + \left( \frac{\partial \phi_R}{\partial \gamma} \right)^2 \sigma_\gamma^2. \tag{6.49}$$

Thus, as before we calculate the weighting factors,

$$\left( \frac{\partial \phi_R}{\partial \phi_A} \right)^2 = 1 \tag{6.50}$$

$$\left( \frac{\partial \phi_R}{\partial |G|} \right)^2 = \frac{\gamma^2 \sin^2(\phi_G)}{(1 + (\gamma |G|)^2 + 2\gamma |G| \cos \phi_G)^2} = \Im m\{W\}^2 \frac{1}{|G|^2} \tag{6.51}$$

$$\left( \frac{\partial \phi_R}{\partial \phi_G} \right)^2 = \frac{(1 + \gamma |G| \cos \phi_G)^2}{(1 + (\gamma |G|)^2 + 2\gamma |G| \cos \phi_G)^2} = \Re e\{W\}^2 \tag{6.52}$$

$$\left( \frac{\partial \phi_R}{\partial \gamma} \right)^2 = \frac{|G|^2 \sin^2(\phi_G)}{(1 + (\gamma |G|)^2 + 2\gamma |G| \cos \phi_G)^2} = \Im m\{W\}^2 \frac{1}{\gamma^2} \tag{6.53}$$

and substitute back into Eq. (6.49),

$$\sigma_{\phi_R}^2 = \sigma_{\phi_A}^2 + \Im m\{W\}^2 \left( \frac{\sigma_{|G|}}{|G|} \right)^2 + \Re e\{W\}^2 \sigma_{\phi_G}^2 + \Im m\{W\}^2 \left( \frac{\sigma_\gamma}{\gamma} \right)^2 \quad (6.54)$$

## Summary

The model of the LIGO interferometer's response to gravitational wave strain from an optimally-oriented source is

$$R \equiv \frac{1 + \gamma G}{\gamma C} \quad (6.55)$$

which, for the purposes of uncertainty estimation can be re-written in terms of easily measurable quantities,

$$R = A D \frac{(1 + \gamma G)}{\gamma G} \quad (6.56)$$

Where  $G = ADC$ , and we assume that the digital filter function  $D$  has negligible uncertainty.

We report the uncertainty of our model in terms of relative magnitude and absolute phase uncertainty, which are comprised of the measured uncertainty in each model component,

$$\left( \frac{\sigma_{|R|}}{|R|} \right)^2 = \left( \frac{\sigma_{|A|}}{|A|} \right)^2 + \Re e\{W\}^2 \left( \frac{\sigma_{|G|}}{|G|} \right)^2 + \Im m\{W\} \sigma_{\phi_G}^2 + \Re e\{W\}^2 \left( \frac{\sigma_\gamma}{\gamma} \right)^2 \quad (6.57)$$

$$\sigma_{\phi_R}^2 = \sigma_{\phi_A}^2 + \Im m\{W\}^2 \left( \frac{\sigma_{|G|}}{|G|} \right)^2 + \Re e\{W\}^2 \sigma_{\phi_G}^2 + \Im m\{W\}^2 \left( \frac{\sigma_\gamma}{\gamma} \right)^2 \quad (6.58)$$

where  $W = 1/(1+G)$  is the weighting function of the DARM control loop. In these definitions is the implicit assumption that the uncertainties in the actuation function  $A$  and open loop gain  $G$  are treated conservatively as uncorrelated.

## Appendix D: Tilt-Horizontal Coupling

Inertial sensors measure the position of a suspended proof mass in the sensor's sensitive direction,  $x_{pm}$ . They are well modeled by an damped harmonic oscillator, as shown in Figure 6.8. When a single axis inertial sensor operates under the presence of gravity, its equation of motion is

$$\ddot{x}_{sp} = \ddot{x}_{pm} + \frac{\omega_0}{Q} \dot{x}_{pm} + \omega_0^2 x_{pm} + g \cos \Theta \quad (6.59)$$

where  $x_{pm}$  and  $x_{sp}$  are the position of the proof mass and suspension point along the sensitive direction,  $\omega_0$  and  $Q$  are the natural frequency and quality factor of the suspension, and  $0 < \Theta < \pi$  is the angle of the sensitive direction with respect to local vertical, defined by gravity. Hence, the sensor output,  $x_{pm}$ , is both a function of its orientation and input acceleration.  $\Theta$  can be decomposed into a constant, optimal orientation  $\Theta_0$ , and any small change in orientation as the sensor tilted,  $\theta(f) \ll 1$ . If so, then the infinitesimal change in apparent force of the proof mass is

$$\ddot{x}_{pm} + \frac{\omega_0}{Q} \dot{x}_{pm} + \omega_0^2 x_{pm} = \ddot{x}_{sp} - g [\cos \Theta_0 \cos \theta - \sin \Theta_0 \sin \theta]. \quad (6.60)$$

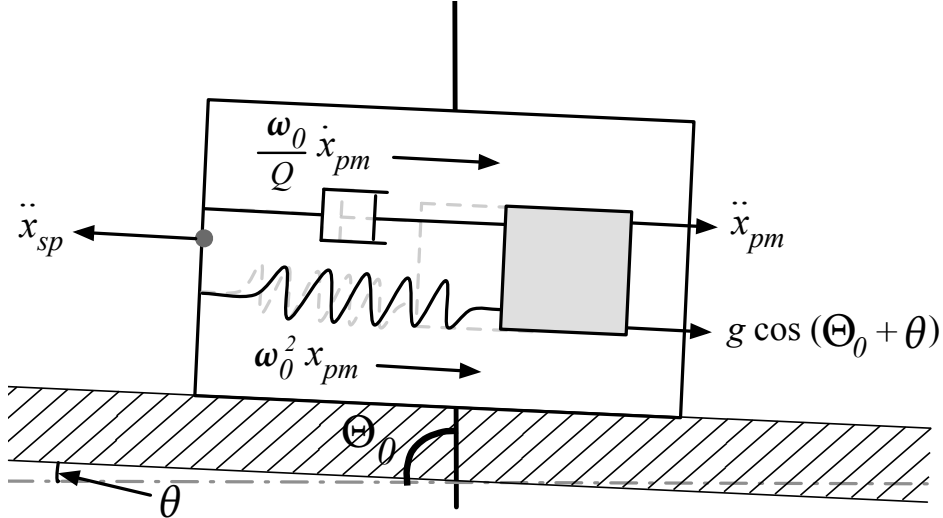


Figure 6.8: Diagram of a horizontal seismometer ( $\Theta_0^{(h)} = \pi/2$ ) under the influence of a small tilt  $\theta$  of the platform which is translating in the horizontal direction  $x_{sp}$ .

We define “vertical” inertial sensor as one whose optimal orientation is  $\Theta_0^{(v)} = 0$ . For sufficiently small deviations,  $\theta$  from this orientation,  $\cos \theta = 1 + \mathcal{O}(\theta^2)$ . This leaves the vertical sensor insensitive to the deviation (to first order),

$$\ddot{x}_{pm}^{(v)} + \frac{\omega_0}{Q} \dot{x}_{pm}^{(v)} + \omega_0^2 x_{pm}^{(v)} = \ddot{x}_{sp}^{(v)} - g. \quad (6.61)$$

However, for a “horizontal” sensor, where  $\Theta_0^{(h)} = \pi/2$ , the output is maximally sensitive to tilt, as  $\sin \theta = \theta + \mathcal{O}(\theta^2)$ , and

$$\ddot{x}_{pm}^{(h)} + \frac{\omega_0}{Q} \dot{x}_{pm}^{(h)} + \omega_0^2 x_{pm}^{(h)} = \ddot{x}_{sp}^{(h)} + g\theta. \quad (6.62)$$

This sensitivity to small changes in orientation is known as tilt-horizontal coupling. The frequency response of the sensor is derived from the Fourier transform of Eq. 6.62,

$$\begin{aligned} -\omega^2 x_{pm}^{(h)} + i \frac{\omega_0}{Q} \omega x_{pm}^{(h)} + \omega_0^2 x_{pm}^{(h)} &= -\omega^2 x_{sp}^{(h)} + g\theta. \\ -\left(\omega^2 - \frac{\omega_0}{Q} i\omega - \omega_0^2\right) x_{pm}^{(h)} &= -\omega^2 \left(x_{sp}^{(h)} - \frac{g}{\omega^2} \theta\right) \\ x_{pm}^{(h)} &= \frac{\omega^2}{\left(\omega^2 - \frac{\omega_0}{Q} i\omega - \omega_0^2\right)} \left(x_{sp}^{(h)} - \frac{g}{\omega^2} \theta\right) \end{aligned} \quad (6.63)$$

indicating the ratio between the tilt and horizontal sensitivity is

$$\frac{\theta}{x_{sp}^{(h)}} = -\frac{g}{\omega^2} \quad (6.64)$$

When  $-(g/\omega^2)\theta > x_{sp}$ , the horizontal inertial sensor becomes dominated by tilt signal  $\theta$ , with its sensitivity increasing proportional to  $\omega^2$ . If such a signal is used in feed back control, cross-coupling between translation and tilt degrees of freedom destroys the linearity of the control loop at low frequencies, and necessitates multi-input-multi-output control, complicating the design. The frequency at which the tilt signal begins to dominate the is referred to as the “tilt-horizontal coupling zero,”

$$f_{thc} \approx \frac{1}{2\pi} \sqrt{\left| -g \left( \frac{\theta}{x_{sp}} \right) \right|}. \quad (6.65)$$

This nomenclature arises from the change in slope of inertial sensor response at  $f_{thc}$ , the details of which are determined by the curvature of tilt,  $\alpha = \theta/|\theta|$ . In general, this curvature may be time-varying, and non-linear (96), but we consider only constant curvature here. For positive curvature  $\alpha = +1$  (in the case where the platform tilts up along a circular arc of radius  $r$  when pushed horizontally, as a pendulum), the phase between tilt and translation cancel near  $f_{thc}$ , resulting in decrease in response magnitude. For constant negative curvature  $\alpha = -1$ , as is the case where the platform tilts down along a circular arc of radius  $r$  when pushed horizontally, the phase does not neatly cancel and no reduction in response is seen. These two cases are demonstrated in Figure 6.9.

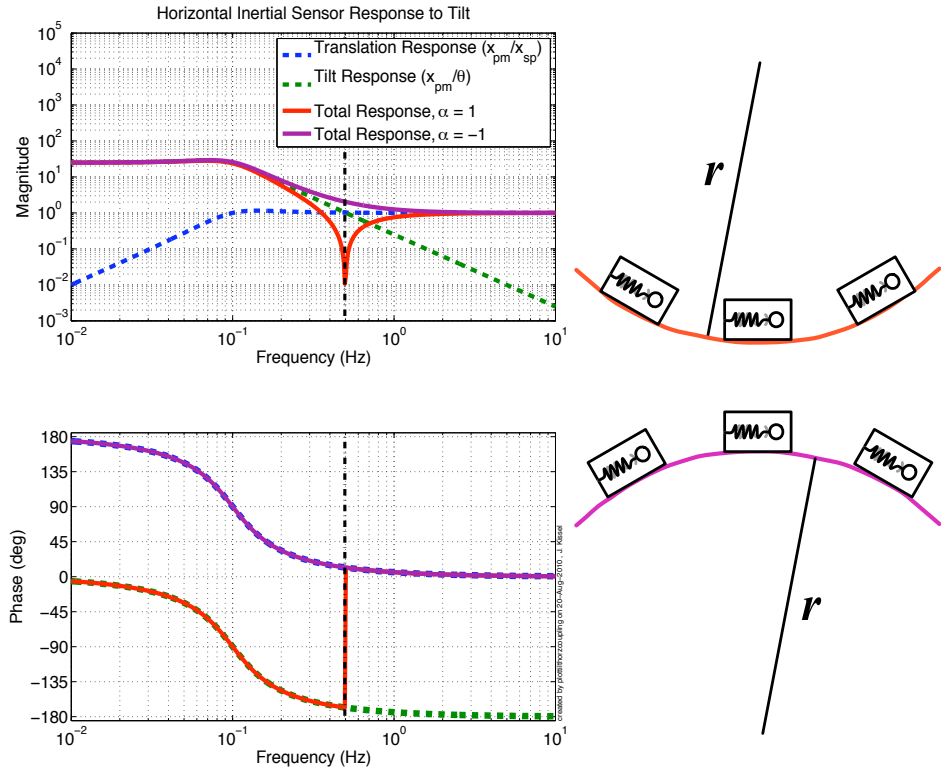


Figure 6.9: Model, normalized response of an inertial sensor ( $f_0 = 0.1$  Hz,  $Q = 1$ ) under both tilt and translation (in arbitrary velocity units). The idealized response to translation is shown in dashed blue. The response under the influence of linear tilt-horizontal coupling alone is shown in dashed green. If the sign of the tilt curvature is positive (as shown in the right-top drawing), and the magnitude of tilt is equal to the amount of input translation, the resulting response of the inertial sensor is shown in red. However, if the tilt curvature is negative (as shown in the right-bottom drawing), the resulting response is shown in purple. The tilt-horizontal coupling zero is shown in dash-dotted black with  $f_{thc} = 0.5$  Hz.

## Appendix E: Copyright Permissions

(53) is published and permission is granted to reproduce it.

From: william barletta <wabarletta@lbl.gov>  
Subject: **Re: Your Submission**  
Date: July 28, 2010 2:22:09 PM CDT  
To: Jeff Kissel <jkisse1@tigers.lsu.edu>

---

Jeff,

The submission looked good to me. Every thing was clearly spelled out. I know that the collaboration reviews are quite thorough. In that case my priority is to get the material into print as fast as possible.

You are welcome to use the material as you suggest in your thesis. This is explicitly part of the journal's use policy. We ask only That your citation of the publication (you can use the DOI as this is a unique identifier among all publishers) is explicit and clear.

Good luck with the thesis.

Bill Barletta

Jeff Kissel wrote:

Hey Dr. Barletta,  
This is excellent news, thank you! I'm surprised to see there were no comments from the reviewer, I hope everything was sufficient.

One question: I intend to use the material covered in this paper as a portion of my doctoral thesis. What are the policies of NIM-A in this regard? From what I have seen of fellow graduate student theses, they have placed a footnote at the beginning of the chapter(s) where previously published material is used saying something to the effect of "Reprinted with the permission from [NIM-A]," with an immediate citation of the paper. Is this acceptable?

Thanks again!

Cheers,  
Jeff Kissel  
Graduate, Physics  
Experimental Gravity Group  
Louisiana State University

## Vita

Jeffrey Scott Kissel was born in Rochester, New York, to Tom and Eileen Kissel. He graduated from Greece Athena High School in 2001, and received his bachelor of science in astronomy and astrophysics from the Pennsylvania State University in 2005. In the Fall of 2005, Jeff began his graduate studies at LSU. While there, he was awarded the LIGO Student Fellowship and became a visiting student researcher at the LIGO Livingston Observatory in 2007. Jeff will graduate with a doctorate of philosophy in physics and astronomy in Fall of 2010.